INVESTIGATION OF CHAOTIC ADVECTION REGIME AND ITS EFFECT ON THERMAL PERFORMANCE OF WAVY WALLED MICROCHANNELS

Hassanali Ghaedamini Harouni

(B. Sc. Isfahan University of Technology, Iran)

A THESIS SUBMITTED FOR THE DEGREE OF

DOCTOR OF PHILOSOPHY

DEPARTMENT OF MECHANICAL ENGINEERING

NATIONAL UNIVERSITY OF SINGAPORE

2015

Declaration

I hereby declare that the content presented in this dissertation has originated from my doctoral level original research endeavor under the guidance of Prof. Poh Seng Lee and Prof. Chiang Juay Teo at National University of Singapore. I also assert that this thesis has been thoroughly composed by me and any relevant source of information has been duly referred to and cited.

Moreover, I also admit that neither part of this thesis nor the entire copy has been submitted elsewhere for any academic degree achievement purpose.

Hassanali Ghaedamini Harouni

21/01/2015

Acknowledgements

I would like to express my gratitude to all those people who contributed in different ways to this thesis. I am really grateful to my beloved parents and younger sister, Maryam, for their supreme support and encouragement. Without them, my dream would not have come true. I am particularly grateful to my supervisor Prof. Lee Poh Seng who guided me in this study without imposing his personal viewpoint, but rather encouraging a fruitful discussion and debate. And I would like to thank my co-supervisor, Prof. Teo Chiang Juay for all the discussions and support.

I am very much pleased to acknowledge my colleagues and good friends, Mrinal, Matthew and Bugra and specially our lab officer, Ms. Roslina, for their assistance and support in the development of work in various ways.

I would also like to thank Lee Foundation for their support grant during the final semester of my studies.

Hassanali Ghaedamini

January 2015

Contents

ABSTRACT

Since the early works of Tuckerman and Peace [1], liquid cooling of electronics using microchannel heat sinks has proven to be a viable solution for high heat dissipation rates needed for modern electronics. While a microchannel heat sink has high heat transfer area-to-volume ratio due to its small dimension, it also typically operates in the laminar flow regime which is thermally less effective compared to the turbulence regime. Hence, finding ways to enhance mixing and as a result heat transfer has been a topic of interest in recent years.

Chaotic advection is a regime in which a laminar and well behaving Eulerian fluid field shows chaos in its Lagrangian representation, i.e. chaotic and irregular pathline for fluid particles. This concept is being used for enhancing the transport phenomenon in micro scale devices like microreactors, micromixers and microchannel heat sinks. While utilizing chaotic advection in micromixers through three dimensionally twisted shapes are well established in literature, studying and characterizing planar designs for heat transfer applications have not been extensively studied.

Wavy walled microchannels are believed to show chaotic advection as they force the fluid elements to stretch and fold due to the three dimensional vortical structures formed in them. For a converging-diverging shape, which is studied in this thesis, these vortical structures are four streamwise vortices at the corners of the contraction part of the furrow and two counter rotating vortices in the trough region of the furrow. Our geometrical and flow parametric study on the converging-diverging configuration shows that chaotic advection is indeed present in this converging-diverging design. However, chaotic advection becomes stronger at higher *Re* and/or for highly modulated channels. Strong chaotic advection shows itself with an asymmetric Poincaré map and also a sharp increase in the heat transfer and pressure drop behaviors.

Along with the numerical investigations on the parametric space for both fully developed and developing conditions, experiments were performed to validate the numerical results. Converging-diverging microchannel heat sinks were designed with the microchannels being machined on a 2.5 cm by 2.5 cm footprint area with possible application in electronics cooling. Different levels of wall waviness and Reynolds number up to 800 were studied. A good agreement between the numerical results and the experiments was observed which further validates the numerical approach.

The numerical and experimental results show that high heat transfer rates due to the presence of strong chaotic advection is indeed achievable with converging-diverging microchannel heat sinks albeit with high pressure drop penalties. Thus, in the last chapter the concept of *chaotic advection near resonance* is introduced to enhance heat transfer at relatively lower pressure drop tradeoff by achieving a strong chaotic advection regime for slightly modulated channels and at relatively smaller Reynolds numbers. Heat transfer enhancements of up to 70% are observed with this novel method while the pressure drop penalty was lower than 60%.

Our results confirm that the converging-diverging microchannel design is a very good candidate for passive and active heat transfer augmentation. Especially considering that almost all the micro-pumps are inherently pulsatile, the concept of chaotic advection near resonance introduced in this thesis can certainly find applications in microscale thermal systems. In addition, wavy walled microchannel heat sinks show a more uniform temperature distribution compared to the straight design. Since heat transfer is a strong function of wall waviness, such a design can be used for conditions with non-uniform heat flux distribution and also for hot spot mitigation.

List of Tables

List of Figures

Nomenclature

A	wavy wall amplitude, m
A_{cb}	bottom area of a single channel, m^2
A_{cs}	side wall area of a single channel, m^2
A_{FP}	footprint area, m^2
A_{HT}	heat transfer area, m^2
a	average width of the channel, m
b	channel depth, m
C_p	specific heat capacity, J/kgK
D_h	hydraulic diameter of the averaged cross section, m
DAQ	data acquisition system
f	friction factor
f_p	pulsation frequency, Hz
Δf	variation in friction factor
FOM	figure of merit
h	heat transfer coefficient, W/m^2K
IGBT	insulated-gate bipolar transistor
ITRS	International Technology Roadmap for Semiconductors
k	thermal conductivity, W/mK
L	wavy wall wavelength, m
$\dot{m}$	mass flow rate, kg/sec
N	number of furrows
Nu	Nusselt number
N_t	number of time steps in one pulsation period
ΔNu	variation in Nusselt number
M	number of channels
P	pressure, Pa
ΔP	pressure drop, Pa

PF	performance factor
PP	pumping power, W
Q	heat transfer rate, W
q''	heat flux, W/m^2
R	thermal resistance, K/W
Re	Reynolds number
S	aspect ratio of the equivalent straight microchannel
S'	aspect ratio of the narrowest part of the microchannel
S_w	fin thickness, m
S_v	vertical distance of the thermocouples to the base of microchannels, m
T	temperature, K
ΔT_{lm}	logarithmic mean temperature difference, K
t	time, s
Δt	time step, s
U	inlet velocity, m/s
U_m	averaged velocity of the equivalent straight microchannel, m/s
UPS	uninterruptible power supply
$\dot{V}$	volumetric flow rate, m^3/s
u,v,w	velocity components, m/s
x,y,z	coordinates, m

Greek symbols

B	pressure gradient, Pa/m
γ	expansion factor
θ	scaled temperature
λ	waviness
μ	dynamic viscosity, Pa s
ρ	density, kg/m^3
τ	forced pulsation period, s

τ_w	wall shear stress, Pa

Subscripts

0	steady component
b	bulk
Cu	copper
f	fluid
in	inlet
m	mean
max	maximum
out	outlet
p	pulsatile component
s	solid
ss	steady state component
w	wall

Chapter 1. Introduction

Tuckerman and Pease [1] introduced the idea of liquid cooling of electronics in 1981. Since then, thermal management of electronics and power electronics has been the main driver for microchannel heat sink technology [2]. However, it should be noted that the concept being developed in this thesis can find its way into different industrial sectors like thermal management of LEDs [3], lasers [4] and micro-scale heat exchangers [5].

1.1. Motivation

1.1.1. Thermal challenges of electronics

Moore's law is closely related to thermal management of electronics [6]. Named after Gordon E. Moore, it states that the number of transistors in a dense integrated circuit (IC) doubles approximately every two years, as shown in Figure 1-1. More transistors means faster computation, higher power consumption for electronics and hence larger heat fluxes to be dissipated. In the 2003 report of ITRS, International Technology Roadmap for Semiconductors, the need for thermal management of electronics with heat fluxes up to 100 W/cm^2 was heavily emphasized [7]. However, the newer report of ITRS published in 2013 has minimal concerns regarding the high heat flux management and the emphasis is mostly on hot spot mitigation, co-design of chips and the multi-disciplinary (thermal, mechanical and electrical) considerations of packaging materials. This is due to the fact that the trend in designing the processors has changed in recent years whereby instead of increasing the speed of the processors, multi-core strategy is being adopted by the semiconductor industry. This multi-core strategy has suppressed the issue of overheating of the computing units and in this way air cooling is still a valid solution for personal computers despite the concerns people had in 2003. Figure 1-2 shows the trend of micro-

processor data in the past 35 years. The speed of processor is still around 3 GHz while core number has increased, at the same time the typical power consumption of a CPU has been around 100 W.

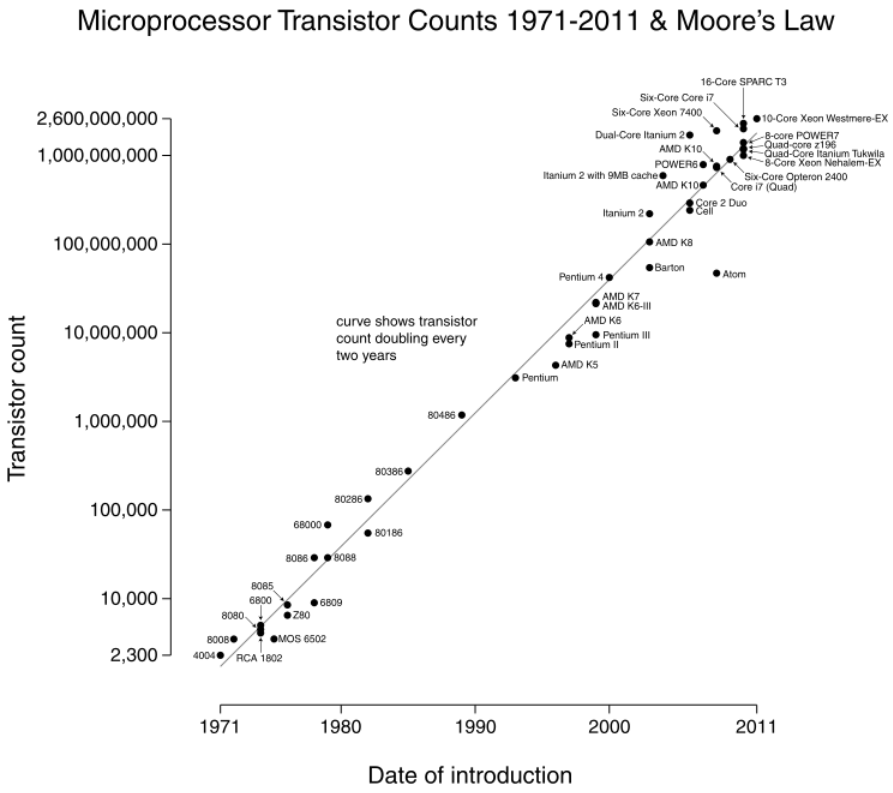

Figure 1-1. Moore's law, CPU transistor counts against dates of introduction.

Unlike personal computers, liquid cooling is a common solution for super computers and server farms due to several advantages over air cooled systems. These include: cost effectiveness, more compact designs, more efficient systems and quieter operation. Cooling is a huge fraction of power consumed by supercomputers. As an example, the newest Chinese super computer, Milkyway-2, consumes 24 megawatts of which 6 megawatts are for its closed loop water cooling system [8]. A recent study done in 2014 by HIS, a market research firm, reveals that even Data Centers are migrating towards

liquid cooling with a market size of $2.3 billion in 2014 which is anticipated to double in just two years at the current growth rate.

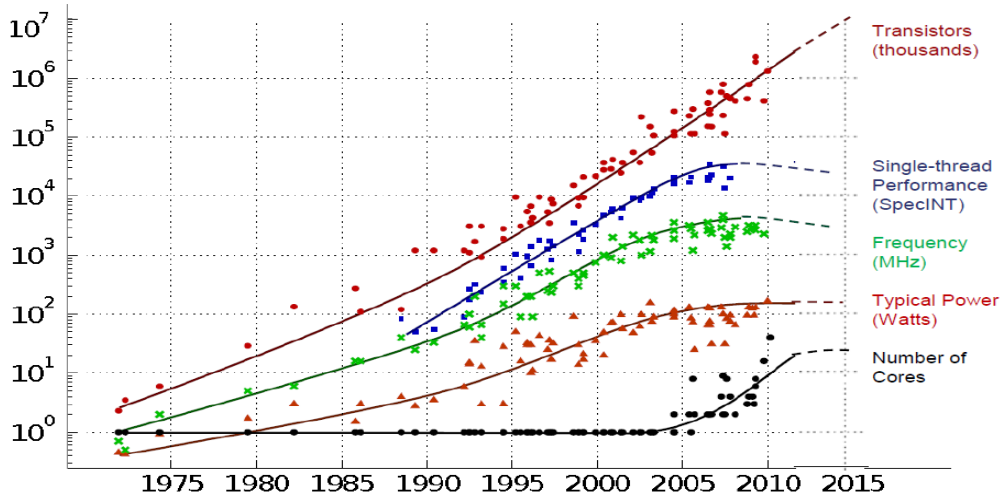

Figure 1-2. 35 years of microprocessor trend data [9], Original data collected and plotted by M. Horowitz, F. Labonte, O. Shacham, K. Olukotun, L. Hammond and C. Batten. Dotted line extrapolations are done by C. Moore.

Trends regarding the market demand and technical limitations of air cooling point out the importance of liquid cooling for electronics industry. The newer generation of ICs with 14nm technology is anticipated to hit the shelves in the second quarter of 2015 which answering their thermal management demand can be a challenge to engineers and designers.

There is also a paradigm shift taking place from traditional packaging hierarchy to 3D packaging configurations [10]. The three dimensional chip stacks thermal challenges include:

- Sizable increase in the number of power dissipating devices with a typical heat dissipation demand of 300 W/cm^2 and greater [11].
- Overlapped hotspots

- Higher thermal resistances to the heat sink due to increased number of layers

Considering the physical configuration of 3D IC stacks, Figure 1-3, liquid cooling is among the very few options for thermal management of such designs.

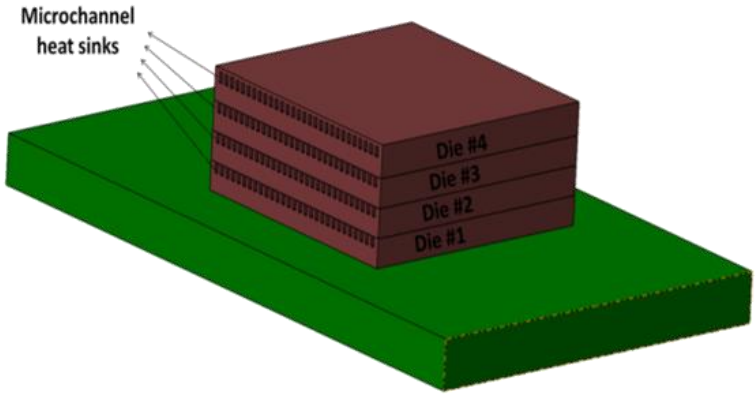

Figure 1-3. Schematic view of microchannel heat sink for 3D stacked dies.

1.1.2. Thermal challenges of power electronics

Power electronics are systems which are used to process and control the flow of electric energy by converting it from one set of voltages, currents and frequencies to another which is better suited for the user load. Power electronics save 10-15% of generated energy and they provide the opportunity to use non-conventional energy sources like solar and wind while being compact and lightweight [12]. Figure 1-4 shows the schematic representation of a power electronic system. Power electronics are the key to efficient energy generation, distribution and utilization and they have widespread applications in vehicles, power backups (UPS), power generation systems and also grid inverters.

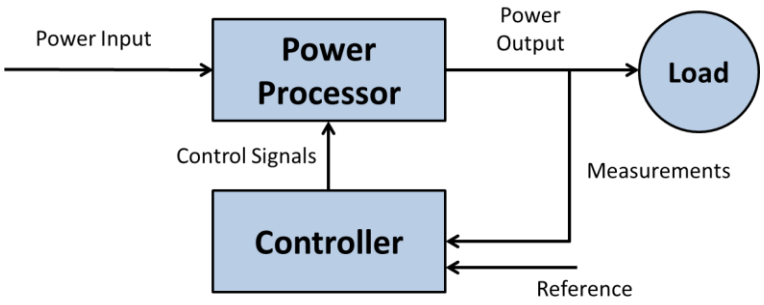

Figure 1-4. The block diagram of power electronics systems.

A multichip power electronic module contains multiple power devices, i.e. transistors and diodes, which operate in parallel to create a single switch. The module usually has high efficiencies of 95-98% with power dissipation levels of 500 – 5000 W. Considering the module size (10 – 100 cm^2), heat fluxes of 50 – 500 W/cm^2 are needed for sufficient heat dissipation.

Increasing power densities in electronics require more effective cooling solutions. Particularly for power electronic modules, controlling the temperature is critical as it affects the performance as well as the reliability of IGBTs, insulated-gate bipolar transistor. Higher temperatures will result in higher power losses in the IGBT which causes slower switching, higher leakage current and higher forward voltage. In the study done by Xu et al [13], it was shown that there is a 70% increase in switching losses when junction temperature increases from 25°C to 125°C.

1.2. Thermal management of electronics and power electronics

Figure 1-5 shows a schematic design of a typical insulated-gate bipolar transistor (IGBT) module being cooled by liquid or air. For a one dimensional thermal conduction it can be written:

$$T_{IGBT} = Q(R_{IGBT} + R_{solder} + R_{DBC} + R_{grease} + R_{base} + \frac{1}{hA_{HT}}) + T_{fluid} \qquad (1\text{-}1)$$

Hence, in order to reduce the IGBT junction temperature the following can be done:

- Use higher thermal conductive solder to reduce R_{solder}.
- Use higher thermal conductive grease to reduce R_{grease}.
- Increase effective heat transfer area, A_{HT}.
- Increase effective heat transfer coefficient, h.

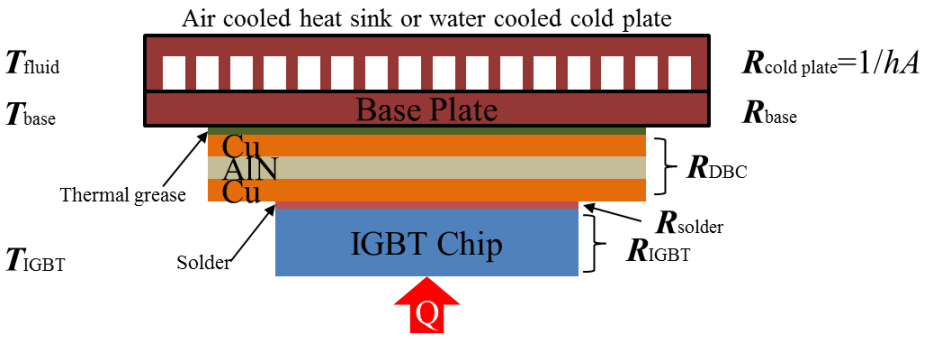

Figure 1-5. A schematically drawn packaging of an IGBT module.

Implementing any of the above measures can improve heat transfer performance of the cooling system and hence reduces the T_{IGBT}. Among the above approaches, increasing the heat transfer coefficient is the main scope of this thesis. We are seeking ways to improve heat transfer while keeping the pressure drop penalty moderate. In the next part common cooling techniques will be discussed.

1.3. Cooling techniques

While a comprehensive discussion of cooling techniques is beyond the scope of this thesis, a short treatment is nonetheless included here for completeness. These cooling techniques include:

- Single phase liquid cooling
- Two phase liquid cooling

- Microchannel flow boiling
- Jet impingement cooling
    - Spray cooling
    - Immersion cooling
- Heat pipe technology
- Thermoelectric (Peltier) coolers

All the above methods have their own advantages and drawbacks. Brief review of each of the above methods is presented below.

1.3.1. Two phase liquid cooling

Two phase liquid cooling includes microchannel flow boiling, spray cooling and impingement jets.

Two phase flow in microchannels consists of a phase changing coolant in the channels which are parallel to the heat transfer area. Heat fluxes in the range of 16-840 W/cm^2 are reported to be dissipated with this method [14] and due to the high COP and low pumping power requirement of this technique, this is an advantageous solution for situations which require light weight equipment and high heat transfer capability. Currently an extensive research is being conducted to characterize the flow boiling regime in microchannels [14]. However, the flow instability and the need for active control systems makes this an expensive technique operationally and as Kandlikar [14] has pointed out in his recent review paper on heat transfer in microchannels:

"*The complexity of a flow boiling system cannot be justified when the performance of a simpler pool boiling or single phase system is superior.*"

Spray cooling uses fine droplets of liquid which impinge individually on the heated surface and creating a thin liquid film. The thin film of the fluid carries the heat by phase change and also thermal conduction. Arrays of sprays are needed for cooling of multiple IC chips or IGBTs in the case of power electronics [15, 16].

Jet impingement cooling is achieved by passing the coolant through a single nozzle directed at the hot surface. Despite its great heat transfer coefficient of jets, heat transfer coefficient is very high in the middle of the jet and it degrades radially which is an inherent disadvantage of such design [16, 17].

1.3.2. Immersion cooling

Immersion cooling can be single phase or two phase. The working principle includes the equipment placed in an enclosure containing a dielectric fluid. In the case of two phase immersion cooling, the dielectric fluid has a low boiling point. In this way, the fluid boils on the surface of the component and removes the dissipated heat from the device. The vapor created will subsequently condense on the walls of the container which are at temperatures below the saturation temperature of the vapor. This system does not need a pump and it has the following advantages:

- It allows many devices to be densely packaged on the board
- Relatively high heat fluxes can be dissipated by this method
- It is simple and less expensive compared to some other methods

While the above advantages are highly appealing, the difficulty in maintaining such immersed cooled systems as well as the inadequacy of data on the long term effect of coolants on the electronics components, are among the drawbacks of this technique.

1.3.3. Heat pipe technology

This technology is widely used in portable electronic devices. A container like copper or aluminum with wicked surface is the primary component for a heat pipe device. At one side of the heat pipe, heat pumps in (evaporator) and the vapor starts to flow towards the cold end of the heat pipe where it condenses and releases the heat. The liquid will then travel back through the wicked surface to the hot region and circulation continues. This system needs no pump but there is a limited amount of heat that it can carry.

1.3.4. Thermoelectric (Peltier) coolers

This technique has the lowest COP of all the mentioned cooling strategies [18]. However, it can be used for hot spot mittigation through hybrid designs which involve microchannel heat sinks and thermoelectric coolers simultaneously [18].

1.3.5. Single phase liquid cooling

This is probably the most frequently used technique in the industry [19]. For such a system a pump is used instead of a fan in air cooled system which adds to the complexity, weight and cost of the equipment. Microchannel heat sinks can provide heat transfer coefficients in the range of 300-1000 W/cm^2K and with the flow range of 1-2 L/min, pressure drops in the range of 15-150 kPa are anticipated [14]. Disadvantages of this technique include the high pressure drop, low COP and temperature non-uniformity in the chip. However, single phase liquid cooling is simple in operation, it has robust design criteria and it is relatively cheap. Hence, greater effort is needed to improve the thermal performance of this method by enhancing the transport phenomenon at small scales. In the next section these enhancement techniques will be briefly discussed.

1.4. Heat transfer enhancement for single phase cooling

As mentioned previously, among all of the cooling techniques, microchannel heat sinks with single phase flow have probably the simplest working principle for high heat flux dissipation. Considering the fact that heat fluxes up to 1kw/cm^2 are anticipated in advanced electronics and power electronics, in order to meet this power dissipation demand, a heat transfer coefficient as high as 500,000 W/m^{2}K is needed assuming an average wall to fluid temperature difference of 20 K [14]. This indeed emphasizes the high demand for heat transfer enhancement techniques in single phase liquid cooling.

Microchannels provide high heat transfer area to volume ratio and due to their small scale, their flow regime is laminar. As the heat transfer coefficient for laminar regime is inversely proportional to hydraulic diameter, microchannels have high heat transfer coefficients and at the same time since pressure drop increases by D_h^{-4}, hydraulic diameter, pressure drop for microchannels is relatively high and it further decreases the COP.

In order to enhance the COP of single phase flow microchannel devices, heat transfer can be enhanced through mechanisms such as surface treatment like nano-structured microchannels [20] or microchannels with rough surfaces [21]. One of the enhancement methods for single phase convection is to invoke chaotic advection in the system. Chaotic advection will increase the mixing in the channel and it enhances heat transfer as the result. Other methods include disturbing the boundary layer formation [22] and mixing enhancement [23].

Wavy walled passages are among the configurations which are believed to enhance transport phenomena by employing chaotic advection. Considering a wavy walled microchannel and by defining a spatial wave function for the side walls, wavy, out of

phase, and converging-diverging configurations are created, Figure 1-6. In this thesis with the application of electronics cooling in mind, converging-diverging configurations will be studied numerically and experimentally.

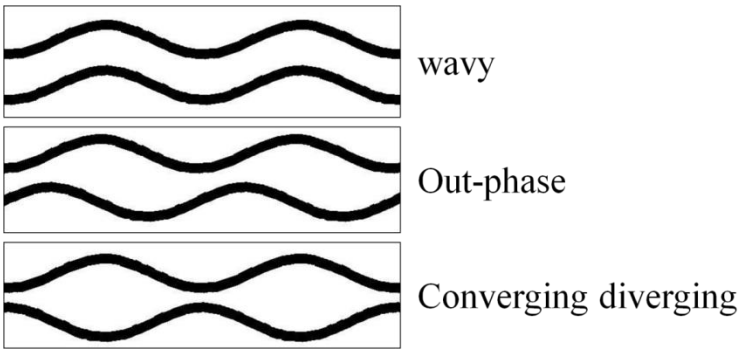

Figure 1-6. Different wavy walled microchannel configurations.

1.5. Objectives

The specific objectives of this research are to:

- Numerically investigate the hydro-thermal performance of the developing and fully developed flow in converging-diverging microchannels with different geometrical parameters and at different *Re.*
- Experimentally validate the numerical results for configurations with different levels of wall waviness.
- Analyze the problem from dynamical systems' point of view and explain the association between the heat transfer enhancement and the strength of chaotic advection.
- Introduce a novel active cooling method which provides strong chaotic advection at smaller *Re* and moderate pressure drop to further improve the hydro-thermal performance of the cooling system.

1.6. Scope

The scope of the research includes:

- Careful and systematic numerical investigation of converging-diverging microchannels to obtain accurate flow behavior and heat transfer over a range of mass flow rate and geometrical parameters.
- Analysis of the numerical results from dynamical systems point of view and to stablish the relation between the thermal performance and the advection regime.
- Evaluation of the wavy walled microchannels for electronics cooling using experimental investigation and also to validate the numerical results further.
- Introducing the concept of chaotic advection near resonance and to numerically study the system over a range of flow pulsation amplitudes and frequencies.

1.7. Organization of the document

This thesis consists of 8 chapters. In the first chapter, a brief background on cooling technologies is provided and single phase liquid cooling is introduced as a robust solution for a wide variety of applications. Heat transfer enhancement techniques are briefly reviewed subsequently and microchannels with wavy walls that can promote chaotic advection are introduced as a solution for heat transfer enhancement.

Chapter 2 is devoted to the literature review.

In Chapter 3 the physical problem is explained and computational domains as well as the governing equations are discussed. In the final section of the chapter dynamical systems are introduced and the theory of chaos is explained through an example.

In Chapter 4 fully developed fluid flow and heat transfer in converging-diverging microchannels is discussed.

In Chapter 5 an investigation on developing flow in converging-diverging microchannels is presented.

In Chapter 6 an experimental apparatus is introduced which is used to characterize the flow and heat transfer performance of wavy walled microchannels. The experimental results are compared with two boundary conditions: (1) constant temperature and (2) conjugated condition and it is shown that the constant temperature boundary condition being considered in our numerical investigations is a valid boundary condition due to high efficiency of the fins.

In Chapter 7 pulsatile flow in wavy microchannels is investigated and the concept of chaotic advection near resonance is introduced as a solution to enhance transport phenomenon at small scales.

In Chapter 8 conclusion and future works are discussed.

Sample uncertainty analyses are presented in Appendix A.

Chapter 2. Literature review

Greater system density and as a result higher speeds require innovative cooling technologies to be implemented for modern electronics. Recent generations of supercomputers use advanced methods of cooling for both processors and memory chips [24, 25]. Cloud computing as the future trend for computer industry needs data centers and server farms for which the cooling constitutes a huge fraction of the operational cost [26]. Having these facts in mind, development of appropriate and efficient methods of cooling that address current needs and future demands is desirable.

By reaching their acoustic threshold and cooling capacity, air cooling systems are harder to cope with [26]. In a review done by Agostini et al. [27], four different technologies that can address the high heat removal demand were introduced and it was mentioned that while single phase liquid cooling is a short term solution, two phase technology is the promising trend for the future of cooling technology. Surveying two-phase germane literature, it is inferred that stable performance of these cooling techniques is the main challenge and active controlling methods may even be needed for them [11]. The Boiling mechanism is inherently efficient however, it suffers from low critical heat flux (CHF) and low heat transfer coefficient [14, 28]. On the other hand, single phase liquid cooling is much simpler in principle and more stable, thus rendering this the preferred solution for certain applications. Moreover, as highlighted by Khan and Fartaj [29], it should be noted that the proposed enhancement technique is not solely for electronics cooling applications and can potentially find its way to all heat transfer devices and microchannel heat exchangers.

This literature review is composed of four sections. In the first part, the literature related to corrugated channels is discussed while in Section 2.2 chaotic advection in fluidic

systems is reviewed. The last two sections are devoted to pulsatile flow enhancement techniques and unsteady flow in wavy walled passages respectively.

2.1. Corrugated channels for transport enhancement

The first use of converging-diverging channels to enhance transport phenomenon goes back to early 70s when such a configuration was used to enhance mass transfer in a membrane oxygenator [30]. Sobey and Bellhouse later collaborated and such a configuration was studied numerically and experimentally [31, 32]. They performed 2D unsteady numerical simulations investigating two parameters, *Re* and amplitude of the wavy wall. Based on their study, flow structures for steady and pulsatile flow regime were determined and they concluded that there is a critical *Re* after which separation happens for steady flow in symmetrical sinusoidal channels.

Tatso Nishimura et al. investigated converging-diverging channels with conventional size. In their early work, the flow patterns of steady flow in the converging-diverging channel of Bellhouse [30] for *Re* of 100 to 10000 [33] were studied numerically and experimentally. From their experiments, it was observed that after *Re* = 350, the fluid flow became unstable where it was predicted to be steady by their numerical simulations. They claimed that laminar flow exists at *Re* less than about 350, and a subsequent increase of *Re* results in turbulent flow. They also observed that in the laminar flow range, friction factor is inversely proportional to *Re* while in the turbulent range, it is independent of *Re*. The flow patterns observed by them as well as the friction factor as a function of *Re* are presented in Figure 2-1.

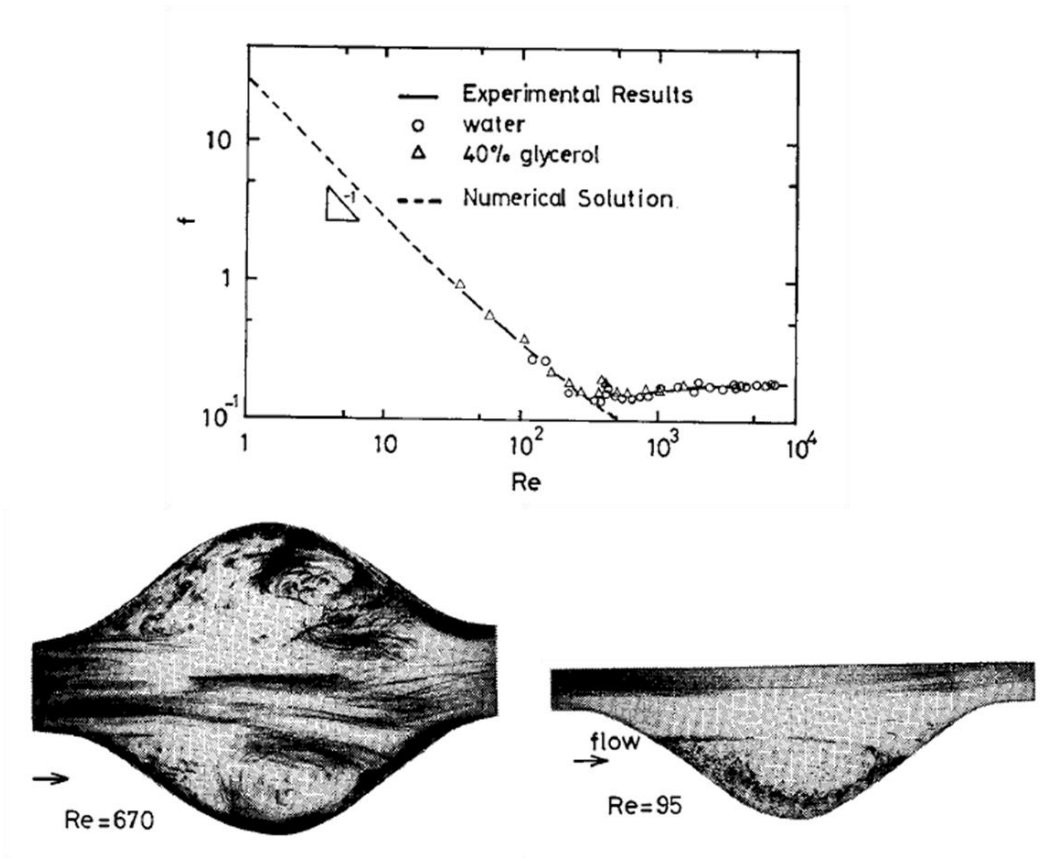

Figure 2-1. Friction factor relation with *Re*. Flow patterns [33].

In another study by Nishimura et al., for a geometry similar to the Oxford membrane blood oxygenator [30], mass transfer characteristics were investigated by Leveque theory and electromechanical method [34]. The study was done for $100 < Re < 10000$ for both laminar and turbulent regimes. It was concluded that for laminar flow, mass transfer enhancement of the wavy channel is barely noticeable as compared to the corresponding straight microchannel, but it becomes remarkable for turbulent flows (Re > 350), Figure 2-2. *L* in Figure 2-2 denotes the mass transfer measurement length and as it can be seen for turbulent regime, the results are invariant to the length of mass transfer. It should be noted that the definition of equivalent straight channel used in their investigation is also used for current study. The width of the straight channel is equal to the average width of

the converging-diverging channel thus, equal *Re* means equal mass flow rate for the cases with equal aspect ratio.

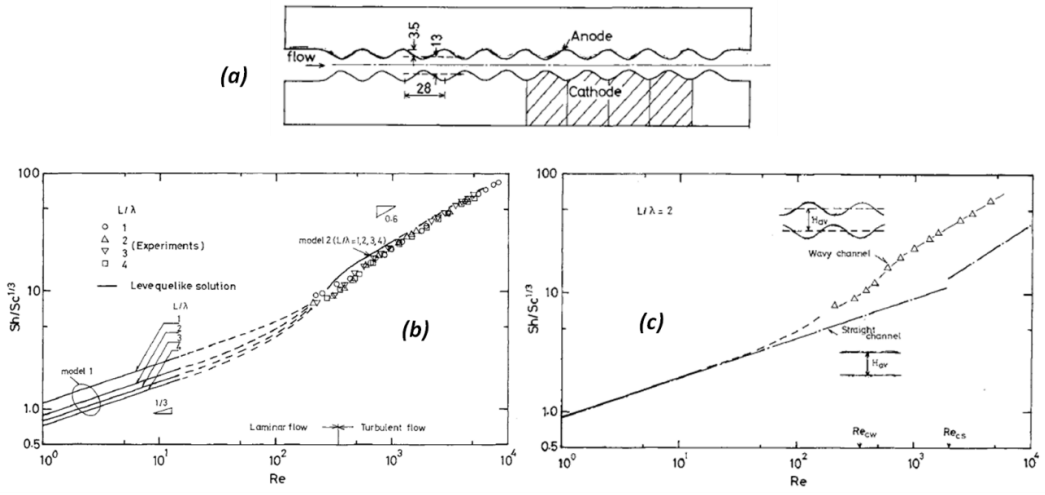

Figure 2-2. a) Experimental setup and position of electrodes. b) Average Sherwood number. c) Comparison of Sherwood number for wavy and straight channel. [34]

In the study Nishimura's group did for moderate Reynolds numbers, the development from laminar to transitional flow was investigated [35], and they concluded that although it is widely believed that the flow pattern of such a configuration is 2D, there may be three dimensional flow structures even at small *Re*. This indeed is proven in our study by observing the vortical structures in the microchannels.

Blancher et al. [36] addressed the effect of Tollmien-Schlichting waves on heat transfer in converging-diverging configurations performing linear stability analysis by integrating time dependent Navier-Stokes and energy equations. 2D, laminar, incompressible, time dependent, periodically fully developed flow was considered in their investigation with the Bellhouse geometry [30].

Greiner et al. studied V shaped symmetrical grooved channel by using a full channel 2D model for studying the developing flow and a 3D single furrow model for the fully

developed condition [37-42]. Using the spectral element technique, Navier-Stokes equations of three dimensional flow and convective heat transfer in a fully developed symmetrical grooved passage was solved for $180 < Re < 1600$. The evolution of the flow structure from the steady 2D flow to coherent travelling waves and then three dimensional mixing is reported in their paper [39]. They also stated that 2D simulations cannot correctly predict averaged value of friction factor or heat transfer coefficient for higher Reynolds numbers. From a comparison they made with the measured quantities, less than 20% error was observed between the experiments and 3D simulations done. One important point about this paper is that they both tested constant body force and constant flow rate as the periodic boundary condition. They claimed that the results are more or less identical, and flow rate unsteadiness (in the case of a constant body force) has minimum effect on the transport phenomenon at critical Reynolds numbers. Using the same method, periodic flow in an intermittently grooved passage in 2D was also studied by this group [37]. Their results showed that intermittently grooved passages may even have higher heat transfer for a given pumping power than the fully grooved channels.

Minichannels with semicircular cross section were investigated by Fletcher et al. [43-48]. Their recent paper on periodic tortuous passages showed that the flow will become fully developed in a long channel with enough repeating units. They also managed to observe the transition to chaotic flow by analyzing the velocity signal and also hydro-thermal performance of the channel [48]. Periodic shapes like trapezoidal channels with applications in compact heat exchangers were also examined by this group [45]. Among the shapes being studied, the swept zigzag channels provided the greatest heat transfer performance.

Heidary and Kermani [49] analyzed the thermal performance of nanofluids in wavy microchannels and claimed that nanofluids perform better in terms of thermal

performance compared to normal fluids. In a similar study performing a numerical analysis with a 2D model, Ahmed et al. [50] observed that copper-water nanofluid shows better thermal performance compared to normal fluid while the pressure drop penalty was marginal.

Gong et al. [51] did a parametric study on microchannels with wavy walls. Specifically, the effects of geometrical parameters related to wall waviness and channel aspect ratio for $5 < Re < 150$ were studied. Based on the range of parameters they examined, it was claimed that the wavy microchannels perform better compared to converging-diverging configuration. It should be noted that this study is among the very few parametrical studies done on wavy walled microchannels.

Mohammed et al. [52-54] numerically investigated the configurations of zigzag, wavy, and step microchannel heat sinks. The Hydro-thermal performance of these configurations were compared with plain microchannels while the zigzag configuration showed the highest pressure drop and the best thermal performance while the step configuration showed better hydraulic performance with lower thermal performance compared to straight microchannel heat sink.

Xia et al. [55, 56] studied the microchannels with cavity structure and fan shaped reentrant cavities. Their results showed that slipping over the reentrant cavities reduces the friction factor, but seriously impedes heat transfer (our observations support this finding). However, their results lack a relation between the flow structure and heat transfer performance. Also, presence of chaotic advection and its effect was not reported by them.

2.2. Chaotic fluidics

Chaotic advection was first introduced by Hassan Aref [57] on the topic of stirring in a tank. He showed that a well-defined laminar flow field from the Eulerian point of view can generate stochastic advection patterns from the Lagrangian point of view. Chaotic advection has gained more attention with the recent development of microfluidics [58-62]. Microchannels due to their small scales exhibit laminar behavior and finding ways to enhance their mixing was of interest to researchers for applications like lab-an-a-chip [59, 63] and micromixers [60].

While three-dimensional configurations similar to the ones depicted in Figure 2-3 are used to generate chaotic advection in micromixers [59-61], planar designs are needed for heat transfer applications due to their manufacturability and the level of compactness needed for thermal systems. Wavy walled microchannels are among the novel planar designs that may exhibit chaotic behavior and due to their manufacturability with metallic materials, are among the possible solutions for passive heat transfer enhancements [23, 64, 65].

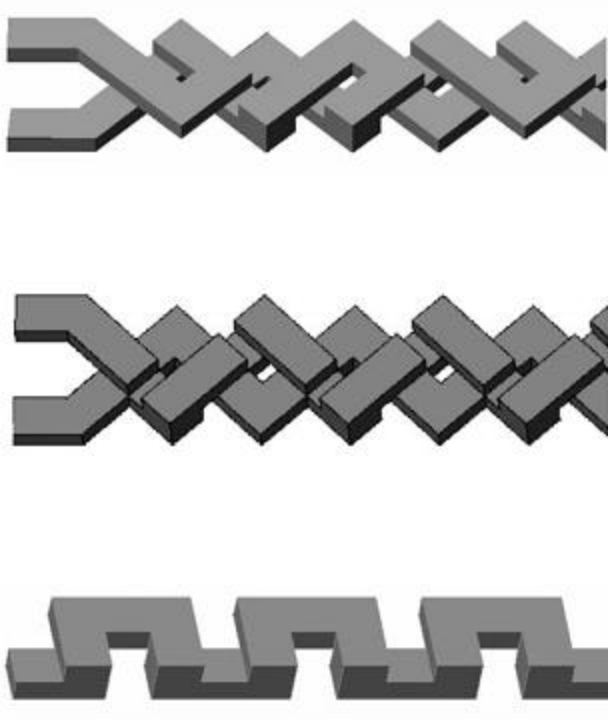

Figure 2-3. Three dimensional configuration of micromixers invoked in [60].

Cristina H. Amon and A. M. Guzman studied converging-diverging channels as a dynamical system [66-68]. They used direct numerical simulation to observe the transition between different flow regimes in converging-diverging channels [66]. Self-sustained oscillatory flows were observed in such configurations and a scenario similar to the Ruelle-Takens-Newhouse (RTN) scenario of the onset of chaos was observed. The RTN scenario is characterized by a finite number of successive supercritical Hopf bifurcations as the control parameter –*Re* in this case- changes. As *Re* is increased, the flow regime exhibits a sequence of periodic, quasi-periodic and eventually aperiodic or chaotic regimes. Analyzing the velocity signal at a certain point in the domain, a periodic regime shows itself by a single peak in the power spectrum of the velocity profile while quasi-periodicity comes with two or three fundamental frequencies. The chaotic behavior for this regime is indicated by a broadband Fourier power spectrum, Figure 2-4.

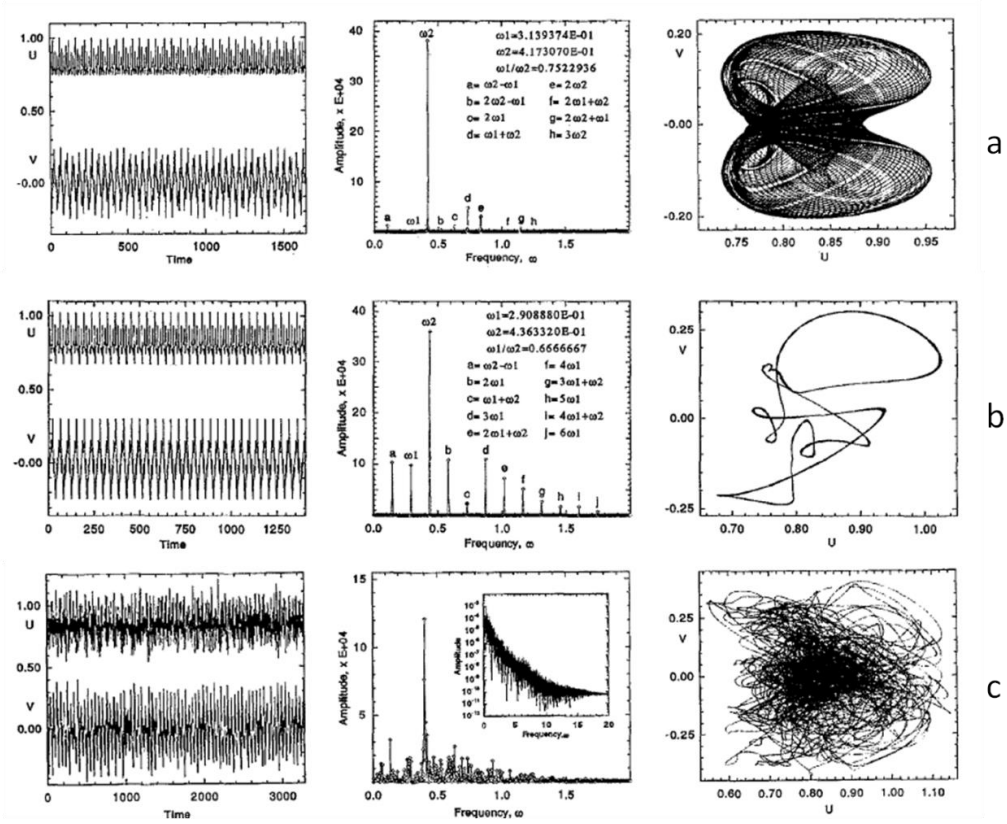

Figure 2-4. Streamwise and crosswise velocities as a function of time. Fourier power spectra of the *u* velocity, and state space trajectories of *v* vs *u* for the converging-diverging channel flow: a) periodic b) quasi-periodic c) chaotic behavior. [66]

In an study by Guzman et al., DNS (spectral element method) was used for a single geometry at $10 < Re < 850$ [67]. The chosen route to chaos was of interest in this study and with the dynamical system parameters calculated, results obtained strongly supported the RTN route to chaos for these configurations. Dynamical system techniques such as autocorrelation functions, fractal dimensions and Eulerian Lyapanov exponents were used to characterize the laminar, transitional and chaotic flow regimes. Flow evolution from laminar to low-dimensional deterministic chaos was well investigated by the above techniques. It was claimed that there are critical *Re* at which the flow regime transitions in stages as follows:

$$\text{Laminar} \rightarrow \text{Periodic} \rightarrow \text{Quasi} - \text{Periodic} \rightarrow \text{Chaotic}$$

In the recent investigation of Guzman et al. [69], waviness λ and expansion factor γ of the channel geometry are introduced as the main parameters which determine the transition scenario observed for converging-diverging channels. The results of 2D simulation showed that for greater aspect ratio, there is a frequency-doubling transition scenario which is characterized by one Hopf flow bifurcation where further increase in the *Re* will just result in periodic flows. For a smaller expansion factor (the ratio of widest width of the channel to the narrowest width) RTN scenario was observed. The technique used to detect the Hopf bifurcation is the velocity signal analysis with FFT method explained previously. It should be noted that the model used in the investigation by this group was 2D and further investigation for 3D models on the transition scenario is needed. A similar study on flow bifurcation in asymmetric wavy wall channels was also performed by Guzman et al. [70]. Again they observed that the transition scenario was a strong function of geometrical parameters, a claim yet to be investigated for 3D configurations.

A configuration with one furrow similar to Bellhouse et al. [30], under periodic boundary condition with imposing pressure drop in the streamwise direction was investigated by Wang et al. [71]. The flow medium was air and they observed that converging-diverging channels can show a great enhancement in a certain range of parameters. They also observed the flow regime change reported previously by Guzman et al. [66-68]. However, they claimed that these transition scenarios greatly depend on the periodic boundary condition imposed.

Stalio et al. studied a 2D sinusoidal symmetric wavy channel using direct numerical simulation [72]. Their observation also supported the transition scenario of periodic, quasi-periodic and chaotic for their configuration.

Sui et al. [23, 64, 65] studied the effect of chaotic advection and the transition to chaos in wavy microchannels. Their results showed that presence of chaotic advection in the system can enhance the thermal performance. They also demonstrated the potential of wavy microchannel heat sinks for hot spot mitigation by varying the wall waviness. Their investigation on transition to chaos for wavy microchannel [65] showed a similar scenario to RTN scenario of the onset of chaos.

2.3. Pulsatile flow

The early work of Faghri et al. [73] on fully-developed pipe flows with pulsation was an analytical approach to the pulsatile flow problem. Yakhot et al. [74] numerically studied pulsating laminar flow in rectangular ducts trying to characterize the flow based on a non-dimensional parameter representing the pulsation frequency and channel dimension. Phase lag and the amplitude of the induced oscillating velocity and wall frictional force were analyzed in their work.

In an experiment done by Habib et al. [75], pulsating air flow in a pipe was investigated for uniform heat flux condition for parametric space of $780 < Re < 1987$ and $1\text{Hz} < f_p < 29.5\text{Hz}$ where f_p is the pulsation frequency. Their result revealed that the average mean Nusselt number is highly affected by pulsation frequency and less by *Re*. In a work done by Sabry et al. [76], an analytical approach was chosen for thermally fully-developed flow and FEM method for the developing region, while investigating laminar pulsating flow for uniform heat flux condition. They reported marginal enhancement for both developing and fully-developed regions with the developing region showing greater sensitivity.

A static device was used in the study of Zeng et al. to generate pulsed flow, and they observed enhancements of up to 10% in their experiments [77]. Experimental results on

arrays of heated blocks in a pulsating channel flow showed that there is a frequency at which thermal enhancement is a maximum [78], a phenomenon that is also observed in our study.

Heat transfer in a circular isothermal duct under pulsation flow condition was tested numerically by Himadri et al. [79] while the flow was developing thermally and hydrodynamically within the parametric space of pulsation frequency from 1Hz to 20Hz and amplitudes less than 100% for Re = 200. It was observed that pulsation had no effect on the time-averaged heat transfer.

Pulsatile flow in curved passages was explored in a fundamental study done by Sumida [34]. It was observed that pulsating the flow reduced the entrance length [80]. The effect of flow rate and geometry on pulsating flow passing through corrugated rectangular shape channel was investigated experimentally by Olayiwola et al. [81]. They reported that no significant enhancement was observed at very low (Re ~ 100) and very high (Re ~ 1000) mass flow rates. In a recent experimental study by Persoons et al. [82], enhancements were observed for flow pulsation in straight minichannels. Our results on pulsatile flow with a straight 2D model showed no enhancement which we believe to be due to the manifold effect.

2.4. Unsteady flows in wavy walled architectures

Sobey et al. numerically calculated the pattern of the fluid flow for pulsatile regime in wavy walled passages and identified three parameters which govern the flow, i.e., Pulsatile Reynolds number, Strouhal number (St) and Reynolds number. The Strouhal number is an important parameter in oscillatory flows and based on their observation they concluded that at large St, i.e., O(1), viscosity dominates the flow and inertial separation never occurs regardless of Re. On the other hand, for St of O(10^{-4}) a true quasi-steady

flow exists. Between these orders, there is an intermediate range in which inertial separation occurs but the flow does not behave in a quasi-steady fashion [83]. Strouhal number is an indicator of oscillatory flows with the definition:

$$St = \frac{hf}{U} \tag{2-1}$$

Where in their case, h is a characteristic length scale, half of the narrowest part of the channel, f is the forced oscillation frequency and U is a velocity which id the peak velocity with the assumption of flat velocity profile at narrowest cross section. Figure 2-5 shows a diagram for Strouhal number vs. Reynolds number. They suggested that the region dominated by inertia, region II in the Figure 2-5, is effective for mass transfer enhancement.

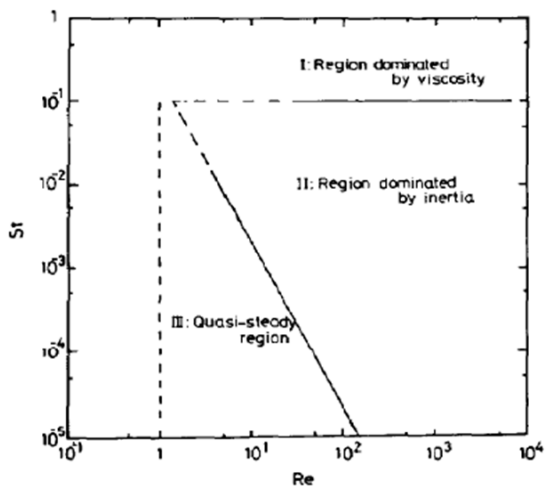

Figure 2-5. Flow diagram proposed by Sobey[83] for a sinusoidal wavy walled channel.

In another study, numerical investigation and flow observation of oscillatory flow in asymmetric channels at intermediate Strouhal numbers were performed by Sobey et al. [84]. Two reasons were mentioned for such a study: the converging-diverging configuration may suffer from imperfect manufacturing, such as misaligned channel

walls and secondly, maybe deliberate introduction of asymmetries would augment the vortex-mixing process further. Misalignment between the upper and lower walls was created by introducing a phase difference between the sine function of the walls. Again, the flow structure was investigated in this study but they did not provide any information about the enhancement of the transport phenomenon.

Oscillatory flow in furrowed channels was also of interest to Nishimura's group [85-91]. In the study by Nishimura et al. [90], oscillatory viscous flow in a symmetric wavy wall channel was investigated. The experiments were carried out under the condition of $5 < Re < 200$ and $0.06 < St < 0.3$. Womersley number, $\alpha^2 = St.Re$, showed a critical role in the structures formed in the channels. They claimed that for small values of α^2, $\alpha^2 < 4$, steady streaming consisting of a symmetrical pair of recirculation within each furrow, i.e. two-vortex system, is observable. And when α^2 exceed 4, a new secondary counter-rotating pair of recirculation appears near the centerline of the maximum cross section in addition to primary recirculation observed for values of $\alpha^2 < 4$, i.e., four-vortex system. It should be noted that these vortical structures are formed for the oscillatory flow regime with net flow rate of zero and they should not be confused with vortical structures formed with constant flow rate.

Mass transfer enhancements in asymmetric and symmetric channels with pulsatile flow were studied by Nishimura et al. [92, 93]. An electrochemical method was used for the experiments and fluid flow dynamics were visualized both experimentally and numerically. From the comparison between the symmetric (converging-diverging) and asymmetric (wavy) channel, it was concluded that an asymmetric channel shows larger mass transport enhancement for a wider range of flow parameters, i.e., frequency and amplitude of fluid oscillation. Figure 2-6 depicts the experimental test setup as well as the mass transfer result for steady state flow. From this figure it can be seen that for the

steady flow regime, i.e. $Re_S < 300$, the symmetric channel leads to a larger value in the mass transfer rate than the asymmetric channel. However, in the unsteady flow regime, there is no difference in terms of mass transfer rate. On the other hand, for pulsatile flow, Sherwood number (*Sh*) becomes larger than the equivalent steady value which can be related to the dynamical behavior of vortices. Their results showed that the enhancement factor for Sherwood number increases with the frequency of fluid oscillation as the net flow Reynolds number increases.

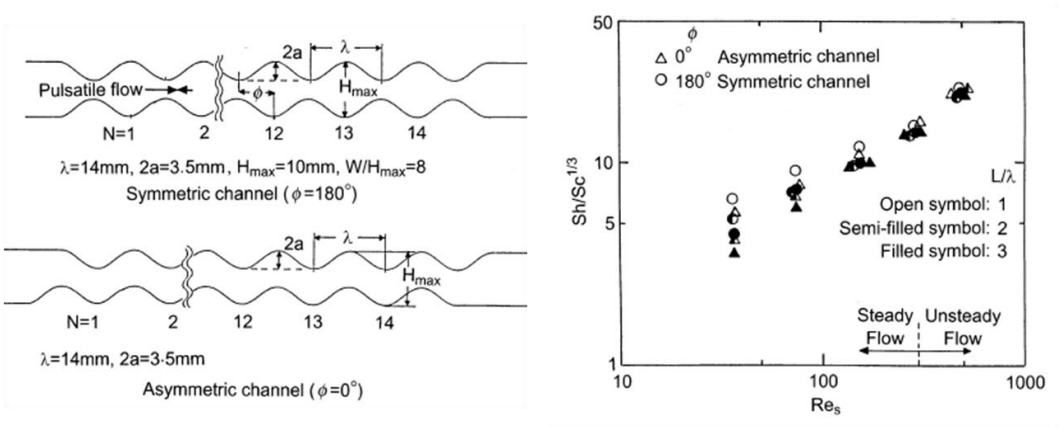

Figure 2-6. Experimental test section and Sherwood number vs. *Re* for symmetric and asymmetric channels. [92]

2.5. Conclusion

Reviewing the literature, although different studies have been performed on converging-diverging configurations, most of them have been on a single architecture. Thus, a full parametric study which considers converging-diverging structure for applications like microchannel heat sink is still lacking. The recent study performed by Gong et al. [51] is among the few parametric studies; however the range of *Re* considered in their investigation has been less than 150. Moreover, no information regarding the presence of chaotic advection and its effect on heat transfer is provided. Our study on the other hand considers *Re* up to 800 and the fluid flow and heat transfer characteristics are established.

Due to the fact that most of the literature related to the experimental studies are based on conventional dimensions, there is also a need for experimental investigation on converging-diverging configuration and especially for microchannel heat sink application. The experimental results provided in this thesis are performed for different levels of wall waviness ($0 < \lambda < 0.15$) across *Re* ranging from 100 to 800. The comparison performed between the experimental results and the numerical simulations with different computational domains provides a good benchmark for future studies and actual thermal management system designs.

The terminology of chaotic advection near resonance which considers the pulsatile flow in wavy walled microchannels is introduced for the first time for such designs. Although oscillatory flows, with net flow rate of zero, for such configurations have been studied previously, the slightly modulated microchannel design under pulsatile regime is studied for the first time in this thesis and the idea of chaotic advection near resonance is built based on the idea of chaos near resonance [94]. This concept has very good potential particularly if we consider that most of the micro-pumps are inherently pulsatile [95].

Chapter 3. Problem definition and methodology

3.1. Physical description

Figure 3-1 shows a typical configuration of microchannel heat sink used for back cooling of a chip. Heat is conducted from the bottom and is carried by the coolant going through the channels. The top of the channels is covered by a glaze which can be represented by an adiabatic condition. Figure 3-1b depicts the converging-diverging heat sink configuration investigated in the current study with the key geometric parameters being shown in Figure 3-1c.

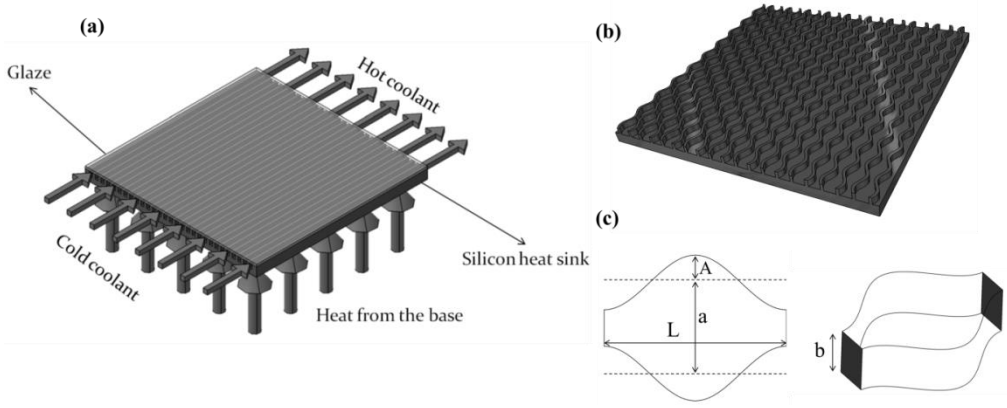

Figure 3-1. a) Physical configuration. b) Wavy walled microchannel heat sink. c) Key dimensional parameters.

From Figure 3-1 it is observed that there are five geometrical parameters which define the geometry:

- *A*: the wave amplitude of the wall
- *L*: the wavelength of a single furrow
- *a*: averaged width of the channel
- *b*: channel depth
- *N*: number of furrows for each channel

These parameters can be represented by three salient dimensionless parameters as follows:

- **Aspect Ratio**, the ratio of width to depth of the channel, $S = a / b$
- **Waviness**, the ratio of wall amplitude to its wavelength, $\lambda = A / L$
- **Expansion factor**, the ratio of widest width of the channel to the narrowest width, $\gamma = (a + 2A) / (a - 2A)$

With this definition, having two channels with equal waviness and different expansion factor is possible if wall waviness is kept constant and the distance of the side walls are altered. Thus, expansion factor γ is complementary to the waviness λ. From the above definitions, waviness of a straight channel λ is equal to zero while expansion factor γ is equal to 1.

In the parametric study designed to investigate the effect of geometrical configuration on hydro-thermal performance of the wavy walled microchannels, depth of the channel *b* is kept constant and by changing the average width *a*, different aspect ratios *S* are achieved. To achieve different levels of wall waviness, wall amplitude *A* is increased while average width *a* is kept constant, in this way the amount of volume occupied by two channels with the same aspect ratio *S* and different waviness λ would be the same. Figure 3-2 shows a typical converging-diverging configuration for a case with *S* = 0.8 and different values of wall waviness λ. As it can be seen, the equivalent straight microchannel for all the cases is the same and it is the case with λ = 0. Side walls are sinusoidal functions with the phase difference of π, $y = A\,Sin\,(2\pi x / L)$ and $y = A\,Sin\,(2\pi x / L + \pi)$, where *A* is the amplitude and *L* is the wavelength. Considering the way the channels are constructed, designs with equal aspect ratio, *S*, will have the same equivalent straight microchannel for which the width is equal to the averaged width of the converging-

diverging channel *a* and in this way average hydraulic diameter will be the same for the microchannels with the same aspect ratio *S*. Average hydraulic diameter for converging-diverging microchannel is defined based on the equivalent straight microchannel which has width of *a* and depth of *b*:

$$D_h = \frac{4a \times b}{2(a+b)} \tag{3-1}$$

In the case of 2D geometries, $b \to \infty$ and hence $D_h = 2a$.

Reynolds number for all the configurations is defined based on the average hydraulic diameter and the mean velocity of the equivalent straight microchannel, U_m:

$$Re = \frac{\rho U_m D_h}{\mu} \tag{3-2}$$

Based on the above equation, for the cases with similar aspect ratio *S*, the same *Re* will result in the same mass flow rate in the microchannels.

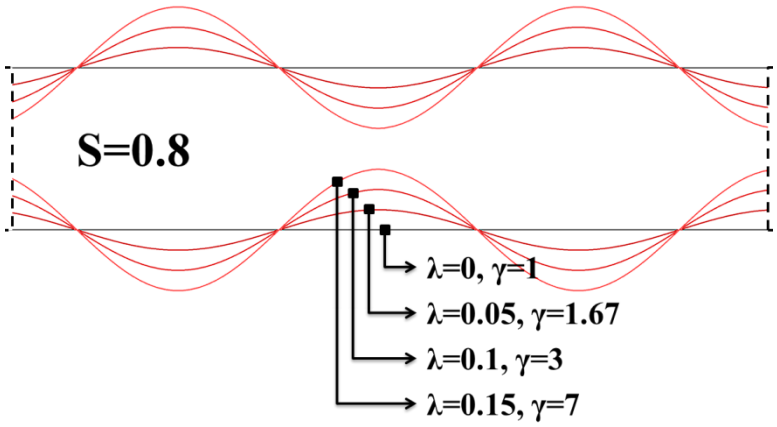

Figure 3-2. A typical configuration with *S* = 0.8 and different level of wall waviness. The equivalent straight microchannel is the one with *λ* = 0 for all the cases.

3.2. Computational domains

In order to study the fluid flow and heat transfer performance of converging-diverging microchannels, numerical studies are performed for configurations with four conditions:

1- Fully developed condition which considers a single furrow with periodic boundary condition at inlet and outlet and constant temperature at the walls, Figure 3-3.

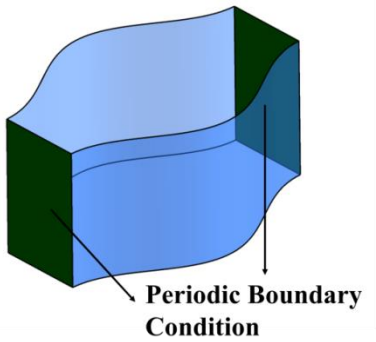

Figure 3-3. Computational domain for fully developed condition.

2- Developing condition which considers a single wavy microchannel with constant temperature boundary condition at the side and bottom walls and adiabatic boundary condition at the top wall, Figure 3-4.

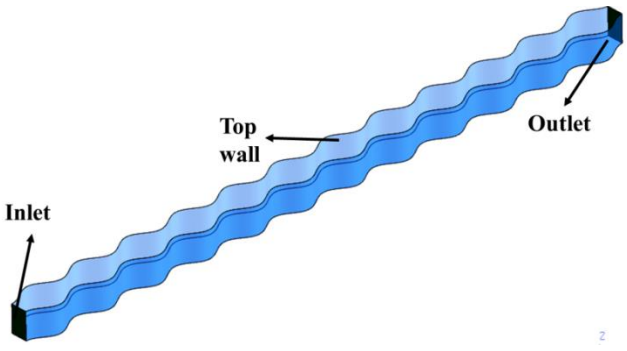

Figure 3-4. Computational domain for developing flow with constant temperature boundary condition.

3- Developing condition with conjugated domains which consists of extended inlet and outlet with symmetry boundary condition at the sides, Figure 3-5.

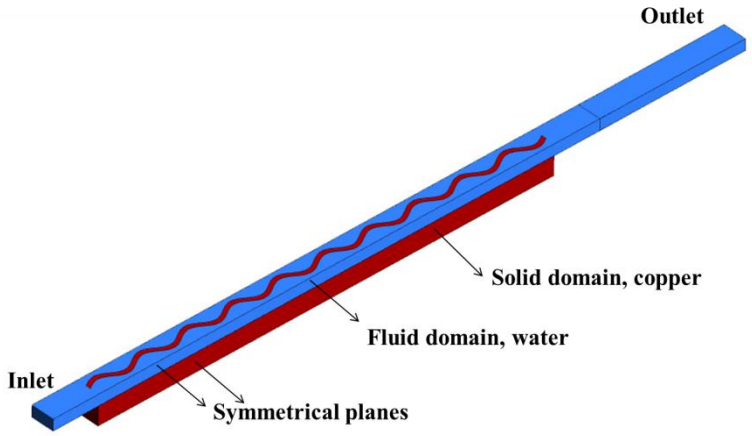

Figure 3-5. Computational domain for conjugated condition.

4- Pulsatile flow investigation which considers a 2D model for wavy channel and a pulsatile flow regime at inlet. Two thermal boundary conditions are considered for this study, constant temperature at walls and conjugated solid-liquid domains, Figure 3-6.

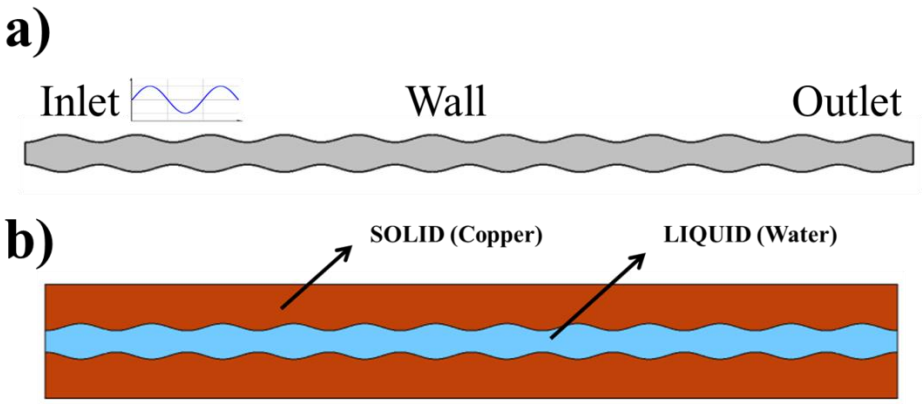

Figure 3-6. Computational domain for study of pulsatile flow in wavy walled channels. a) single channel with constant temperature boundary condition. b) conjugated domain with constant heat flux at solid boundary.

3.3. Governing equations

The minimum microchannel dimension in this study is greater than 10μm and as Obot [96] has proposed, under such conditions, the continuum assumption is valid. Thus, the classical Navier-Stokes and energy equations govern the pertinent transport processes. Laminar, incompressible flow is assumed for this investigation and in this way conservation of mass under incompressible flow assumption would be:

$$\nabla \cdot \mathbf{V} = 0 \tag{3-3}$$

where $\mathbf{V}$ is the velocity field and ∇ is the gradient vector, $\nabla = \frac{\partial}{\partial x}\hat{i} + \frac{\partial}{\partial y}\hat{j} + \frac{\partial}{\partial z}\hat{k}$.

The momentum equation is given as follows:

$$\frac{D\mathbf{V}}{Dt} = -\frac{1}{\rho}\nabla p + \nu\nabla^2\mathbf{V} \tag{3-4}$$

Where ρ is the density and ν is the kinematic viscosity. ∇^2 is the Laplacian operator, $\nabla^2 = \frac{\partial^2}{\partial x^2} + \frac{\partial^2}{\partial y^2} + \frac{\partial^2}{\partial z^2}$ and $\frac{D}{Dt}$ is the total derivative, $\frac{D}{Dt} = \frac{\partial}{\partial t} + u\frac{\partial}{\partial x} + v\frac{\partial}{\partial y} + w\frac{\partial}{\partial z}$.

Conservation of energy in fluid and solid domains is respectively given by:

$$\frac{DT}{Dt} = \left(\frac{k}{\rho C_p}\right)_{fluid} \nabla^2 T \tag{3-5}$$

$$\frac{\partial T}{\partial t} = \left(\frac{k}{\rho C_p}\right)_{solid} \nabla^2 T \tag{3-6}$$

where k is the thermal conductivity and C_p is the specific heat capacity.

The partial differential equations above are discretized and along with the appropriate boundary conditions, solved with finite volume method using either FLUENT or CFX packages. Grids for the above simulations are generated using either Gambit or CFX mesh. For the whole study, structured mesh was chosen to discretize the domains due to the better control this method provides over the range of parameters. An algebraic method was used for the structured mesh generation with uniform division in *x* direction. In *y* and *z* direction, expansion rate of 1.05 was considered which made the near wall grid denser. Grid independence test is performed for all the cases to have results independent of the mesh size. The results of grid independence study will be presented at the related section in the following chapters.

3.4. Fluid flow as a dynamical system

Based on the idea of similarity between the passive advection of a particle in fluid flow and a finite dimensional dynamical system, the term *Chaotic advection* was coined by American-Egyptian mathematician, Hassan Aref, in 1981 [57]. While the presence of chaos was very well established for dynamical systems [97], invoking the concept and representing it with a new terminology for advection problems in fluid flow was the main contribution done by Aref [76]. In the following section, we try to build a fundamental understanding of chaotic advection, a phenomenon present in wavy walled microchannels and responsible for the hydro-thermal performance of such designs.

3.4.1. Dynamical system

A *dynamical system* is a mathematical concept for which a fixed rule (*evolution rule*) determines the time dependence of a point in a geometrical space [97]. The dimension of a dynamical system is determined by the number of *state variables* which can uniquely

define the state of the system. These state variables form the state space of the dynamical system. A one dimensional dynamical system is mathematically represented by:

$$\frac{dx}{dt} = f(x) \tag{3-7}$$

And in general form:

$$\frac{d\mathbf{x}}{dt} = \mathbf{f}(\mathbf{x}, t) \tag{3-8}$$

is the mathematical model for a finite dimensional dynamical system where **x** is a vector in the state space and *t* is the time while **f** is the evolutionary rule. At any time, a dynamical system has a *state* which is represented by a vector in the *state space* of the system. As there is a fixed rule to describe the future state of the dynamical system, dynamical systems are *deterministic* and that means for a given time interval, there only exists one state following the current state.

Chaotic dynamics may be achieved even when the right hand side of the system of ODEs represented by Equation 3-8 is not that complicated. In the following sections, the definition of orbit and map will be provided and through the example of Lorenz model, the theory of chaos will be explained.

3.4.2. Orbits and maps

Trajectory or *orbit* is a collection of points related to the temporal evolution of the dynamical system starting from an initial position in the state space and its subsequent evolution based on the evolutionary rule [98]. The nature of the system shows itself through the shape of its corresponding orbit. A *periodic* dynamical system, a simple pendulum for example, has an orbit in the format of a closed loop while a period-two system has two loops in its orbit. A *chaotic* system has an irregular orbit with no

periodicity. In fact, it can be stated that a chaotic system is a period-infinity dynamical system. Figure 3-7 shows orbits for periodic, periodic-two and chaotic 3D systems.

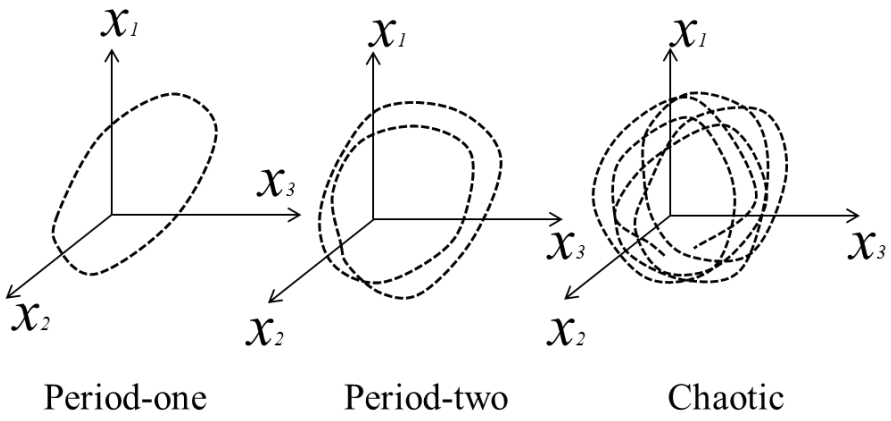

Figure 3-7. Orbit of periodic and chaotic dynamics for a three dimensional system.

In order to reduce the complexity of the system analysis, it is possible to reduce the dimension of the system by studying the system's Poincaré map instead of the orbit. A Poincaré map can be created by passing a plane through the orbit of a system, Figure 3-8. In this way, the Poincaré map for a periodic system would be a single point and for a period two system it would be two points. The Poincaré map for a chaotic system would be stochastic placement of points in the map.

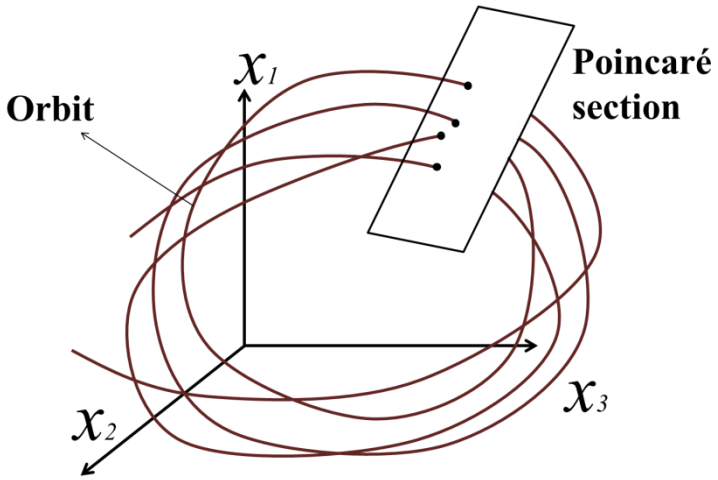

Figure 3-8. Poincaré map related to a typical 3D dynamical system.

3.4.3. Chaos theory through an example, Lorenz model

One of the first examples of chaos theory was introduced by meteorologist Lorenz in 1963. In fact, the term 'butterfly effect' was first used by him [99]. Lorenz obtained a set of equations through his investigation of Rayleigh-Benard convection, and presented a three dimensional dynamical system to study the weather behavior. The Lorenz model consists of three ODEs with quadratic couplings as:

$$\begin{aligned} \frac{dx}{dt} &= -\sigma(x-y) \\ \frac{dy}{dt} &= -xz + rx - y \\ \frac{dz}{dt} &= xy - bz \end{aligned} \qquad (3\text{-}9)$$

where x, y and z are the state variables and σ, r and b are the system parameters.

Lorenz observed that for some set of system parameters, the evolution of the system will become highly sensitive to the initial condition. For example starting from $\begin{pmatrix} x \\ y \\ z \end{pmatrix} = \begin{pmatrix} 15 \\ 10 \\ 40 \end{pmatrix}$,

deviating by as little as 0.005 from the initial condition results in two completely different behaviors based on the value of *r*. Figure 3-9 shows the temporal evolution of the system in *zx* plan. It is seen that for $r = 10$, the trajectories of the two initial conditions are similar (regular dynamics) while for the value of $r = 20$, trajectory of the two initial conditions in the state space are completely different (chaotic dynamics). This behavior is named *sensitivity to initial condition* and is a characteristic of chaotic systems. When a system is highly sensitive to initial condition, a small perturbation in the current trajectory will lead to a significantly different future behavior and that is the reason why chaotic systems are *unpredictable* despite being *deterministic*.

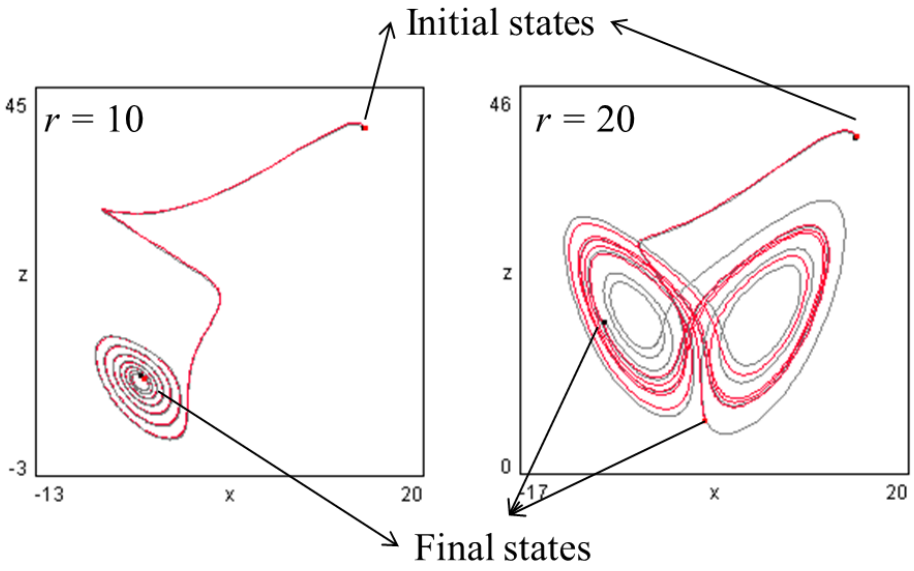

Figure 3-9. Temporal evolution of two initial conditions deviated by 0.005 based on the Lorenz equations for a regular dynamic (left) and a chaotic dynamic (right)

3.4.4. Chaotic advection

Passive advection of a massless particle in a fluid field means that the particle is so inert that it just follows the flow. In fact for single phase flow, each fluid particle undergoes a passive advection for which it can be written:

$$\mathbf{V}_{\text{particle}} = \mathbf{V}_{\text{fluid}} \tag{3-10}$$

The velocity of the particle can also be given as the rate of change in its position:

$$\mathbf{V}_{\text{particle}} = \left(\frac{dx}{dt}, \frac{dy}{dt}, \frac{dz}{dt} \right) \tag{3-11}$$

where *x, y* and *z* are the position coordinates of the particle.

The velocity field of the fluid $\mathbf{V}_{\text{fluid}}$ may be obtained analytically for simple flows or numerically for complex geometries and thus it is a known parameter:

$$\mathbf{V}_{\text{fluid}} = (u, v, w) \tag{3-12}$$

where *u, v* and *w* are the velocity components which are functions of space and time.

Based on Equation 3-10 and considering Equations 3-11 and 3-12, a system of first-order ordinary differential equations (ODEs) can be written as:

$$\begin{aligned} \frac{dx}{dt} &= u(x, y, z, t) \\ \frac{dy}{dt} &= v(x, y, z, t) \\ \frac{dz}{dt} &= w(x, y, z, t) \end{aligned} \tag{3-13}$$

which is the Lagrangian description of fluid motion.

As discussed previously, a set of ODEs like the ones presented in Equation 3-13 can easily exhibit chaotic dynamics even if the right hand side is not that complicated. A chaotic system is strongly dependent on initial condition which means that the orbit of the system would totally be different if the initial condition is even slightly different. In the analogy between the advection problem from Lagrangian point of view and a finite size

dynamical system, the orbit is identical to the pathline of the particle. Hence, in a chaotic advection regime, two fluid particles which are very near to each other may undergo a completely different trajectory which contributes to mixing.

The presence of chaos in advection is simply important because it enhances mixing. In fact, mixing by chaotic advection lies between regular advection and turbulence. When turbulence is hard to achieve, chaotic advection can potentially enhance the transport phenomena. Hence, for the case of microchannels which the small scales dictate the flow regime to be mostly laminar, provoking chaotic advection in the channel can help to enhance heat transfer.

3.4.5. Poincaré map for wavy walled microchannels

As mentioned previously, Poincaré maps will help to better understand the dynamical behavior of the systems. In the analogy between the finite dimensional dynamical system and advection from Lagrangian point of view, a Poincaré map can be created by crossing a plane and the pathline of a particle or a set of particles. In the next sections, Poincaré maps for fluidic systems will be discussed.

3.4.5.1. Developing flow

Devices which are used for mixing can be categorized as closed (batch) systems and open/continuous (in-out) systems [100]. Mixing in a tank for example is a closed system [101] while a wavy microchannel is a continuous/open system [102]. Poincaré maps for a closed system can be created by crossing a plane and the pathline of a certain particle. On the other hand, since the pathline will eventually go out of the outlet for open systems, the creation of a Poincaré map, which is the result of intersecting the pathline of a single particle and a plane, provides no information. To overcome this, some studies consider the pathline of a bunch of particles which are released along a line or an area near the

inlet and then positioning them along interval planes [23, 102]. Although this is a weak representation of Poincaré section, it is helpful for studying mixing. In Chapters 5 and 6 this method will be used to generate the related Poincaré maps. Figure 3-10 shows how Poincaré maps are generated for a full domain simulation which is used to study the developing flow in converging-diverging microchannels. A certain number of tracers are released along the middle plane of the first furrow and afterwards positions of those tracers are calculated at the intersections along the channel. In Chapter 5 and 6 these Poincaré maps will be used to explain the thermal performance of the wavy walled microchannels.

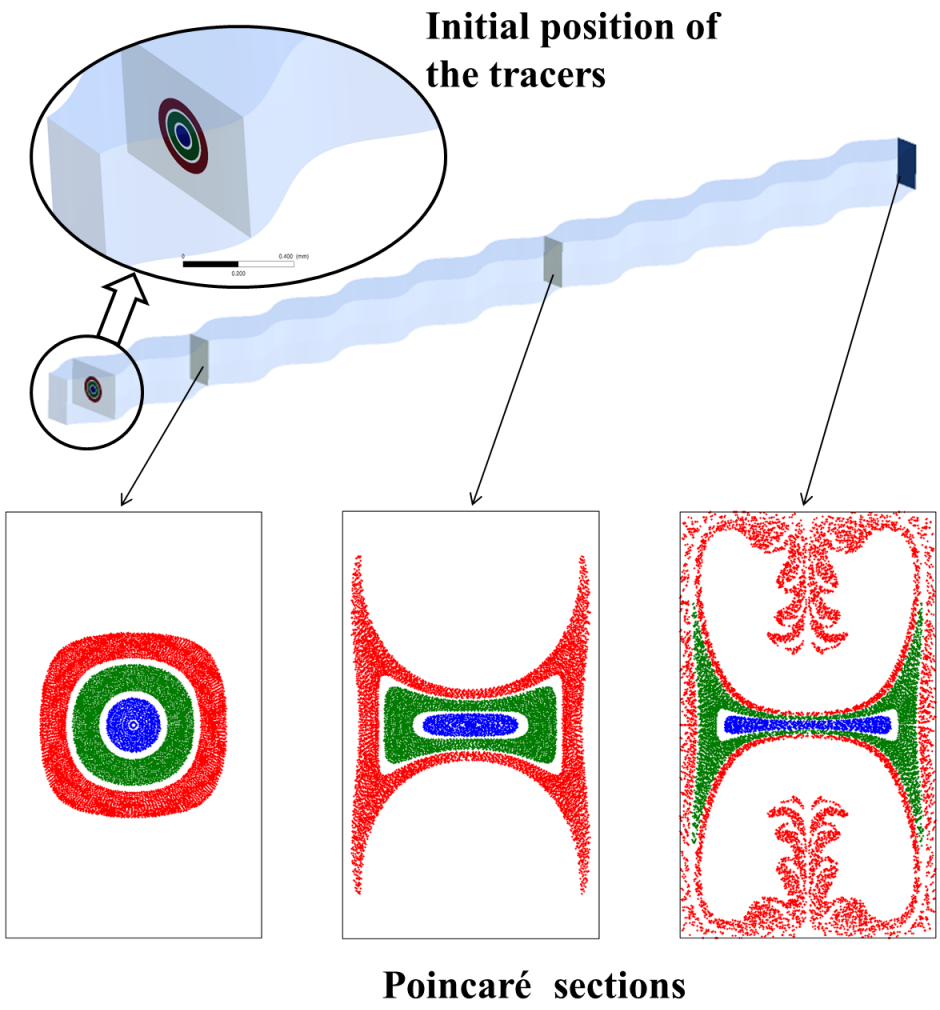

Figure 3-10. Poincaré maps for developing flow condition.

3.4.5.2. Fully developed flow

In order to study the fully developed condition in the wavy walled microchannels, a single furrow with periodic boundary condition at inlet and outlet is considered, section 3.2. Although the wavy walled microchannel is an open (in-out) system, spatial periodicity and the period boundary condition allows us to treat it as a closed system and thus Poincaré maps can be created in a similar fashion that is created for dynamical systems. Figure 3-11 shows a typical Poincaré map for a periodic single furrow condition.

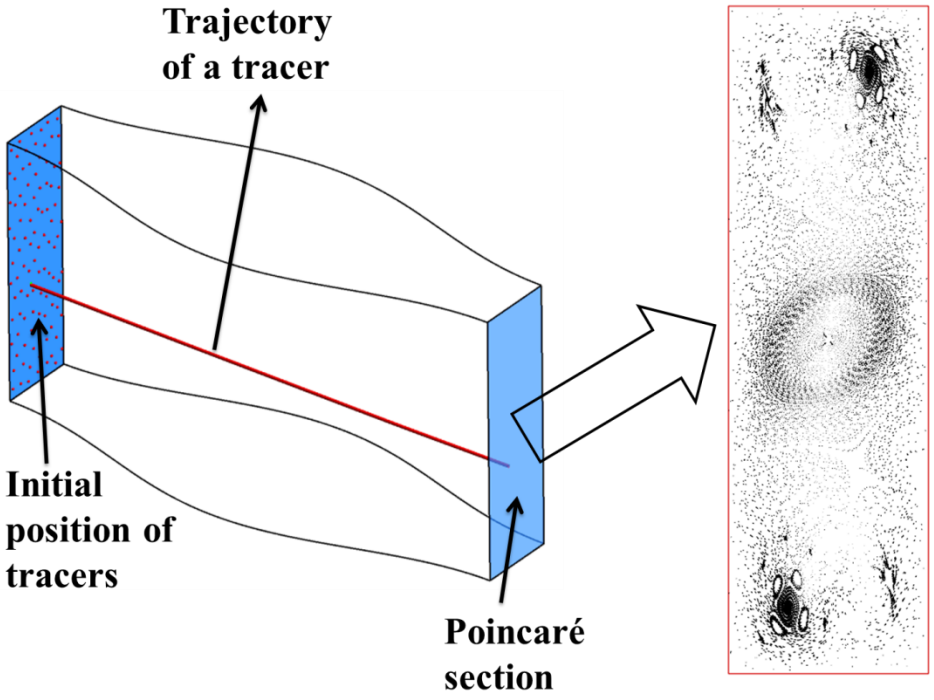

Figure 3-11. A typical Poincaré map for fully developed condition.

In order to create a Poincaré map for the fully developed condition, 100 particles are positioned equidistantly in the plane of the inlet and the trajectory of each particle is calculated based on the ODEs presented in Equation 3-13. The Poincaré map is then generated by recording every intersection of a trajectory and the outlet plane. Subsequently, the particle is again introduced at the inlet corresponding to the same intersection position with the outlet plane and the trajectory is again calculated. This process is repeated for 10,000 times and all the calculated intersections are presented in the format of a Poincaré map. This method was previously used by Khakhar et al. dealing with the problem of mixing in partitioned-pipe mixers [103]. In Chapter 4, Poincaré maps generated in this way will be used to explain the fully developed thermal performance of the wavy walled microchannels.

3.4.5.3. Pulsatile flow

Pulsatile flow in wavy walled microchannels is studied by assuming a 2D model. Aref [57] proves that advection for a steady 2D system is always regular however, by making the flow field time dependent, it may show chaotic behavior. In order to generate the Poincaré map, Aref released a certain number of tracers along a rectangular area and then calculated their position after some time intervals. A regular advection regime is represented by particles positioned along the streamlines while for a chaotic advection regime, tracers were stochastically distributed and they tend to cover the whole domain. Figure 3-12 shows the Poincaré maps related to stirring in a tank, the study done by Aref [57].

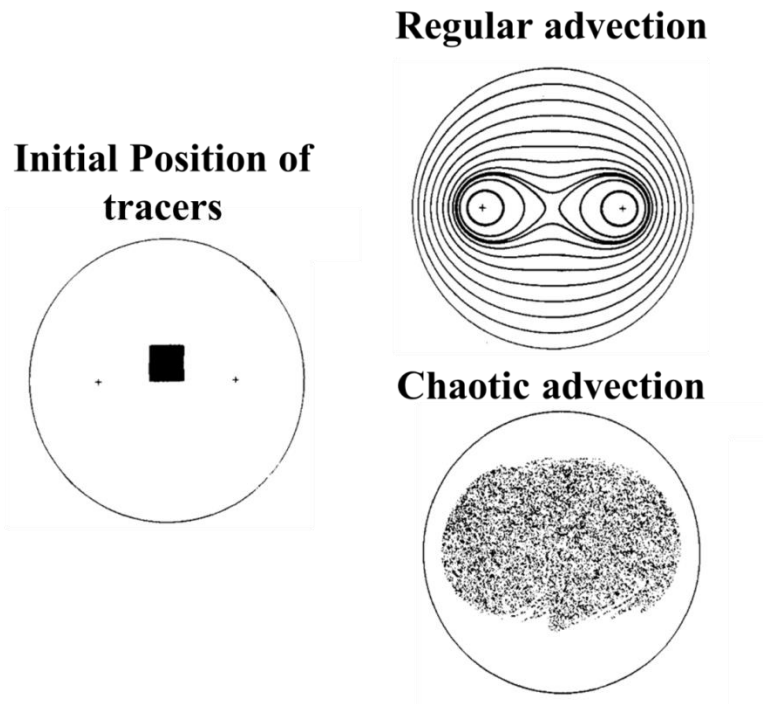

Figure 3-12. Poincaré maps for the problem of stirring in a tank for two advection regimes, regular and chaotic [57].

Poincaré maps for pulsatile flow study in this thesis are generated in a similar fashion. Somewhere near the inlet, 4000 tracers are released along a rectangular area and the

pathline of the tracers are calculated using a fourth order Runge-Kutta method and by considering the time variant velocity field. Figure 3-13 shows the Poincaré map for two cases, regular advection regime and chaotic advection regime. For regular advection regime, particles will travel along the streamline while for chaotic advection regime, particles tend to cover the domain and are positioned stochastically. In Chapter 7 the Poincaré maps created in this way will be used to explain the thermal behavior of the channels.

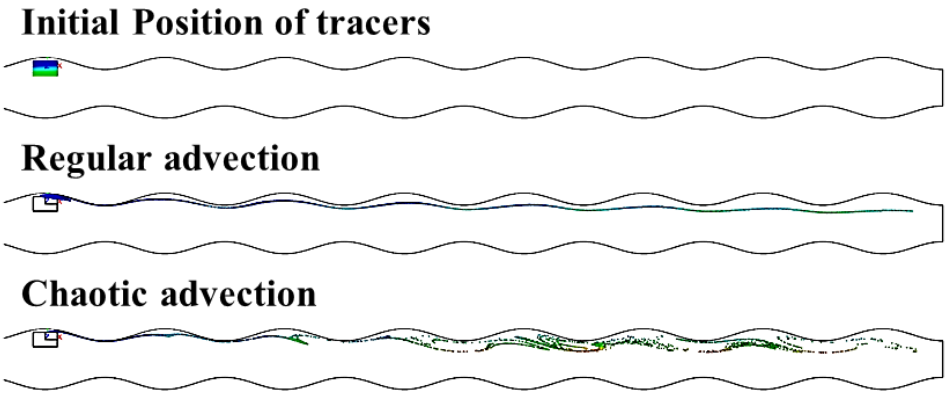

Figure 3-13. Typical Poincaré maps for pulsatile flow in converging-diverging microchannels.

3.5. Vortical structures

By means of analyzing the velocity field, there are several computational techniques to identify a vortex core as a spatial region such as: Eigen Helicity, Real Eigen Helicity, Lambda 2 criterion, Q criterion, Swirling Strength, Vorticity, etc. A thorough review of these methods and their mathematical formulation have been documented in Alfonsi's paper [104]. These methods are mostly used to detect coherent structures in turbulent flows. Nevertheless they can also be used in our case to show the strength of the vortices.

In our study, swirling strength is used to show the vortical structures. Swirling strength represents the imaginary part of complex eigenvalues of velocity gradient tensor and its

value represents the strength of swirling motion around local centers. Iso-surfaces of swirling strength are used to indicate the vortical structures, Figure 3-14.

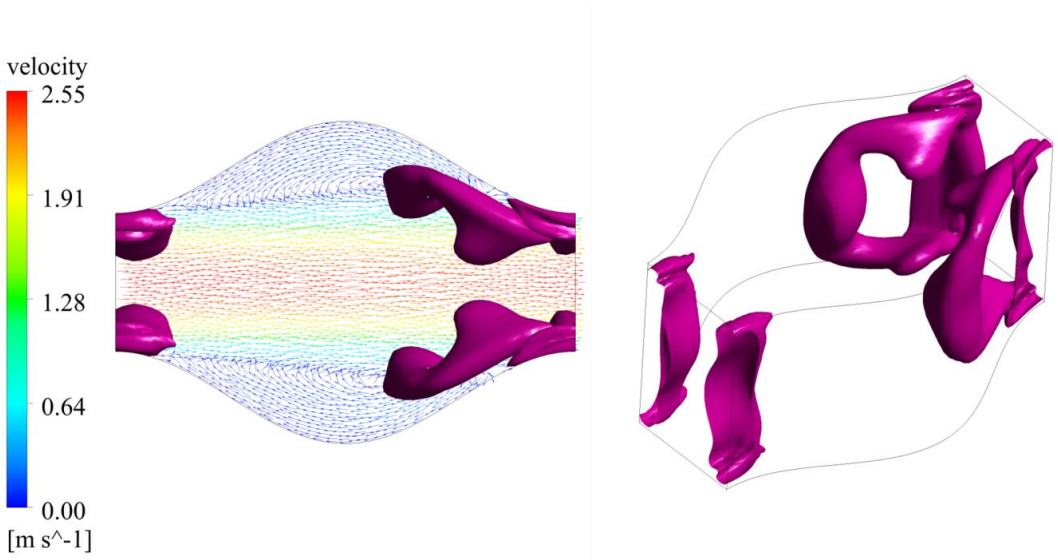

Figure 3-14. A typical vortical structure shown by iso-surfaces of swirling strength. Vector plot shows the presence of a vortex near the region which is indicated by the isosurface.

Chapter 4. Fully developed flow in wavy walled microchannels

4.1. Introduction

In this chapter, the thermal performance of fully developed flow in wavy walled microchannels is investigated by explaining the observed trend using the fluid field, vortical structures in the microchannel and looking into the problem from dynamical systems point of view. Effect of geometrical parameters like channel aspect ratio *S*, wall waviness λ, and channel expansion factor γ are analyzed through extensive transient numerical simulations in order to provide a complete understanding of the physical phenomena. Nusselt number and friction factor graphs are presented as functions of wall waviness and channel aspect ratio and the trends observed are explained by examining the fluid field and Poincaré maps of each microchannel. Comparing the result of modulated channels and the equivalent straight microchannel revealed that there are enhancements up to seven times for the Nusselt numbers albeit with appreciable pressure drop penalty. The performance factor devised to capture the heat transfer augmentation and pressure drop penalty at the same time showed that slightly modulated channels perform better and can achieve enhancements up to 150%.

4.2. Geometry and cases simulated

In Chapter 3, the physical configuration of the converging-diverging microchannel heat sink considered in this thesis was discussed. Figure 3-1 shows a typical configuration of microchannel heat sink with wavy walled microchannels. In order to study the fully developed hydro-thermal performance of the microchannel, it is common to consider a single furrow as the computational domain with periodic boundaries imposed at inlet and outlet [65, 66, 105]. Figure 3-3 shows a typical computational domain for studying the fully developed flow in converging-diverging microchannels.

The current study concentrates on the geometrical parameters' effect on the hydro-thermal performance of the converging-diverging design by studying the fluid flow structures and looking into the problem from dynamical systems point of view. In order to determine the performance of wavy walled microchannels, the equivalent straight microchannel with which comparisons will be done is defined to be the case with $\lambda = 0$ and the same aspect ratio *S*. In order to systematically study the effect of waviness, five aspect ratios are considered, $S = 0.5, 0.8, 1, 1.5$ and 2, and for each aspect ratio waviness is applied to the wall in the way that the average width of the channel *a* remains constant and wall amplitude *A* of the channel changes. All the cases tested are tabulated in Table 4-1. Sections 3.1 and 3.2 present the physical configuration and the computational domains.

Table 4-1. Non-dimensional geometrical parameters of the cases simulated.

$S = 0.5$	$S = 0.8$	$S = 1$	$S = 1.5$	$S = 2$
λ=0, γ=1	λ=0, γ=1	λ=0, γ=1	λ=0, γ=1	λ=0, γ=1
λ=0.05, γ=2.33	λ=0.05, γ=1.67	λ=0.05, γ=1.5	λ=0.05, γ=1.31	λ=0.05, γ=1.22
λ=0.075, γ=4	λ=0.1, γ=3	λ=0.1, γ=2.33	λ=0.1, γ=1.73	λ=0.1, γ=1.5
	λ=0.15, γ=7	λ=0.15, γ=4	λ=0.15, γ=2.33	λ=0.15, γ=1.86
			λ=0.2, γ=3.29	λ=0.2, γ=2.33
				λ=0.25, γ=3

4.3. Mathematical formulation and numerical procedure

Fluid flow in the converging-diverging microchannel is assumed to be incompressible and Newtonian with constant properties, Table 4-2. Neglecting the viscous dissipation, conservation of mass, momentum and energy for the fluid domain would be the ones that are presented previously in Section 3-3 by Equations 3-3 to 3-5. The computational

domain is a single furrow of the corrugated channel under periodic boundary condition, Section 3-2. This is a routine boundary condition available in FLUENT which is used when the geometry as well as the anticipated flow pattern have spatial periodicity. Periodic boundary condition implies that the components of the velocity repeat in space:

$$\mathbf{V}(\vec{r}) = \mathbf{V}(\vec{r} + \vec{L}) = \mathbf{V}(\vec{r} + 2\vec{L}) = \ldots \tag{4-1}$$

where $\vec{r}$ is the position vector and $\vec{L}$ is the periodic length vector which in our case is equal to the wavelength of the wavy wall. Pressure drop also has a periodic nature as:

$$\Delta p = p(\vec{r}) - p(\vec{r} + \vec{L}) = p(\vec{r} + \vec{L}) - p(\vec{r} + 2\vec{L}) = \ldots \tag{4-2}$$

Pressure field however can be decomposed into two parts as:

$$p(\vec{r}) = \tilde{p}(\vec{r}) + \beta x \tag{4-3}$$

where β is the applied pressure gradient that drives the flow in x direction and $\tilde{p}(\vec{r})$ is the periodic pressure field.

Table 4-2. Thermo-physical properties of water.

Density ρ ($kg\ m^{-3}$)	**998**
Thermal conductivity k ($W\ m^{-1}\ K^{-1}$)	**0.6**
Specific heat capacity C_p ($J\ kg^{-1}\ K^{-1}$)	**4182**
Dynamic viscosity μ (Pa s)	**0.001003**

It is obvious that the temperature field may not be periodic. However, it is possible to define a scaled temperature for which spatial periodicity may be applied. This scaled temperature can be defined for constant temperature or constant heat flux boundary

conditions, the scaled temperature $\theta(\vec{r})$ for constant temperature boundary condition would be:

$$\theta(\vec{r}) = \frac{T(\vec{r}) - T_{wall}}{T_{m,inlet} - T_{wall}} \tag{4-4}$$

where the mass-weighted average temperature T_m is determined by:

$$T_m = \frac{\int_A T \left| \rho \mathbf{V} \bullet \overrightarrow{dA} \right|}{\int_A \left| \rho \mathbf{V} \bullet \overrightarrow{dA} \right|} \tag{4-5}$$

And with the above definition, periodicity in the scaled temperature field requires that:

$$\theta(\vec{r}) = \theta(\vec{r} + \vec{L}) = \theta(\vec{r} + 2\vec{L}) = \ldots \tag{4-6}$$

As mentioned, walls are kept at constant temperature and the dimensionless temperatures at the inlet and outlet are set to be periodic. The driving force for the fluid is the parameter β which has a direct effect on the mass flow rate through the channel.

Heat transfer performance of the microchannel is characterized by considering the fully developed Nusselt number as

$$Nu = \frac{hD_h}{k} \tag{4-7}$$

where D_h is the hydraulic diameter and is defined based on the equivalent straight microchannel, Eq. 3-1. For the constant wall temperature boundary condition, heat transfer coefficient h is given by:

$$h = \frac{Q}{A_{HT}} \cdot \frac{ln\left(\frac{T_w - T_{m,inlet}}{T_w - T_{m,outlet}}\right)}{\left(T_w - T_{m,inlet}\right) - \left(T_w - T_{m,outlet}\right)} \tag{4-8}$$

where A_{HT} is the heat transfer area and Q is the amount of heat transferred to the coolant and is determined by integrating the heat flux over the heat transfer area:

$$Q = \int_{A_{HT}} q'' dA \tag{4-9}$$

The definition for mass-weighted average temperatures, T_m, has previously been presented in Equation 4-5.

Pressure drop is quantified by the product *fRe* where *f* is the Fanning friction factor which is a quarter of the Darcy friction factor. Darcy friction factor is determined from:

$$f_D = -\beta \times \frac{2D_h}{\rho U_m^{\ 2}} \tag{4-10}$$

where β is the periodic pressure gradient and $U_m = \dot{m}/A_{cr}$ is the mean velocity for the equivalent straight microchannel. $A_{cr} = a \times b$ is the cross sectional area of the equivalent straight microchannel and $\dot{m}$ is the mass flow rate through the microchannel.

The above equations are used to determine the instantaneous values of *Nu* and *f* which are subsequently time-averaged after system reaches a steady state.

Gambit is used to generate the mesh based on a mapped scheme which uses structural grids. Mesh independence study is performed for each set of geometries so that the results are mesh size independent. For instance, a typical mesh size for a case involving *S* = 2 is $50 \times 60 \times 60$. Table 4-3 shows a typical mesh study performed, the medium mesh size is chosen.

Table 4-3. A typical mesh independence study.

S = 0.8	**Re=200**	**λ=0.05**		
	Nu	*fRe*	*%Nu*	*%fRe*
3*40*40	7.9	19.9		
50*60*60	7.61	19.87	-3.67089	-0.15075
70*80*80	7.52	19.86	-1.18265	-0.05033

Shah and London [106] has provided two empirical equations to calculate the values of *fRe* and *Nu* for straight ducts with aspect ratio of *S* as:

$$fRe = 24*(1-1.3553\times S+1.9467\times S^2-1.7012\times S^3+0.9564\times S^4-0.2537\times S^5) \quad (4\text{-}11)$$

$$Nu = 7.541\times(1-2.61\times S+4.97\times S^2-5.119\times S^3+2.702\times S^4-0.548\times S^5) \quad (4\text{-}12)$$

Using above models, the numerical results of fully developed flow for the straight microchannel configuration showed differences of less than 0.5% for *Nu* and *fRe*, Table 4-4.

Using a finite volume approach, FLUENT 14.5, second order spatial discretization is used to solve the conservation equations along with the prescribed boundary conditions. A SIMPLE scheme is also used to couple the velocity and pressure fields. All the cases are solved with a second order transient scheme to capture any transition to Eulerian chaos and as it will be presented later, there are some cases with transition for *Re* = 400 and 600 with highly modulated walls. Time step was a function of geometry and *Re* and it was between 1e-4 to 1e-5 which resulted to Courant numbers less than 10. A MATLAB code was subsequently written to calculate the values of *Nu* and *f* at each time step and to report the average values of these parameters at the end of the simulations.

Table 4-4. The comparison between the analytical and numerical values of *Nu* and *fRe* for the straight microchannel with *S* = 1.

***S* = 1**	**Analytical**		**Numerical**	
	Nu	*fRe*	*Nu*	*fRe*
	2.9787	14.2296	2.9827	14.187
Difference			0.13%	-0.3%

4.4. Results and discussion

4.4.1. Vortical structures

In order to explain the results for heat transfer and pressure drop of wavy walled microchannels, it is important to understand the fluid field. Vortical structures being formed in the microchannel play a critical role in heat transfer performance as they can enhance heat transfer if they contribute to mixing or can have an adverse effect if they create stagnant regions.

In order to show the vortical structures, iso-surfaces of swirling strength are considered. The volume encapsulated by the iso-surface has larger swirling strength than the corresponding iso-surface. Figure 4-1 shows a typical vortical structure being formed in a converging-diverging configuration and its evolution as a consequence of *Re* increment and wall waviness λ increment. From Figure 4-1 it is seen that there are two types of vortical structures:

- Four streamwise vortices which are formed in the corners of the channel in the contracting part of the furrow
- Two counter rotating vortices which are formed in the trough region of the furrow

By introducing a slight curvature to the wall of the microchannel, four streamwise vortices will be formed in the corners of the channel while for larger values of wall waviness, two counter rotating vortices will be created in the trough region. Similar trends may be observed when the geometry is kept constant and *Re* is increased. The effects of these vortical structures on heat transfer and pressure drop will be discussed in detail in Section 4.4.3.

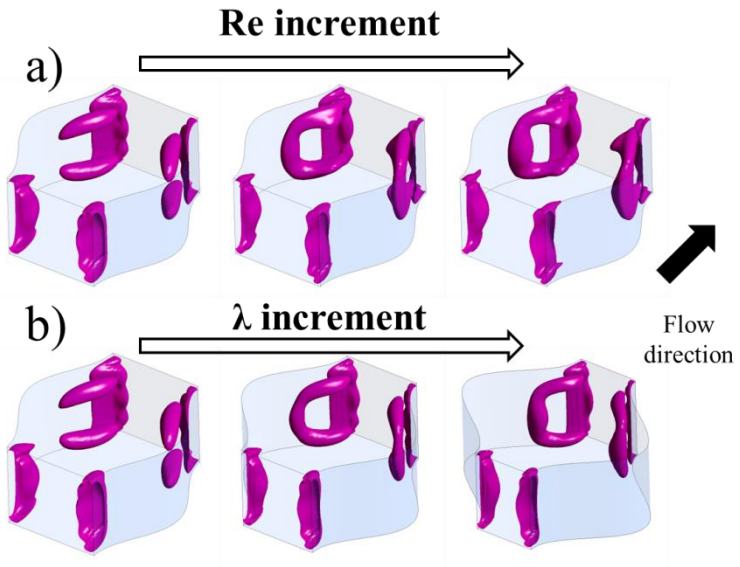

Figure 4-1. Vortical structure evolution as the result of increment in (a) *Re* and (b) wall waviness λ.

4.4.2. Dynamical system point of view

Section 3.4.5 provided an overview of the flow field as a dynamical system. The definition of Poincaré section and also chaotic advection were presented and the method to create the Poincaré section in fully developed condition was discussed. Figure 4-2 shows the Poincaré sections of the cases with aspect ratio of $S = 1$ for varying degrees of wall curvature and *Re* as wall waviness increases from left to right and *Re* increases from top to bottom. The case with $\lambda = 0$ corresponds to the straight microchannel and as it can be seen, the particles along the outlet are positioned at the locations where they have been

released along the inlet. Thus it can be concluded that advection in a straight microchannel is regular. However, introducing slight waviness to the walls, it is observed that wall curvature induces chaotic advection in the system and there appears to be 4 laminar regions residing at the corners of the map which are the KAM curves [107]. If the Poincaré sections are plotted at intermediate lengths, it is possible to see the evolution of these KAM curves. In fact each KAM curve represents the intersection of a tube with the Poincaré section. These tubes are invariant surfaces which cannot be crossed by fluid particles. Consequently, a fluid particle which is trapped in the tube will not mix with other parts of the fluid field. Figure 4-3 shows a schematic diagram of the KAM tubes. As it can be seen, the KAM curves occupy a small area of the Poincaré map and the rest of the map has remains chaotic.

Symmetry in the Poincaré map reveals that there are just four mixing regions and particles from each region will not mix with other regions. For cases with larger *Re* and λ, symmetry of the Poincaré map breaks down and six or eight KAM curves will appear in the map. When asymmetry arises in the Poincaré map, an increase in thermal performance is observed which can be related to stronger chaotic advection. Figure 4-3 shows the typical KAM tubes for the cases with symmetric KAM tubes which resembles a weak chaotic advection regime and the asymmetric KAM tubes which are associated with strong chaotic advection. Later the relationship between the Poincaré section and the thermal performance of the microchannels will be discussed in detail.

4.4.3. Hydro-Thermal performance of the microchannel

As it was discussed in Section 3.1, wall waviness λ and channel expansion factor γ are both needed to define the wavy walled channels. For example cases with the same waviness λ but different aspect ratio *S* will have a different expansion factor γ. In order to show *Nu* and *fRe* as the functions of waviness, a 3D graph similar to Figure 4-4 and 4-5

for *Nu* and *fRe* respectively can be used. However for better representation of the data, a 2D graph which considers the waviness will be used to present the results.

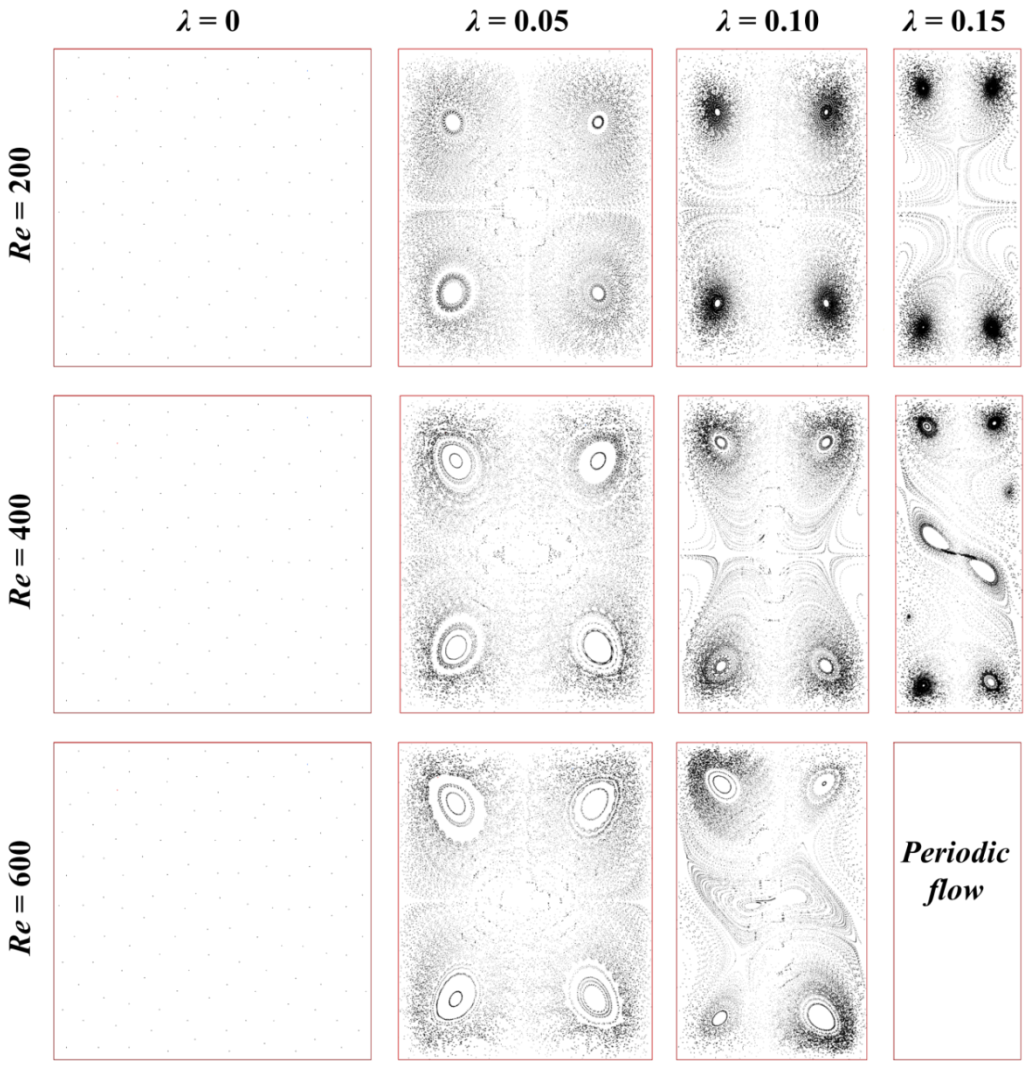

Figure 4-2. Poincaré maps for the case with S = 1 and λ = 0, 0.05, 0.1 and 0.15 at Re = 200, 400 and 600.

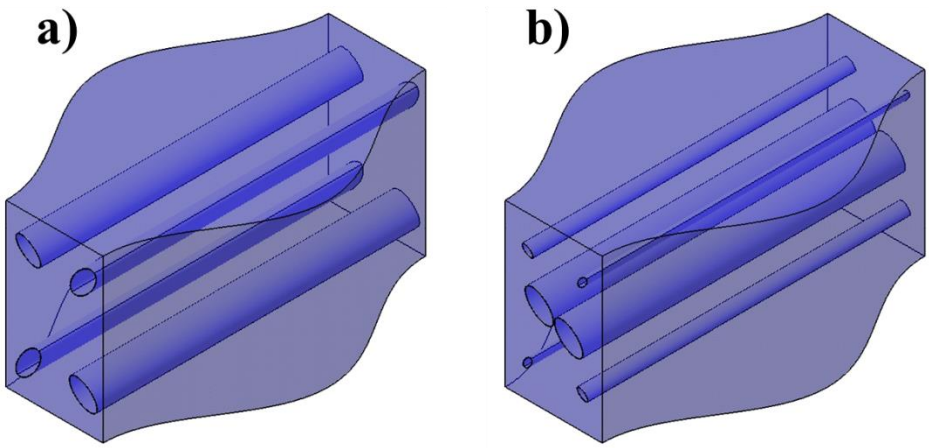

Figure 4-3. Typical KAM tubes for the cases with a) symmetric KAM tubes b) asymmetric KAM tubes.

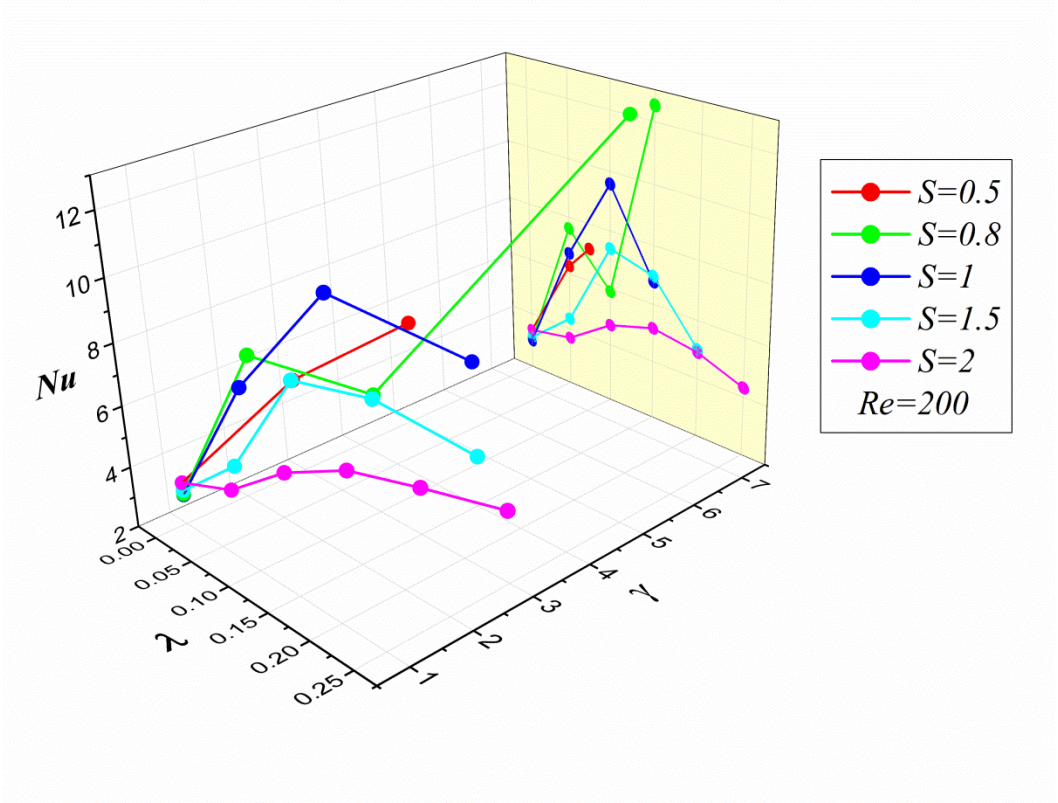

Figure 4-4. *Nu* as a function of waviness λ and channel expansion factor γ.

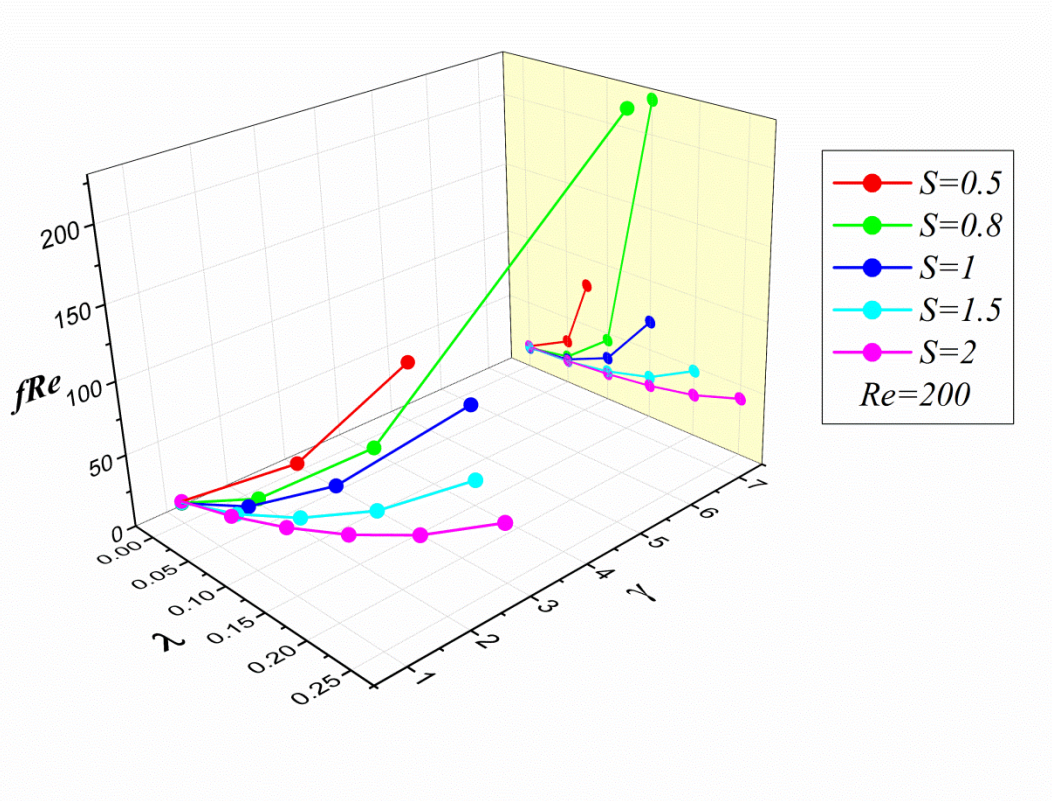

Figure 4-5. *fRe* as a function of waviness λ and channel expansion factor γ.

Figures 4-6 to 4-8 show the Nusselt number as a function of wall waviness λ and aspect ratio S for Re = 200, 400 and 600. As depicted in Figures 4-6 to 8, there is a trend regarding the thermal performance of converging-diverging microchannels. It seems that the heat transfer performance increases at λ = 0.05 for all the cases. However, further increase in wall waviness results in a decrease in Nu. This can be explained by investigating the shape of the vortical structures in the microchannels as well as the Poincaré sections. The error bars in the graphs are due to the fact that some cases shows time dependent behavior with Nu and friction factor being a function of time and hence having maximum and minimum.

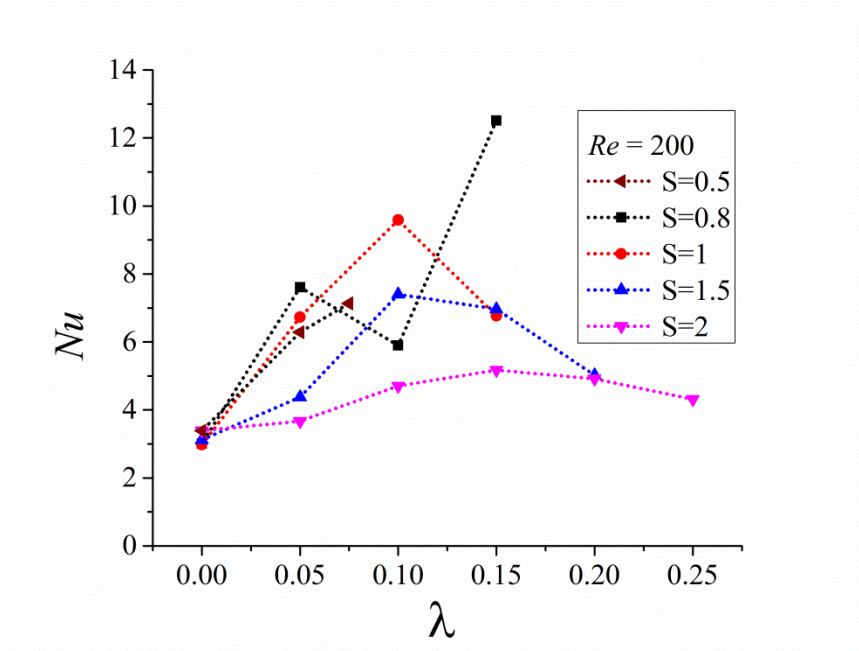

Figure 4-6. *Nu* as a function of wall waviness and aspect ratio for *Re* = 200.

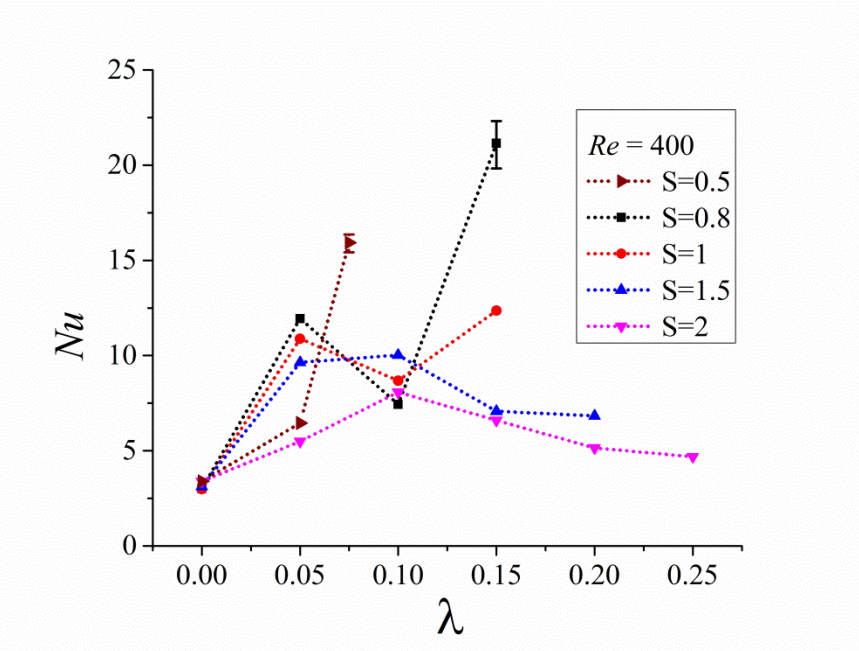

Figure 4-7. *Nu* as a function of wall waviness and aspect ratio for *Re* = 400.

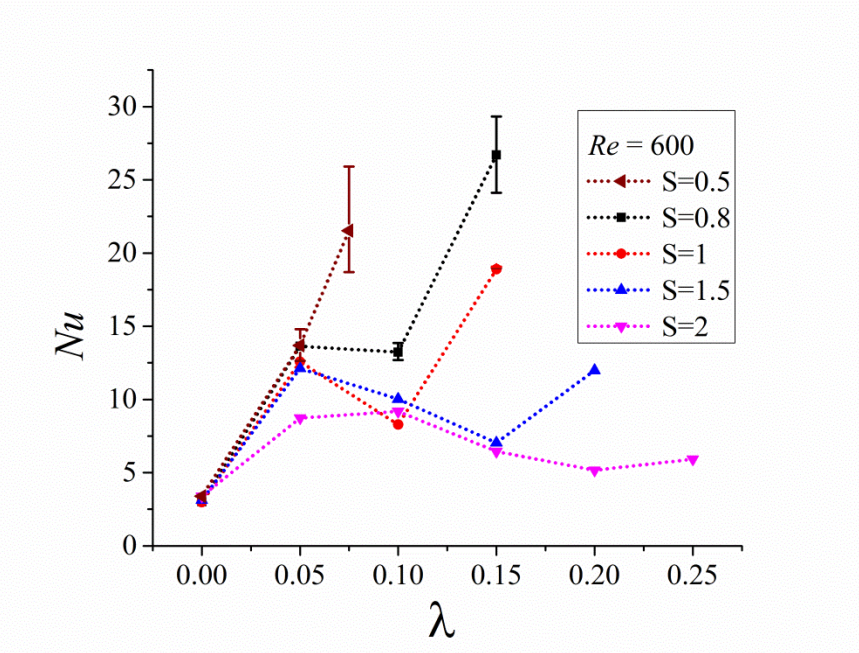

Figure 4-8. *Nu* as a function of wall waviness and aspect ratio for *Re* = 600.

Just for the sake of explaining the behavior and without loss of generality, consider the case with aspect ratio S = 1.5 which corresponds to the blue line in Figures 4-6 to 8. It is seen that by increasing the wall waviness, there is initially an increase in *Nu* and after *Nu* reaches a peak, it starts to decline when the wall waviness is further increased. However, there appears to be a second increment if *Re* and channel expansion factor are sufficiently large, such as the case with S = 1.5 and λ = 0.2 at *Re* = 600. Such a trend is also observed for the case with S = 0.8 at *Re* = 200, 400 and 600. However, for the cases with smaller aspect ratio like S = 0.5, there appears to be no decline in *Nu* as wall waviness λ increases.

As it will be covered with more details in the next chapter on the developing flow in converging-diverging microchannels, Section 5.4.1, there are three mechanisms that affect the heat transfer in such a configuration. These mechanisms are increase in heat transfer area due to channel wall modulation, decrease in heat transfer due to stagnant

volumes of fluid in the trough region of the channel and the presence of strong chaotic advection regime which enhances heat transfer.

The first increase in the *Nu* is due to increase in heat transfer area of the side walls and also the presence of chaotic advection. When wall waviness reaches a certain level, the counter rotating vortices formed in the trough region causes stagnant regions which eventually reduces the effective heat transfer area and hence reduces *Nu*. The second increase in *Nu* is due to the presence of a strong chaotic advection regime. Hence, as compared to the equivalent straight microchannel, small wall waviness increases the heat transfer area and induces chaotic advection. Furthermore, there are no counter rotating vortices in the trough region to decrease the effective heat transfer area. This indeed is confirmed from the *Nu* graphs. As can be seen from Figures 4-6 to 8, for some cases, the increase in *Nu* for λ = 0.05 is more than two to three times compared to the equivalent straight microchannel.

Figure 4-9 shows the vortical structures as well as the scaled temperature θ contour for the cases with S = 1.5 and Re = 200, 400, 600. It is seen that for all the cases with moderate wall curvature, λ = 0.05, four streamwise vortices are created at the corners which help to improve mixing by transporting the flow from the side walls to the center. However, for highly modulated channels, although these streamwise vortices strengthen, counter rotating vortices created in the trough region will create stagnant regions which reduce the effective heat transfer area and eventually reduce *Nu*. For the highest *Re* and λ, it can be seen that *Nu* experiences another increase which means that the effect of streamwise vortices has exceeded the adverse effect of counter rotating vortices.

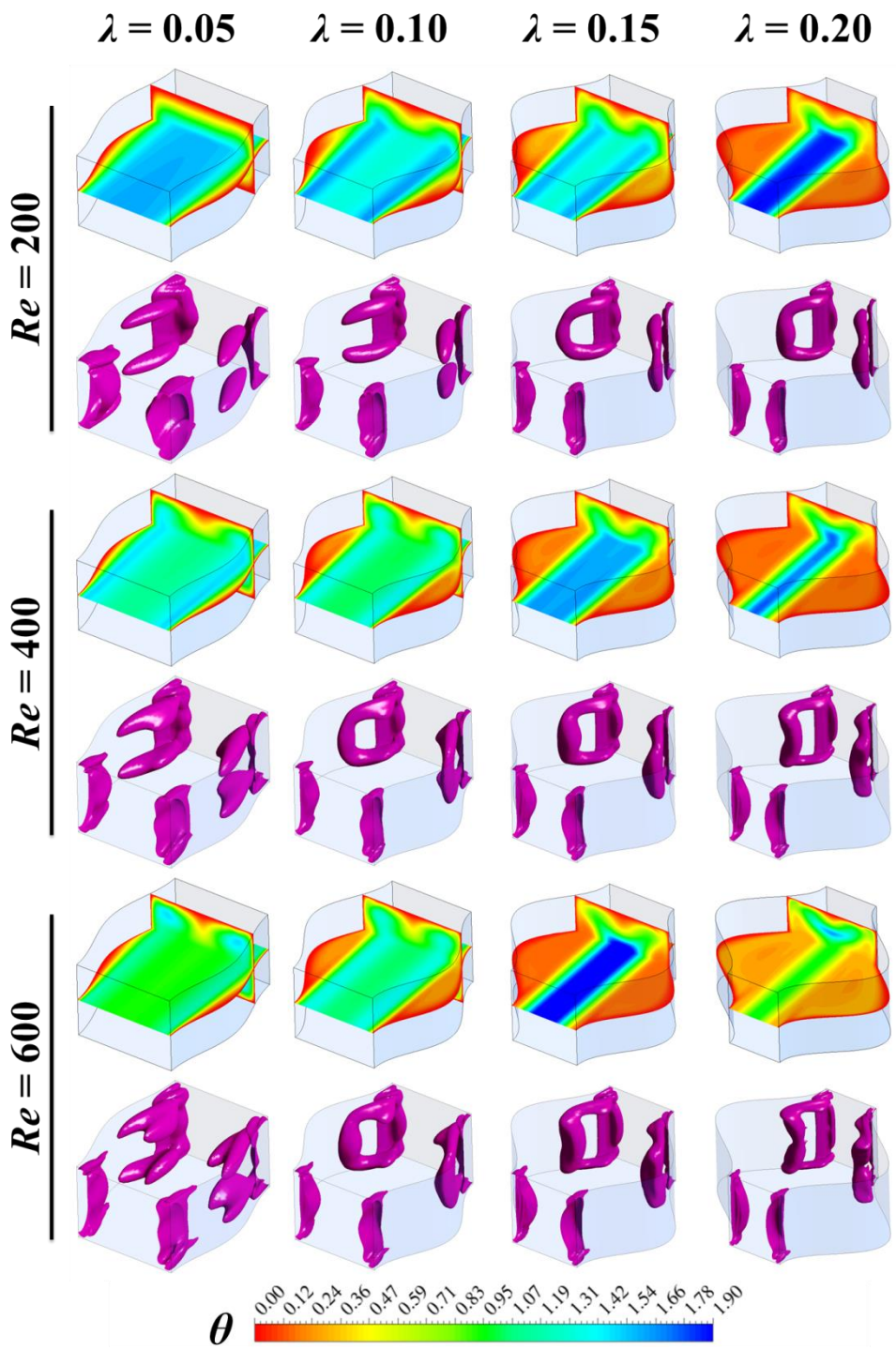

Figure 4-9. Vortical structures and temperature contours for the case with S = 1.5 at four levels of wall waviness and three Re.

Poincaré maps can also help in the understanding associated with the second increase in *Nu*. For example, considering the cases with S = 1 corresponding to the red line in Figures 4-6 to 8, it is observed that at *Re* = 200 there is no second increment while for higher *Re* of 400 and 600, there appears to be a second increase in *Nu*. Considering the Poincaré maps provided for these cases in Figure 4-2, it is observed that symmetry in Poincaré maps breaks down for the case involving *Re* = 400. The case involving *Re* = 600 and λ = 0.15 exhibits transient behavior, which means that the Eulerian flow field has altered from steady to periodic and hence there is a strong chaotic advection regime.

Comparing the values of *Nu* at different *Re* for λ = 0.05, it is seen that a smaller aspect ratio (narrower channel) does not necessarily imply a larger *Nu*. For example, at *Re* = 200, S = 0.8 and 1 display superior heat transfer performance than S = 0.5 at λ = 0.05, whereas at *Re* = 400, the case with S = 1.5 is also performing better than S = 0.5. This shows that there should be an optimal configuration considering *Re* and geometry which yields the best thermal performance.

Figures 4-10 to 12 represents the *fRe* product as a function of wall waviness and aspect ratio for *Re* = 200, 400 and 600. The graphs depicted in Figures 4-10 to 12 reveal that by increasing the wall waviness, pressure drop always increases. Also, for constant wall waviness, cases with smaller aspect ratio S will show higher pressure drop penalties. The cases with strong chaotic advection regimes, S = 0.8 and λ = 0.15 at *Re* = 200 for example, show a noticeable increments in pressure drop. Those cases are the ones that will soon show transition to time dependent behaviors as *Re* or wall waviness λ increases with the values of *Nu* and *fRe* varying between a maximum and minimum which are shown by variation bars in the related Figures.

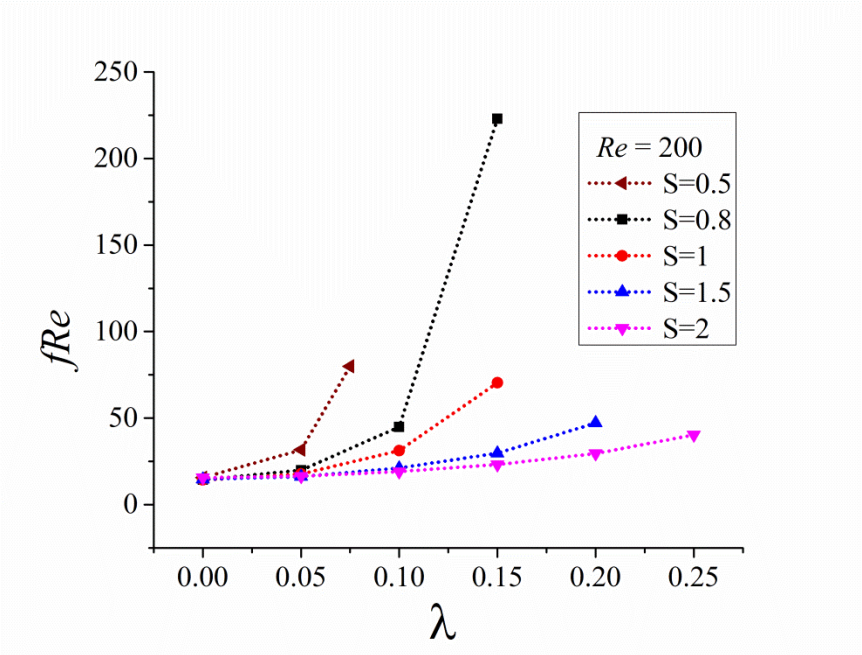

Figure 4-10. *fRe* as a function of wall waviness for *Re* = 200.

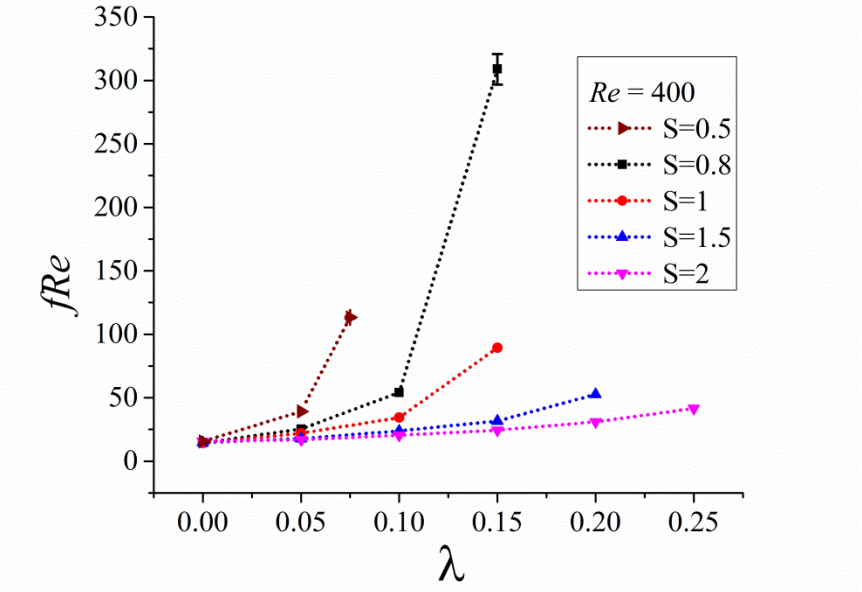

Figure 4-11. *fRe* as a function of wall waviness for *Re* = 400.

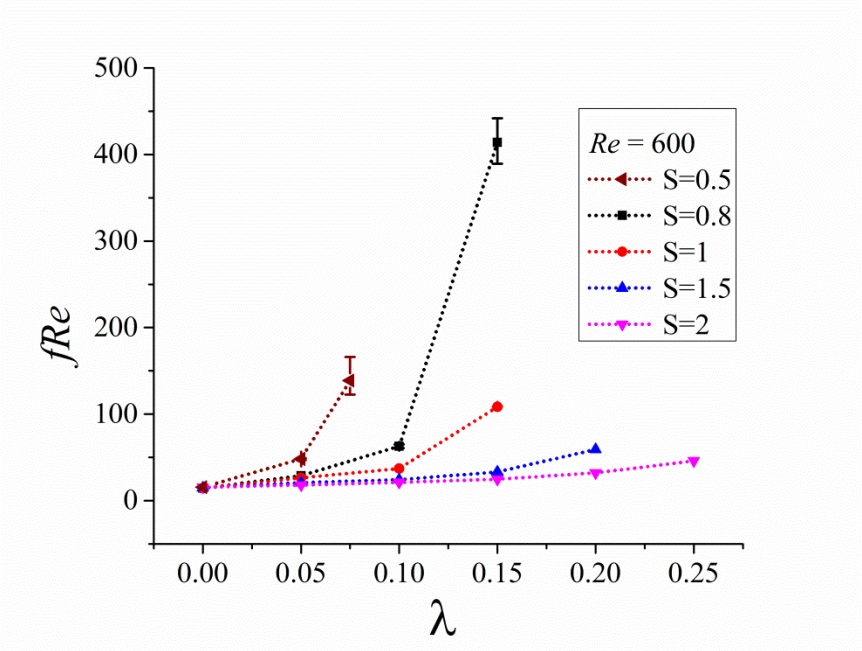

Figure 4-12. *fRe* as a function of wall waviness for *Re* = 600.

It should be noted that the channel expansion factor γ is the counterpart to wall waviness and when *fRe* is plotted against γ, it seems that the friction factor can be expressed in terms of a simple exponential function of γ. It is believed that the narrowest part of the channel has the maximum influence on the pressure drop. Hence, using the expression derived for fully developed flow in ducts, *fRe* for a duct with aspect ratio of $S' = (a - 2A)/b$ is given by [106]

$$fRe_{S'} = \frac{24}{\left(1+\frac{1}{S'}\right)^2\left(1-\frac{192}{\pi^5 S'}\sum_{n=1,3,\ldots}^{\infty}\frac{\tanh\left(n\pi S'/2\right)}{n^5}\right)} \tag{4-13}$$

The above equation is represented in a polynomial form by Shah and London [106] which is already provided in Equation 4-11. This can be used to normalize the result for *fRe* and in this way the effect of channel aspect ratio can be accounted for. Figure 4-13 delineates the ratio $fRe/fRe_{S'}$ as function of channel expansion factor and it can be seen

that a simple closed form relation between friction factor and channel expansion factor γ can be written as $fRe/fRe_{S'} = C_1 \exp(C_2\gamma)$ where C_1 and C_2 are constants which are functions of *Re*. For the Reynolds numbers examined in the current study, the closed form relation is calculated and presented in Figure 4-13.

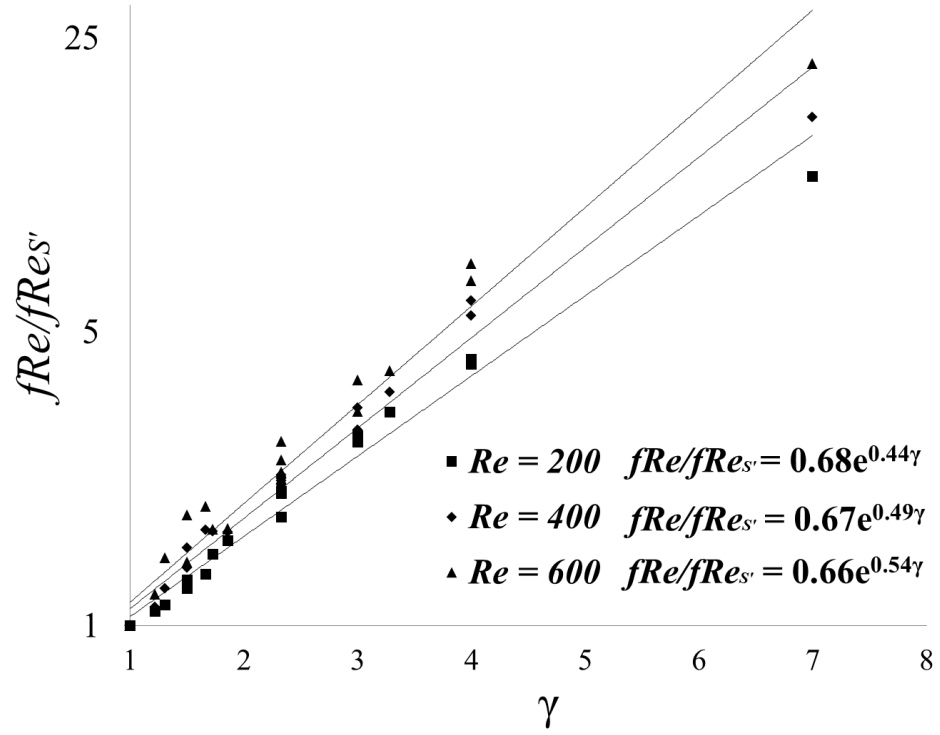

Figure 4-13. Friction factor as a function of channel expansion factor γ.

4.4.4. Transition to chaos

Through the original works done by Guzman and Amon [66-68], it is well established that by increasing the *Re*, converging-diverging microchannels will eventually experience a series of Hopf bifurcations and a scenario similar to the RTN scenario for the onset of chaos is being observed for such systems. *Re* was the control parameter in those studies. However, our results show that a similar trend can be observed even when *Re* is kept constant (which is equivalent to keeping the mass flow rate constant) and when the wall waviness λ is increased. A transition from steady to periodic and finally chaotic flow is

observed in this case. Figure 4-14 displays the transient cases whose values are accompanied by variation bars in Figures 4-6 to 8 and 4-10 to 12.

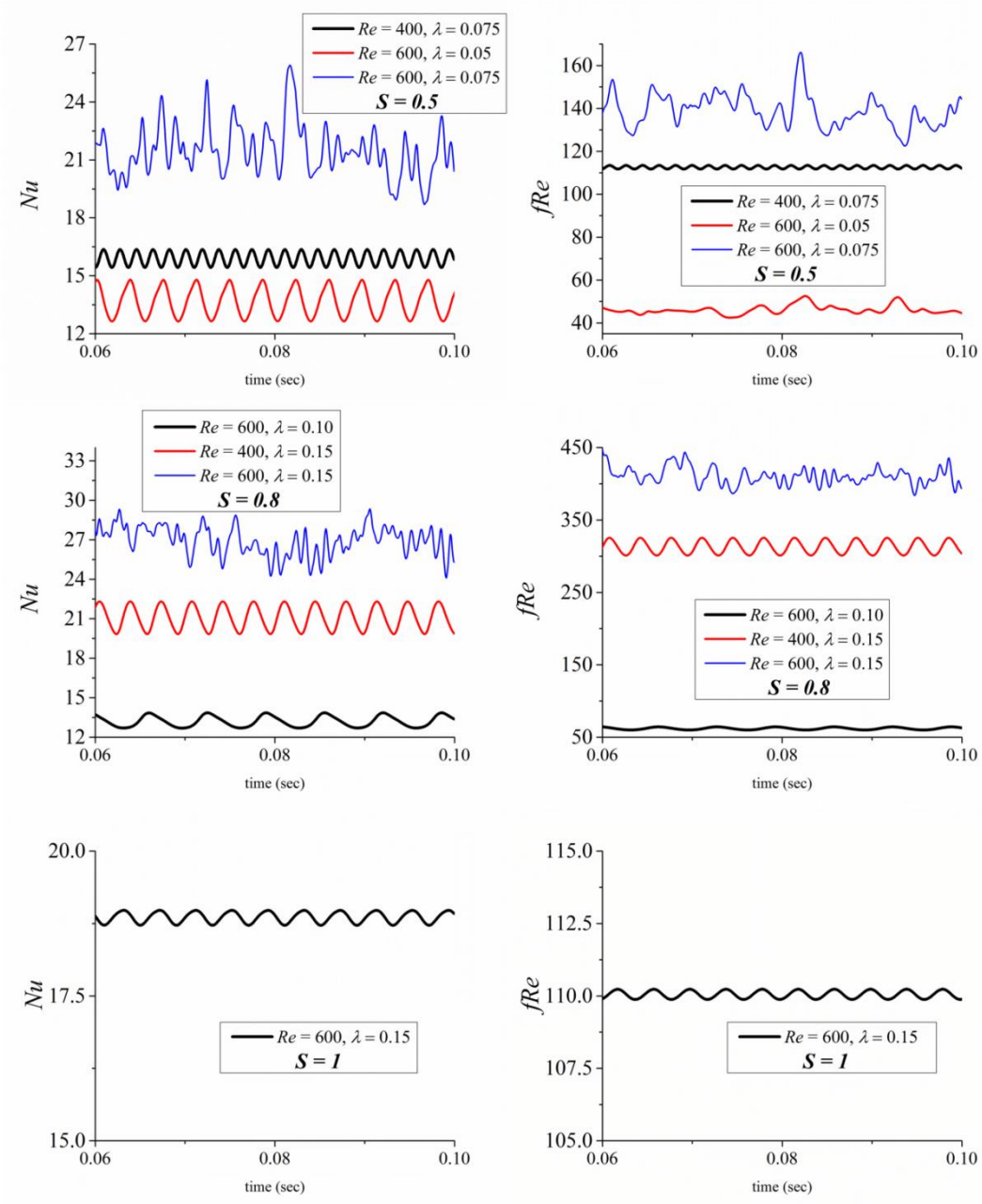

Figure 4-14. Temporal value of *Nu* and *fRe* for the three aspect ratio of *S* = 0.5, 0.8, 1.

Comparing the effects of increasing *Re* and λ, it is seen that increasing the wall waviness has a larger influence on *Nu* and *fRe* as the values are larger for the cases with larger λ

but smaller *Re*. The cases exhibiting transient behavior show a sharp increase in both *Nu* and *fRe*. Thus, there should be a performance factor which simultaneously considers both the heat transfer performance and pressure drop penalty.

4.4.5. Performance factor

It is possible to compare the increase in heat transfer performance and corresponding increase in pressure drop penalty using a single parameter. Consider the increment in heat transfer given by:

$$\eta_{Nu} = \frac{Nu_{wavy}}{Nu_{straight}} \tag{4-14}$$

where $Nu_{straight}$ corresponds to the fully developed Nusselt number for the equivalent straight microchannel. The increment in pressure penalty is given by

$$\eta_f = \frac{fRe_{wavy}}{fRe_{straight}} \tag{4-15}$$

where $fRe_{straight}$ corresponds to the fully developed *fRe* for the equivalent straight microchannel. The performance factor may be defined based on a direct comparison between these two parameters:

$$PF = \frac{\eta_{Nu}}{\eta_f} \tag{4-16}$$

This is a fair comparison as the mass flux and the compactness of the microchannel are the same for the wavy and equivalent straight microchannels. This performance factor was previously used in similar studies [23, 102].

PF is delineated in Figure 4-15 as a function of wall waviness λ and *Re*. It can be seen that for all the cases, moderate wall waviness culminates in a better thermal-hydraulic

performing. At *Re* = 200, the case with aspect ratio of *S* = 0.05 has inferior performance for all values of λ. However, other cases with *S* = 0.8, 1 and 1.5 show improvements up to 80% but mostly for slightly modulated geometries of λ = 0.05 and 0.1. For highly modulated channels, *PF* is always below 1 which indicates that the increment in heat transfer is compromised by a higher pressure drop penalty. Thus, slightly modulated channels lead to more superior designs in terms of thermal-hydraulic performance.

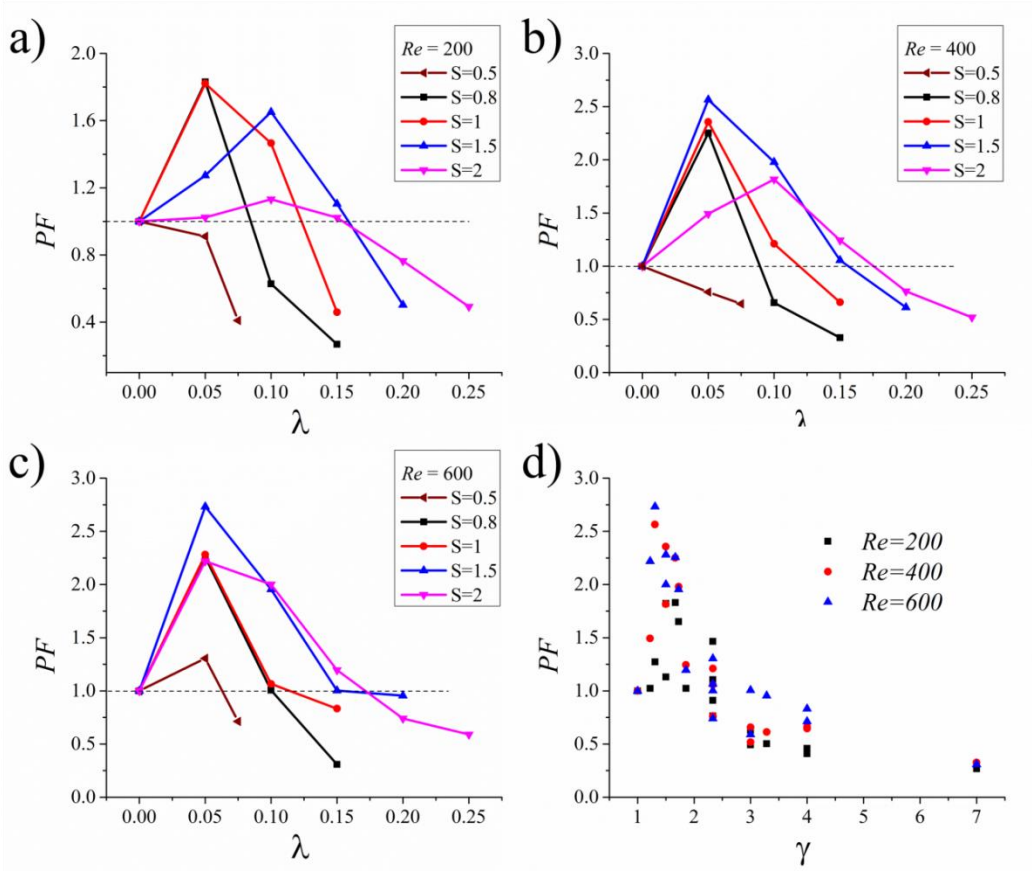

Figure 4-15. *PF* as a function of wall waviness for: (a) *Re* = 200, (b) 400 and (c) 600. (d) *PF* as a function of channel expansion factor, γ.

Another observation is the migration of the peak to smaller values of λ as *Re* increases for cases with larger aspect ratios, *S* = 1.5 and 2. The reason may be due to the strength of the chaotic advection as a consequence of stronger streamwise vortices at larger *Re*. For smaller wall waviness, chaotic advection is not that powerful for cases involving large

aspect ratios. However, when *Re* increases, chaotic advection enhances for smaller wall waviness and eventually results in better performance.

A scattered plot of performance factor *PF* against the expansion factor γ (Figure 4-15d) for all the cases simulated reveals some interesting results. First, there is a strong relation between the expansion factor and the performance factor and second, designs with $\gamma \sim 1.5$ have the highest performance at all the *Re*. These results emphasize the importance of the expansion factor parameter as the key geometrical parameter for converging-diverging configuration.

4.5. Conclusion

In this chapter fully developed flow under constant temperature boundary condition was studied for converging-diverging microchannels. The effect of geometrical parameters on thermal performance and pressure drop penalty were fully investigated by examining the fluid field, vortical structures and looking into the problem from dynamical systems point of view.

A study of the vortical structures showed that by adding wall curvature to the microchannel, four streamwise vortices were created at the corners of the microchannel which have major effect on mixing. These vortices also induced chaotic advection in the system as Poincaré sections suggest. Increasing the wall waviness further, two counter rotating vortices were formed in the trough region of the channel, creating stagnant areas in the domain and reducing the effective heat transfer area and heat transfer eventually. For highly modulated channels and/or high *Re*, the effect of streamwise vortices will exceed the counter rotating vortices and heat transfer increases again. This usually shows itself by asymmetrical Poincaré map of the system.

A typical Poincaré map of converging-diverging microchannel is a stochastic map with four laminar regions at the corners which by considering the 3D model, are the result of intersecting four invariant surfaces in the format of tubes and the Poincaré plane. Increasing the value of wall waviness causes the diameter of these tubes to reduce but it makes them of higher order of periodicity. As long as symmetry in the Poincaré map holds, there are four regions of mixing in the channel around each laminar region but when increasing the wall waviness and/or *Re* further, asymmetry in Poincaré section appears and the degree of asymmetry and increment in heat transfer showed a direct relation.

Transition to Eulerian chaos was observed for cases with highly modulated walls and smaller aspect ratios. Transition from laminar to periodic and then Eulerian chaos was observed as *Re* increased for a specific geometry or when *Re* was kept constant and wall waviness was increased. Although the transition to Eulerian chaos as the result of *Re* increment is studied previously [66-68], transition as the result of geometrical change needs a better examination which can be a subject of future investigations.

Considering the *PF* introduced for this study, it seems that cases with slightly modulated channels perform much better for the *Re* range tested. Increments in performances up to 150% is observed for the converging-diverging configurations compared to the equivalent straight microchannel. A scattere plot of the performance factor *PF* as the function of channel expansion factor γ, reveals that performance factor peaks at around $\gamma = 1.5$ for almost all the *Re* tested.

Related publications

- **H. Ghaedamini, P. S. Lee, and C. J. Teo. "Enhanced transport phenomenon in small scales using chaotic advection near resonance." International Journal of Heat and Mass Transfer 77 (2014): 802-808.**
- **H. Ghaedamini, P. S. Lee, and C. J. Teo. "Fully developed flow in wavy walled microchannels." International journal of Heat and Mass Transfer. Accepted, under press**

Chapter 5. Developing Forced Convection in Converging-Diverging Microchannels

5.1. Introduction

Fully developed flow in converging-diverging microchannels was discussed in the previous chapter by considering a single furrow and periodic boundary condition at inlet and outlet. While such a computational domain provided a good understanding of the hydro-thermal performance of the modulated microchannels, it is beneficial to study the development of the flow inside the channel as it takes several construct for the flow to become fully developed hydrodynamically while the thermal development needs more furrows. Moreover, comparing the flow structure for developing and fully developed condition at different *Re* and for different geometrical conditions helps us to assess the validity of periodic boundary condition.

In this chapter, the effects of geometrical configuration on heat transfer performance and fluid flow of developing flow in converging-diverging microchannels are studied numerically. Geometrical parameters are again presented in non-dimensionalized format, i.e., aspect ratio S waviness λ and expansion factor γ. For five different aspect ratios and different levels of wall curvature, *Nu* and *f* are determined for three *Re*, i.e., 200, 400 and 600. In a comprehensive argument, different mechanisms that affect the performance of the microchannel design are addressed and at each level of waviness, the relative dominance of each mechanism is discussed. By studying the flow structure, counter rotating vortices created in the trough region are found to have an adverse effect on heat transfer while at highly pronounced levels of wall curvature, strong chaotic advection is observed which results in higher heat transfer rates albeit with higher pressure penalties. Thus, converging-diverging design can be considered as a planar design with which strong chaotic advection may be achieved. A Performance Factor (*PF*) is proposed to

capture heat transfer and pumping power characteristics of converging-diverging microchannels by comparing the wavy designs with their corresponding straight configurations. Based on the performance factor introduced, it is observed that the superiority of converging-diverging design shows itself at higher *Re* for which higher performance of up to 20% is observed.

5.2. Geometry and cases simulated

In Section 3.1 physical description of the converging-diverging microchannel heat sink geometry is presented. In order to study the hydro-thermal development of the flow in the converging-diverging microchannel, fluid domain of a single microchannel under constant wall temperature boundary condition is studied numerically in this chapter.

Table 5-1. Non-dimensional geometrical parameters of the cases simulated.

S = 0.5	S = 0.8	S = 1	S = 1.5	S = 2
λ=0, γ=1	λ=0, γ=1	λ=0, γ=1	λ=0, γ=1	λ=0, γ=1
λ=0.05, γ=2.33	λ=0.05, γ=1.67	λ=0.05, γ=1.5	λ=0.05, γ=1.31	λ=0.05, γ=1.22
λ=0.075, γ=4	λ=0.1, γ=3	λ=0.1, γ=2.33	λ=0.1, γ=1.73	λ=0.1, γ=1.5
	λ=0.15, γ=7	λ=0.15, γ=4	λ=0.15, γ=2.33	λ=0.15, γ=1.86
			λ=0.2, γ=3.29	λ=0.2, γ=2.33
				λ=0.25, γ=3

Figure 5-1 depicts the computational domain and the related geometrical parameters for reference. In order to study the geometrical parameters effect, five aspect ratios *S* with different levels of wall waviness are examined. The cases simulated are the same as the ones studied in the previous chapter which are tabulated in Table 5-1. These configurations are studied at different values of *Re*. i.e. 200, 400 and 600.

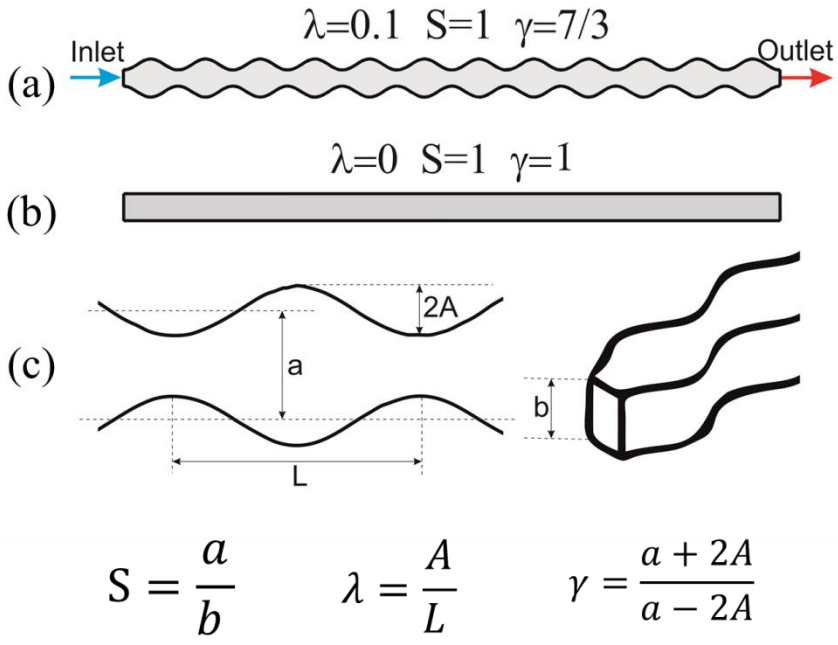

Figure 5-1. Computational domain. a) Converging-diverging configuration; b) its equivalent straight microchannel; c) geometrical dimensions of the microchannel.

5.3. Mathematical formulation and numerical procedure

For the aforementioned fluid domains, the governing equations describing the conservation of mass, momentum and energy are provided in Section 3.3. Assuming a flat velocity profile at inlet, cold fluid enters the microchannel with constant temperature of 300 K. It gains heat from the side walls and bottom which are kept at constant temperature 350K and it leaves the heat sink from the other side of the microchannel. Water as a Newtonian fluid with constant properties is considered as the coolant with the properties presented in Table 5-2.

Table 5-2. Thermo-physical properties of water.

Density ρ ($kg\ m^{-3}$)	**998**
Thermal conductivity k ($W\ m^{-1}\ K^{-1}$)	**0.6**
Specific heat capacity C_p ($J\ kg^{-1}\ K^{-1}$)	**4182**
Dynamic viscosity μ (Pa s)	**0.001003**

Heat transfer is characterized based on Nusselt number:

$$Nu = \frac{hD_h}{k} \tag{5-1}$$

where for a constant wall temperature boundary condition heat transfer coefficient is determined by:

$$h = q''.\frac{ln\left(\frac{T_w - T_{m,in}}{T_w - T_{m,out}}\right)}{\left(T_w - T_{m,in}\right) - \left(T_w - T_{m,out}\right)} \tag{5-2}$$

where q'' is the amount of heat gained by the coolant divided by the heat transfer area, i.e., side walls plus the bottom:

$$q'' = \dot{m}C_P(T_{m,in} - T_{m,out}) / A_{HT} \tag{5-3}$$

T_m is the mass flow averaged temperature and T_w is the wall temperature which is equal to 350K in this study.

$$T_m = \frac{\int_A T\left|\rho \mathbf{V} \bullet \overrightarrow{dA}\right|}{\int_A \left|\rho \mathbf{V} \bullet \overrightarrow{dA}\right|} \tag{5-4}$$

It should be noted that the derivation of log mean temperature considers a constant heat transfer coefficient which is not a function of temperature. Hence LMTD method is less valid for a developing flow condition where h is varying along the channel. However, based on the investigation by Sui et al. [64] the *Nu* calculated by LMTD method gives a value which is very close to the case where *Nu* is locally calculated and then averaged throughout the channel. Hence, above definition for heat transfer coefficient is also considered in this chapter.

5.4. Results and discussion

5.4.1. Hydro-Thermal performance

5.4.1.1. Heat transfer performance

Considering the definition provided previously for *Nu* and waviness λ, Figure 5-2 shows Nusselt number as a function of waviness. Cases with λ equal to zero are the straight microchannel designs with which other configurations are being compared. It is observed that increasing the waviness resulted in the increment in heat transfer. However, for cases with aspect ratio of 1 and above, there is a peak in *Nu* number which means that superiority in thermal performance is diminishing by increasing waviness afterwards.

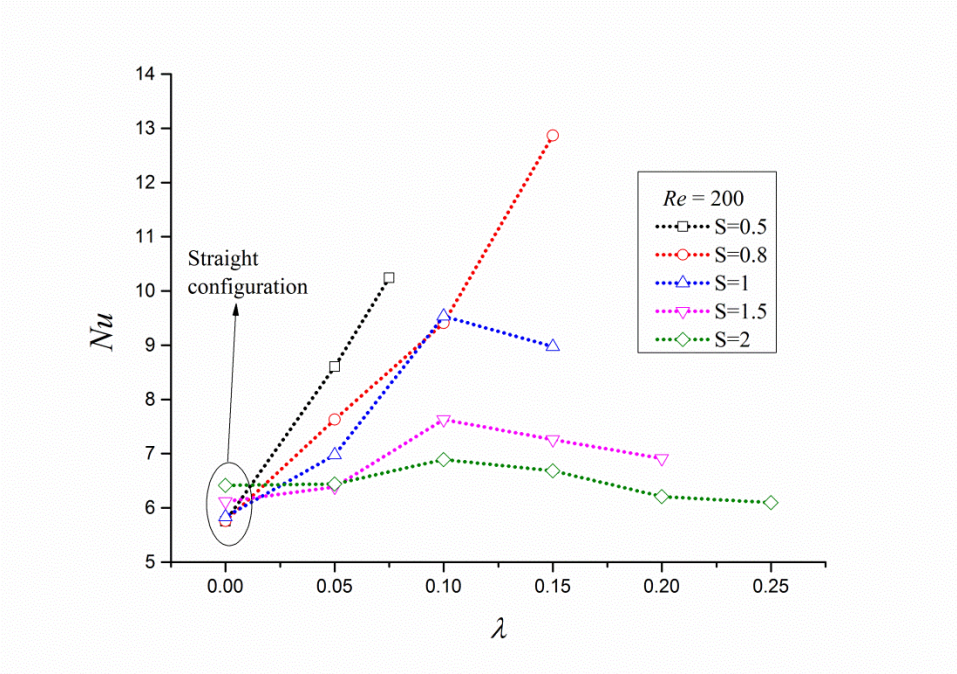

Figure 5-2. Developing Nusselt number as a function of waviness for *Re* = 200.

To explain the behavior observed, several mechanisms that affect the performance of such designs can be introduced as:

- Increment in heat transfer due to increase in heat transfer surface
- Decrease in heat transfer due to presence of dead areas as a result of counter rotating vortices in the trough region which makes the effective heat transfer area to diminish
- Increment in mixing and thereby heat transfer due to strong chaotic advection

For a specific aspect ratio *S* as waviness increases there are phases at which one of the above mechanisms are dominant. As defined in the earlier section, both the straight and converging-diverging designs have equal volumes and fabricating them on a test piece with the same footprint will result in the same number of channels. Thus, with the way that the channel geometry is constrained, increasing the waviness will result in increment of heat transfer area while total number of channels on a work piece is the same.

Figure 5-3 shows the temperature contour in the middle plane of the microchannel. For the purpose of comparison, results for only two configurations are presented here, i.e., configurations with S = 0.8 and S = 1 (corresponding to blue and red lines in Figure 5-2). The whole microchannel consisted of twelve furrows but only the central four furrows are presented here. Although a more detailed study on mixing is going to be presented in the next section, it is qualitatively observed that by increasing the waviness of the channel, core cold flow will diminish more and this is an indication of higher mixing and the resultant higher heat transfer rates. It is also of interest to see that for an equal waviness (e.g., λ = 0.10), cold core for cases with higher expansion factor occupy smaller volumes. Quantitatively, the volume occupied by fluid with temperature 305 K and below to the total fluid volume is 13% and 17% for γ = 2.33 and γ = 1.73 respectively. From Figure 5-3, it can qualitatively be seen that at λ = 0.05 there is no vortex in the trough region while for λ = 0.10, it seems that a well pronounced vortex is formed for the case of S = 0.8 compared with S = 1. However, a more systematic way of showing the vortical structures is needed to justify the comparison.

A vortex can be defined as a spinning flow of fluid, with the flow swirling around a center [108]. Indicating a vortex qualitatively can be simply done by capturing the vector field on a cross sectional plane. However, in this way, one may not be able to capture the vortices which are not forming in that plane. Thus, a three dimensional representation of vortices is of interest.

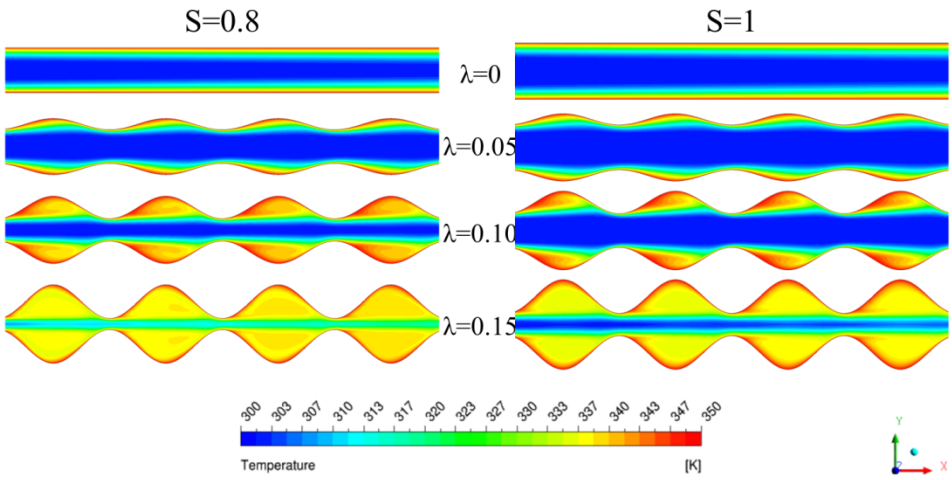

Figure 5-3. Middle plane temperature contours. Central four furrows are presented in this figure.

Figure 5-4 shows iso-surfaces of the *swirling strength* which indicates the strength of local swirling motion. A stronger vortex shows itself as a larger volume occupied by the iso-surface. For example, comparing the cases with λ = 0.1 and λ = 0.15, the latter have a stronger vortex region as it has a bigger vortex core shown. This can also be confirmed by considering Figures 5-3 and 5-4 together. It should be noted that the level defined for determining the iso-surface of swirling strength is identical for all the cases shown.

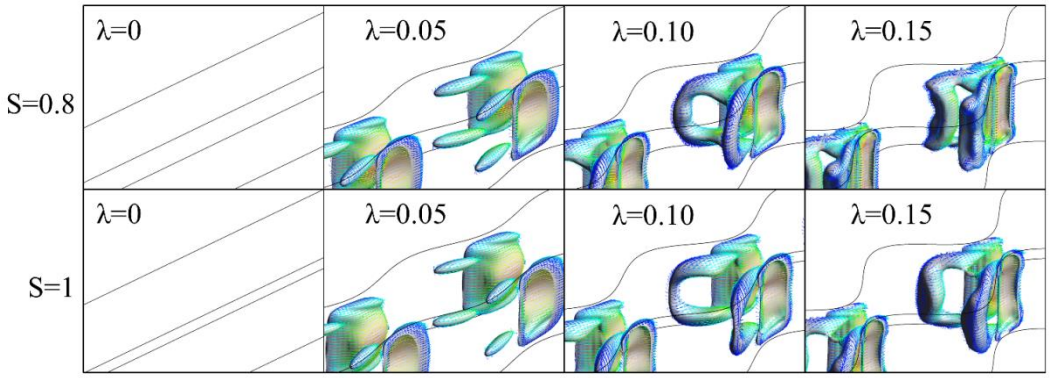

Figure 5-4. Vortical structure formation as a function of waviness. Flow direction is from left to right.

Figure 5-4 also exhibits the evolution of vortical structures as a result of varying the waviness. For straight microchannels, $\lambda = 0$, there are no vortical structures. By imposing a minor waviness to the wall, four streamwise vortices will form in the corner of the furrow near to the converging part. Increasing the waviness will result in the joining of the upper and lower streamwise vortices to form counter rotating vortices in the trough region of the furrow. In Figure 5-4, velocity vectors tangential to the iso-surface are also shown to provide a qualitative understanding of the flow motion.

With the big picture of the mechanisms affecting the thermal performance in mind, the behavior observed in Figure 5-2 can be explained. Considering the two cases with $S = 0.8$ and $S = 1$ in Figure 5-2, from the definition of expansion factor it can be inferred that for cases with identical waviness λ a higher aspect ratio S will result in a lower expansion factor γ. For smaller waviness, $\lambda = 0.05$, the dominant mechanism is the enhancement in heat transfer due to increment in heat transfer area and manipulation of boundary layer formation due to weak chaotic advection regime. At $\lambda = 0.05$, the trend in Figure 5-2 reveals that designs with greater expansion factor γ have superior heat transfer performance. Further increase in waviness, $\lambda = 0.1$, will result in formation of secondary counter rotating flow in the expansion region of the furrow. As can be seen in Figure 5-4, the vortical structure for the case with $S = 0.8$ is stronger and we can see in Figure 5-2 that Nu for $S = 0.8$ case is slightly less than $S = 1$ at $\lambda = 0.1$. This means that the adverse effect of the counter rotating vortices has overwhelmed the positive effect of increment of heat transfer area and manipulation of boundary layer formation. At $\lambda = 0.15$, two different behaviors are observed for the cases $S = 0.8$ and $S = 1$. For $S = 1$, the trend is logical: vortices created in the trough region are reducing the effective heat transfer area and compromising the overall performance of the channel. However, the case with $S = 0.8$ is not showing the same trend and there is a strong boost in heat transfer performance.

This is due to presence of strong chaotic advection which will be explained in the next section.

5.4.1.2. Fluid flow as a dynamical system

In Section 3.4 it was mentioned that advection problem from Lagrangian point of view can be treated as a finite dimensional dynamical system and in this way there is a correspondence between the phase space flow of the dynamical system and the spatial motion of an advected particle.

Although there are several ways to examine the presence of Eulerian chaos (temporal chaos) [67], for Lagrangian chaos, it is hard to quantitatively detect it. The method of Poincaré sections which is introduced in Section 3.4.5 and is used in previous chapter is an effective qualitative way of representing chaotic systems. For this purpose, 7500 massless particles are released along the centerline of the channel. A second order temporal scheme is invoked to calculate the particles' paths based on the computed velocity field. Subsequently, the positions of these particles are reported at the outlet surface. Figure 5-5 shows the microchannel with the surfaces at which Poincaré maps are shown later.

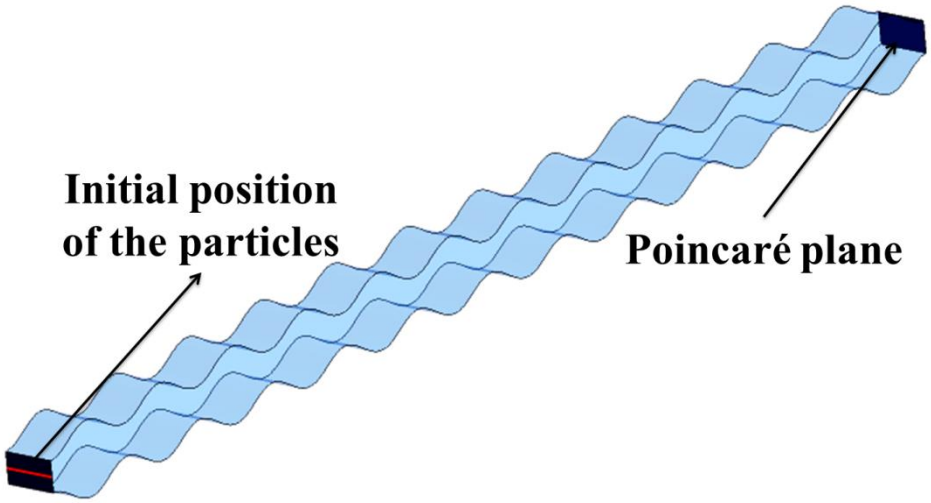

Figure 5-5. Poincaré map position. Particles are released along the red line in the middle of the inlet.

Figure 5-6 shows the Poincaré map for two aspect ratios, S = 0.8 and 1, and different values of waviness. Poor mixing in straight microchannels can be observed as for the cases with λ = 0, straight configurations, the captured particles congregate around the region they have been released at the inlet. From left to right in Figure 5-6, evolution of the Poincaré map as the result of curvature increment can be observed. At λ = 0.05, there is a tendency for the particles to travel to the center. Further increase in the waviness forces the particles to travel to the side walls and the case with S = 0.8 and λ = 0.15 shows a strong chaotic advection behavior. Now going back to Figure 5-2, we understand that the boost in heat transfer for λ = 0.15 of S = 0.8 is a consequence of the presence of strong chaotic advection. Comparing λ = 0.15 for S = 0.8 and S = 1, the importance of expansion factor is revealed. These two cases with equal wall waviness will show two different behaviors as a result of difference in their expansion factor.

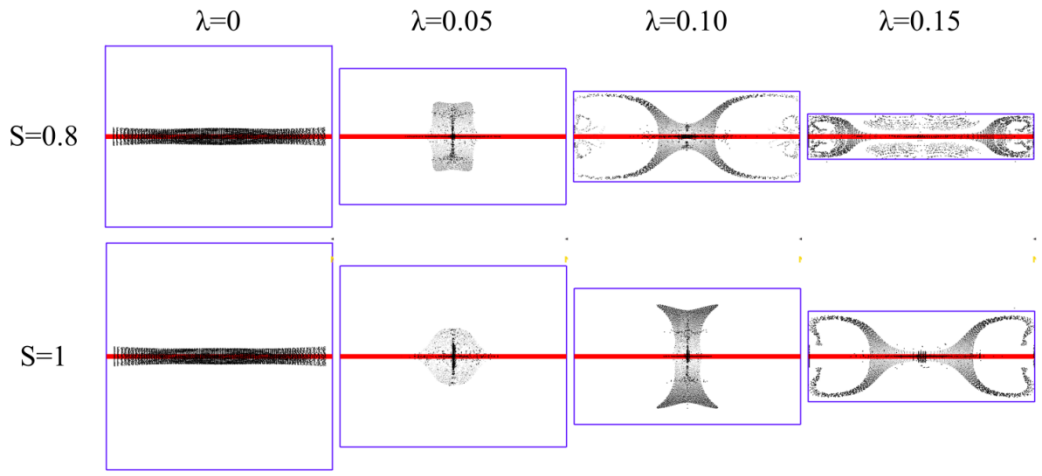

Figure 5-6. Poincaré map for the cases with *Re* = 200.

5.4.1.3. Pressure drop

Figure 5-7 shows the Dearcy friction factor as a function of waviness, λ.

$$f = -\frac{\Delta P}{L} \times \frac{2D_h}{\rho U_m^{\,2}} \tag{5-5}$$

where ΔP is the pressure drop from inlet to outlet.

For all the cases, increasing the waviness will result in increasing the friction factor. However, for higher aspect ratios, S, this increment is less pronounced. The high peak for the case with S = 0.8 and λ = 0.15 is accompanied by the fact that there appears to be a strong chaotic advection regime for this case from the Poincaré maps presented in Figure 5-6.

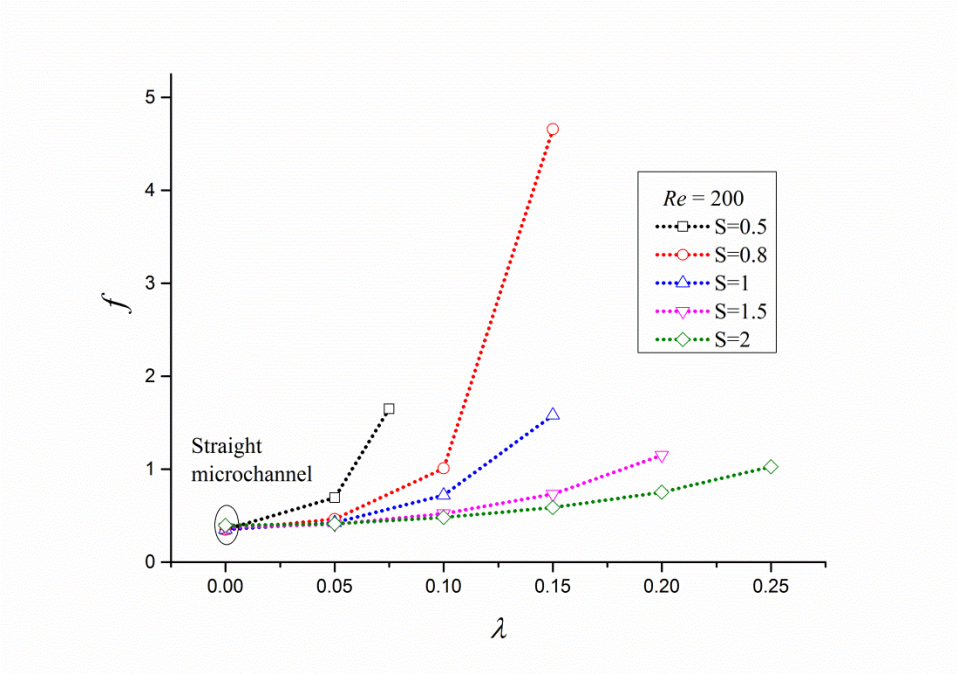

Figure 5-7. Friction factor as a function of waviness λ for the cases with *Re* = 200.

5.4.2. Performance Factor

When dealing with heat transfer augmentation techniques, there is always a debate regarding the definition of the performance factor which indicates the superiority of a configuration. There are many factors which can be taken into consideration, like hydrothermal performance, initial cost, pumping power, operating cost, maintenance cost, and etc. As a general rule, it can be seen that higher heat transfer rates, Figure 5-2, are made possible at the expense of higher pressure drops, Figure 5-7. These two can be combined by introducing the performance factor as the ratio of the amount of heat dissipated by the fluid and the pumping power of the channel while each case is compared with its equivalent straight design with width of *a* and depth of *b*:

$$PF = \frac{\left(\frac{Q}{PP}\right)_{wavy}}{\left(\frac{Q}{PP}\right)_{straight}} \tag{5-6}$$

where Q is the heat transfer rate and PP is the pumping power:

$$Q = \dot{m} C_p \left(T_{out} - T_{in} \right) \tag{5-7}$$

$$PP = \frac{\dot{m} \Delta P}{\rho} \tag{5-8}$$

$\dot{m}$ is the mass flow rate and T_{out} and T_{in} are the mass flow averaged temperatures at outlet and inlet, respectively.

This definition was used in some previous works [23, 64, 65]. It should be noted that the performance evaluation presented here is not an optimization criterion; it serves to give the intuition of heat transfer and pumping power variation as a result of varying the waviness of the channel. Figure 5-8 presents the data calculated for the PF at Re = 200.

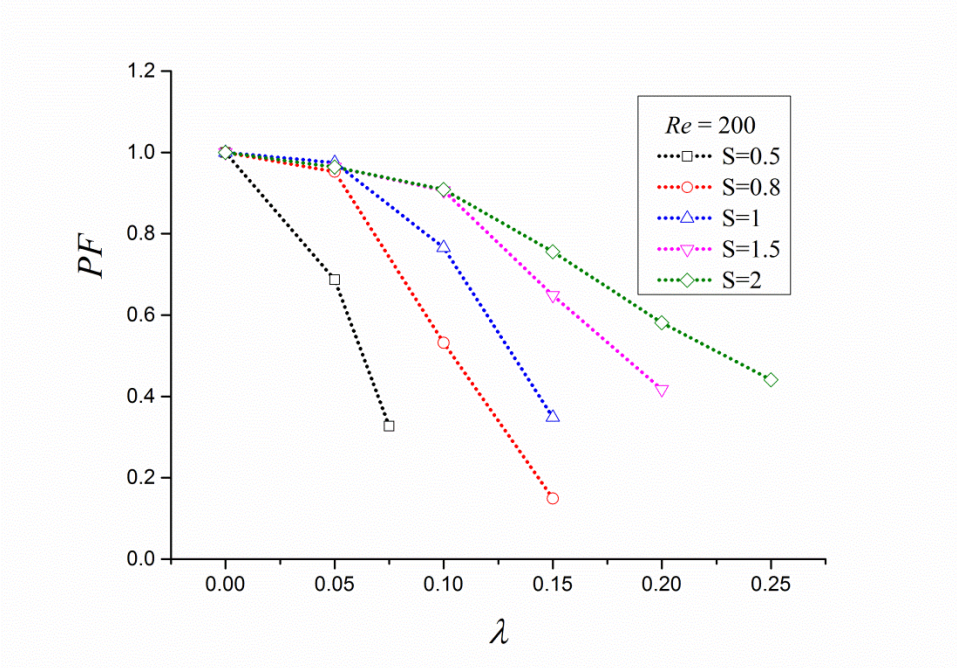

Figure 5-8. Performance factor as a function of waviness λ for the cases with *Re* = 200.

5.4.3. Effect of Re

To have a comprehensive parametric study, the effect of mass flow rate increment is investigated in this part by varying the Reynolds number. Figures 5-9 and 10 show *Nu* as a function of wall waviness for *Re* = 400 and *Re* = 600. The trends in the presented graphs can be explained by considering the dominant physical phenomena in the system. For smaller values of λ, increment in wall curvature will result in an increase in heat transfer area and also an increase in wall shear stress which, based on Reynolds analogy, will result in better heat transfer (Figure 5-11). Increasing the waviness further, two counter rotating vortices will be created in the trough region which will result in a decrease in heat transfer. At the same time, advection regime may migrate towards stronger chaotic behavior which will increase heat transfer. These three mechanisms create the increasing-decreasing-increasing behavior observed in thermal performance trend of converging-diverging microchannels as it can be seen for *S* = 1, 1.5 and 2 in Figures 5-9 and 10.

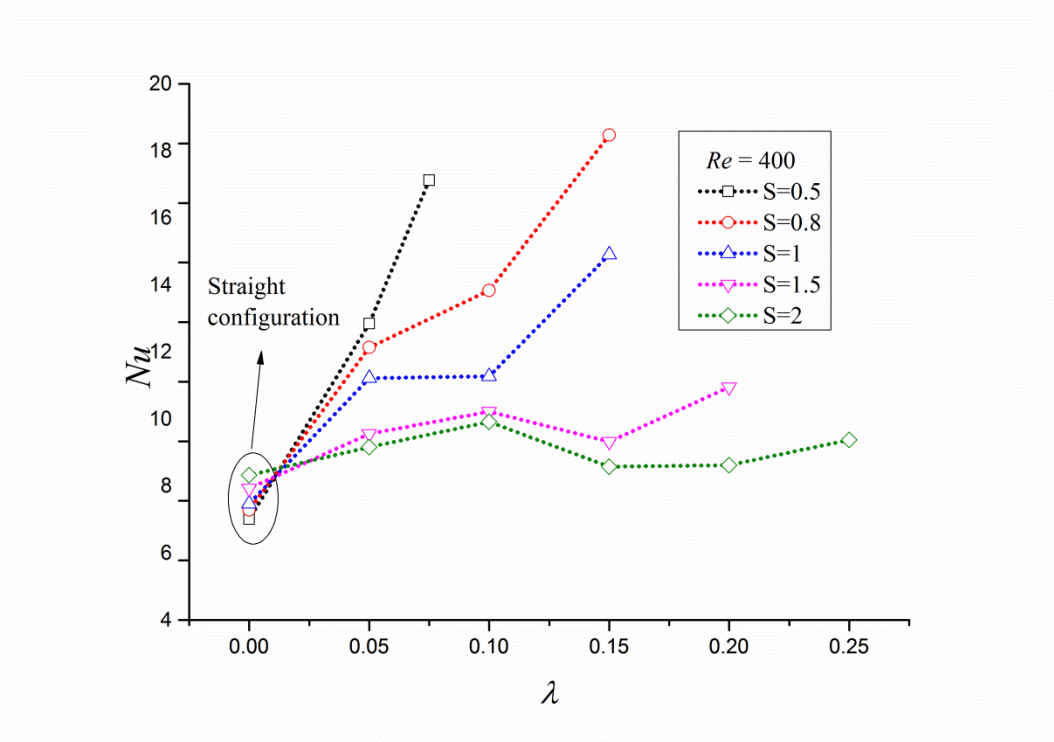

Figure 5-9. Developing Nusselt number as a function of waviness for *Re* = 400.

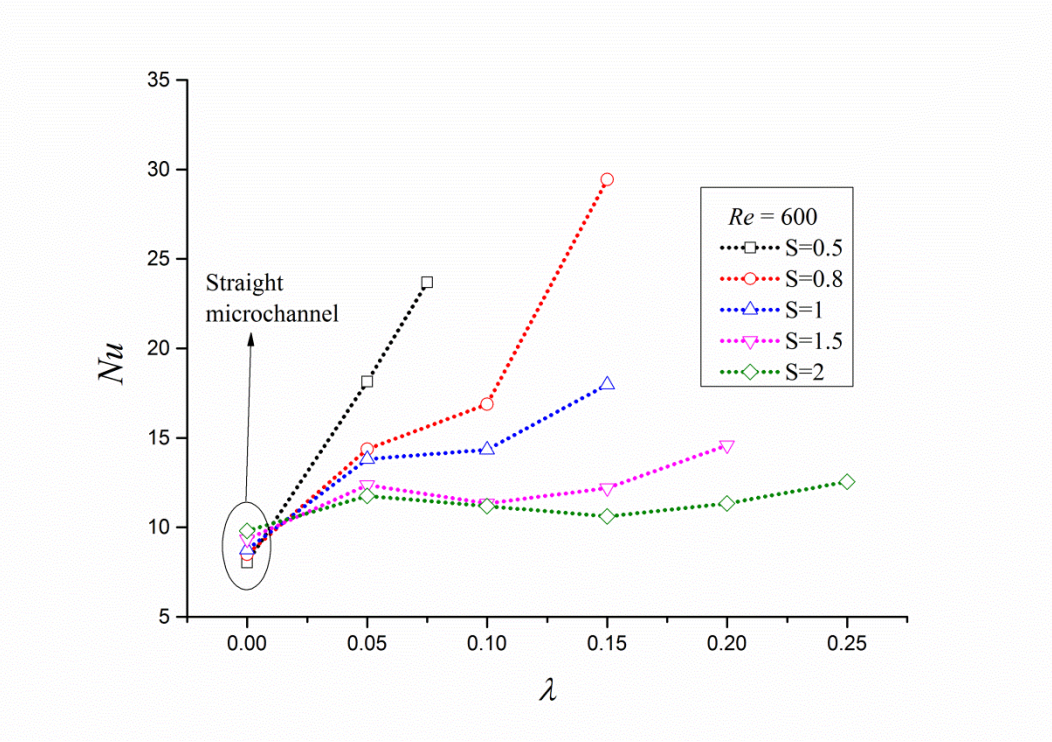

Figure 5-10. Developing Nusselt number as a function of waviness for *Re* = 600.

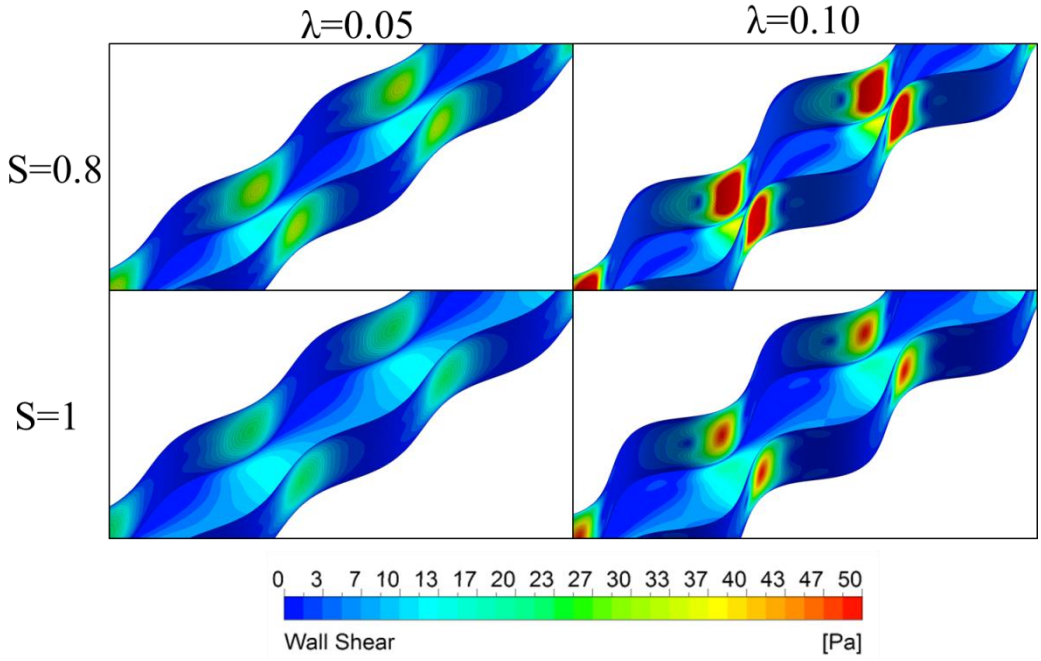

Figure 5-11. Wall shear stress contour for *Re* = 200.

Based on the results of this chapter and the previous one, we believe that there are two parameters that mainly affect the presence of chaotic advection: Reynolds number and expansion factor. As *Re* increases, expansion factors at which transition to strong Lagrangian chaos occurs decreases. For example, for *Re* = 200, cases with γ = 4 and higher showed strong chaotic advection while this reduced to γ = 2.33 and above for higher *Re*. Figures 5-12 and 13 show the Poincaré map located at the outlet of the microchannel for *Re* = 400 and 600, respectively. It is seen that at higher *Re*, even cases with moderate expansion factor are showing strong chaotic advection behavior.

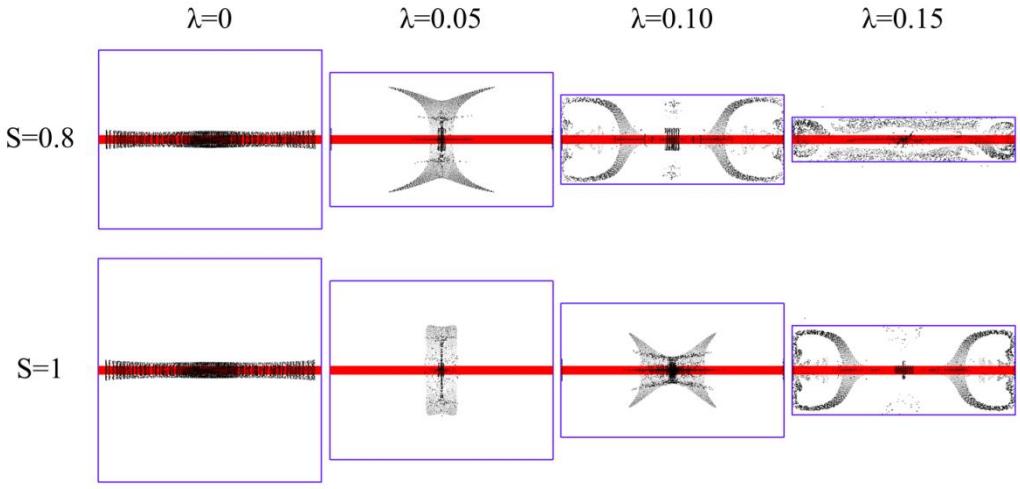

Figure 5-12. Poincaré map for the cases with *Re* = 400.

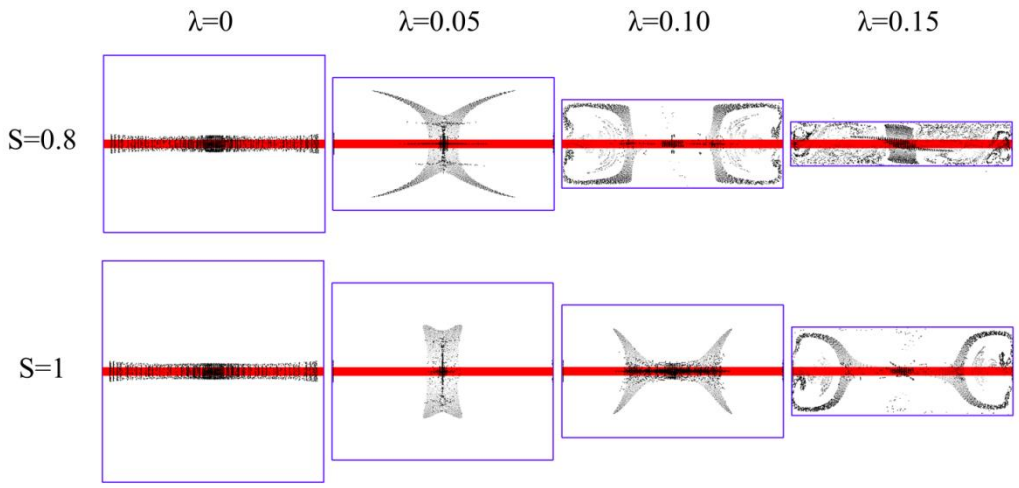

Figure 5-13. Poincaré map for the cases with *Re* = 600.

Figures 5-14 and 15 represent the performance factor for cases with *Re* = 400 and 600 as function of waviness. We can see increase of up to 20% with higher *Re* which shows that the superiority of converging-diverging configuration is pronounced at higher *Re*.

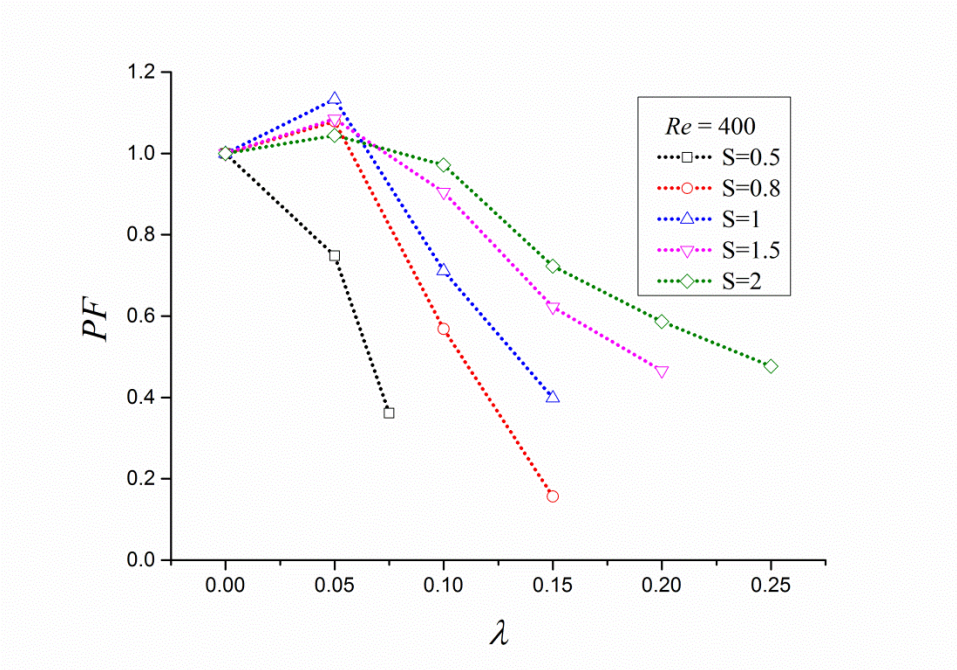

Figure 5-14. Performance factor as a function of waviness λ for the cases with *Re* = 400.

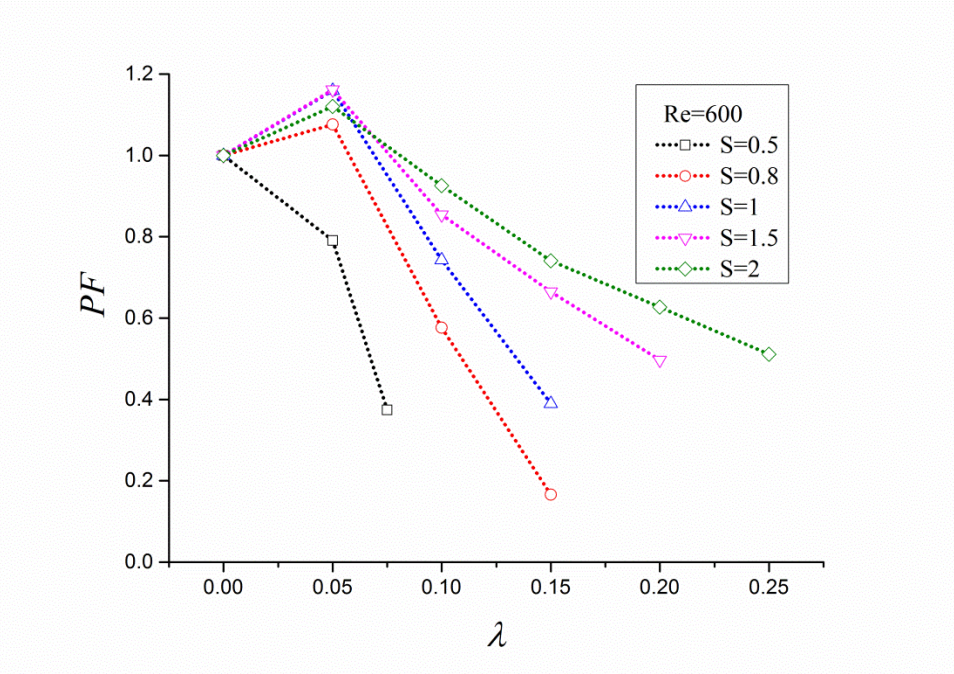

Figure 5-15. Performance factor as a function of waviness λ for the cases with *Re* = 600.

5.4.4. Comparison with fully developed condition

Figure 5-16 shows the comparison between developing and fully developed *Nu* and *f* for *Re* = 200. It is seen from this figure that *f* for the two cases is almost the same which indicates that flow develops hydrodynamically relatively fast. On the other hand, there are differences observed for *Nu* graphs as *Nu* for developing condition is larger than the fully developed condition which is anticipated. It is seen that fully developed flow assumption can predict the trends to a good extent and this result helps the designers to use a less computationally extensive model for their applications.

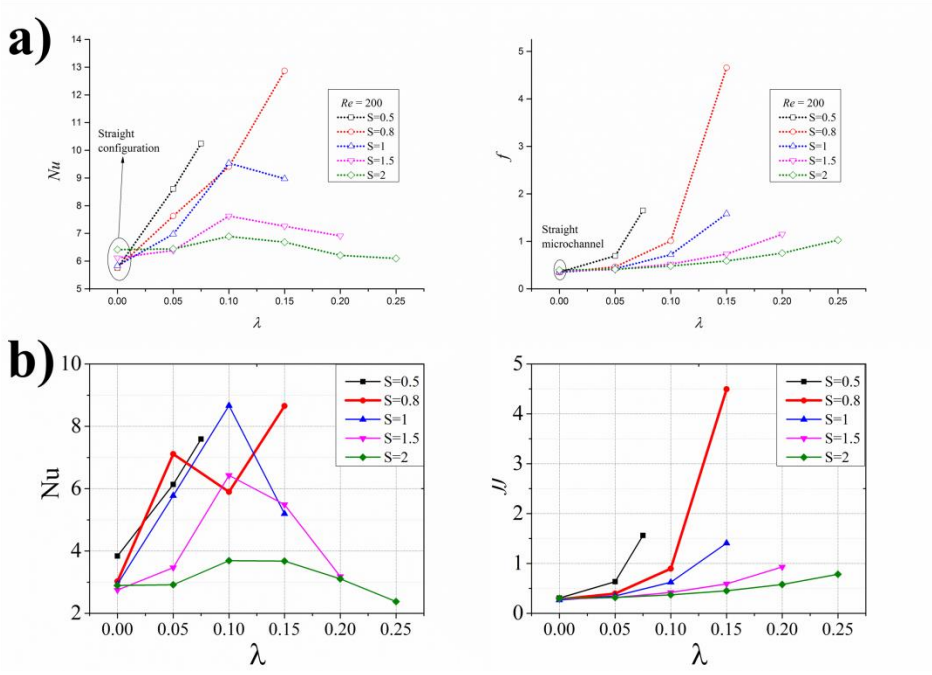

Figure 5-16. *Nu* and *f* for a) developing and b) fully developed condition for *Re* = 200.

5.5. Conclusion

In this chapter a parametric study on converging-diverging microchannel shapes is presented. It is seen that these designs can be introduced as planar configurations for which chaotic advection is present. The geometry is represented by three dimensionless parameters and the effect of each on the thermal performance of the heat sink is discussed. Expansion factor γ and Reynolds number are introduced as the two main parameters that control the presence of strong chaotic advection in the system as by increasing the Reynolds number, strong chaotic advection occurred at smaller expansion factors, which implies that at relatively higher *Re*, slightly modulated channels may also show strong chaotic advection regime.

Mechanisms that affect the thermal performance of the channel are addressed in this chapter and it is observed that:

- Increasing the waviness will result in better heat transfer performance as long as two counter rotating vortices are not present in the trough region. Attempts have been made to identify these vortices by detecting the regions at which swirling strength is higher than a threshold. Vortical structures detected in this way completely explain the behavior observed.
- For the cases with strong chaotic advection, heat transfer increases drastically albeit with a higher pressure drop penalty.

The aforementioned mechanisms create an increasing-decreasing-increasing trend in heat transfer performance of the converging-diverging channels as wall waviness is increased.

Related publications

- **H. Ghaedamini, P. S. Lee, and C. J. Teo. "Developing forced convection in converging–diverging microchannels." International Journal of Heat and Mass Transfer 65 (2013): 491-499.**
- **H. Ghaedamini, P. S. Lee, and C. J. Teo. "Forced pulsatile flow to provoke chaotic advection in wavy walled microchannel heat sinks." Thermal and Thermomechanical Phenomena in Electronic Systems (ITherm), 2014 IEEE Intersociety Conference on. IEEE, 2014.**

Chapter 6. Experimental investigation of single phase forced convection in wavy walled microchannels

6.1. Introduction

In previous chapters, fully developed and also developing flow in converging-diverging microchannels were studied and the effect of geometrical and flow parameters on hydro-thermal performance of such configurations were investigated. The numerical investigation showed that the presence of chaotic advection in the system can be related to the superior thermal performance of such configurations. Here experimental examination is performed to validate our numerical findings.

In this chapter, heat sinks with wavy walled microchannels are studied experimentally. A range of $0 < \lambda < 0.15$ for wall waviness is investigated : straight microchannel design with $\lambda = 0$, slightly modulated channel with $\lambda = 0.05$, moderately modulated with $\lambda = 0.1$ and highly modulated with $\lambda = 0.15$. In this way, by considering the Reynolds number range, $100 < Re < 800$, different flow conditions at different levels of wall modulation will be covered.

The results of the experimental study are compared with two numerical studies at different boundary conditions. The first condition considers the fluid domain with the constant temperature boundary condition, a domain similar to the one presented in chapter 5. The second condition is the conjugated simulation which considers both the fluid domain and also the solid substrate. Our results show that the constant temperature boundary condition can predict the thermal performances to a good extent. Moreover, pressure drop prediction generally matched the experimental results.

6.2. Experimental set-up and data reduction

6.2.1. Experimental loop

Figure 6-1 shows a schematic diagram of the experimental setup being used to study the fluid flow and heat transfer of wavy walled microchannels. This experimental vehicle is similar to the ones being used by Sui et al. [64] and Lee et al. [109]. A three gallon tank is used to contain the deionized water while a positive displacement gear pump (Cole-Parmer 75211 – 35) is driving the coolant in the test rig. The tank has heater elements embedded inside it which are used to boil the water for degasifying purposes before starting the experiments. The bypass line and the air to liquid heat exchanger are used to cool down the boiled water in the tank and in this way the degassed water is prepared for use in the experimental loop.

After the pump is switched on, the fluid flow enters a 15 μm filter and then a turbine flow meter (McMillan Co. 104 6HY Flo-Sen) which has a range of 100 – 1000 ml/min. In order to maintain the inlet temperature, a compact liquid to liquid heat exchanger is used after the flow meter. Fluid then enters the test piece where the wall temperature as well as the fluid temperature and pressure drop will be measured and a DAQ system will collect the data. A liquid to air heat exchanger (Thermatron 735SPC2A01) is used after the test piece in the loop to reduce the enthalpy of the fluid flow and then the fluid subsequently returns back to the tank and the circulation of the coolant continues, Figure 6-1.

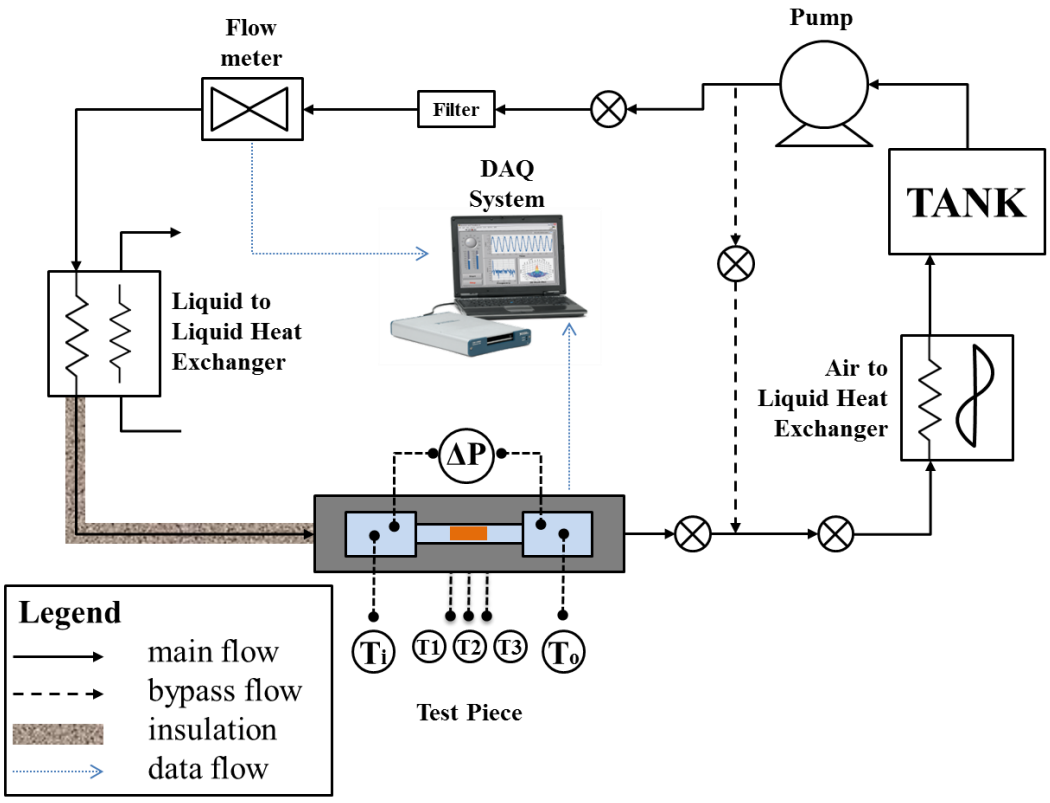

Figure 6-1. Schematic diagram of the flow loop.

6.2.2. Test sections

Figure 6-2 shows the schematic diagram and the test piece block which is used in this study. The test section consists of a copper block and a housing which is made of Teflon material and the top cover which is made of polycarbonate. The copper block has a heat transfer area of $25\text{mm} \times 25\text{mm}$ while the third dimension is 69.5mm. Microchannels are manufactured on the top of the copper block and they have a converging-diverging shape with depth of 600 µm.

Figure 6-3 shows the converging-diverging configuration with the main geometrical parameters shown on it. These dimensions are:

- Average channel width *a*
- Channel depth *b*

- Wave amplitude A
- Wave length L
- Number of furrows N
- Fin width, S_w

The geometry and the dimensionless parameters are presented in details in Chapter 3.

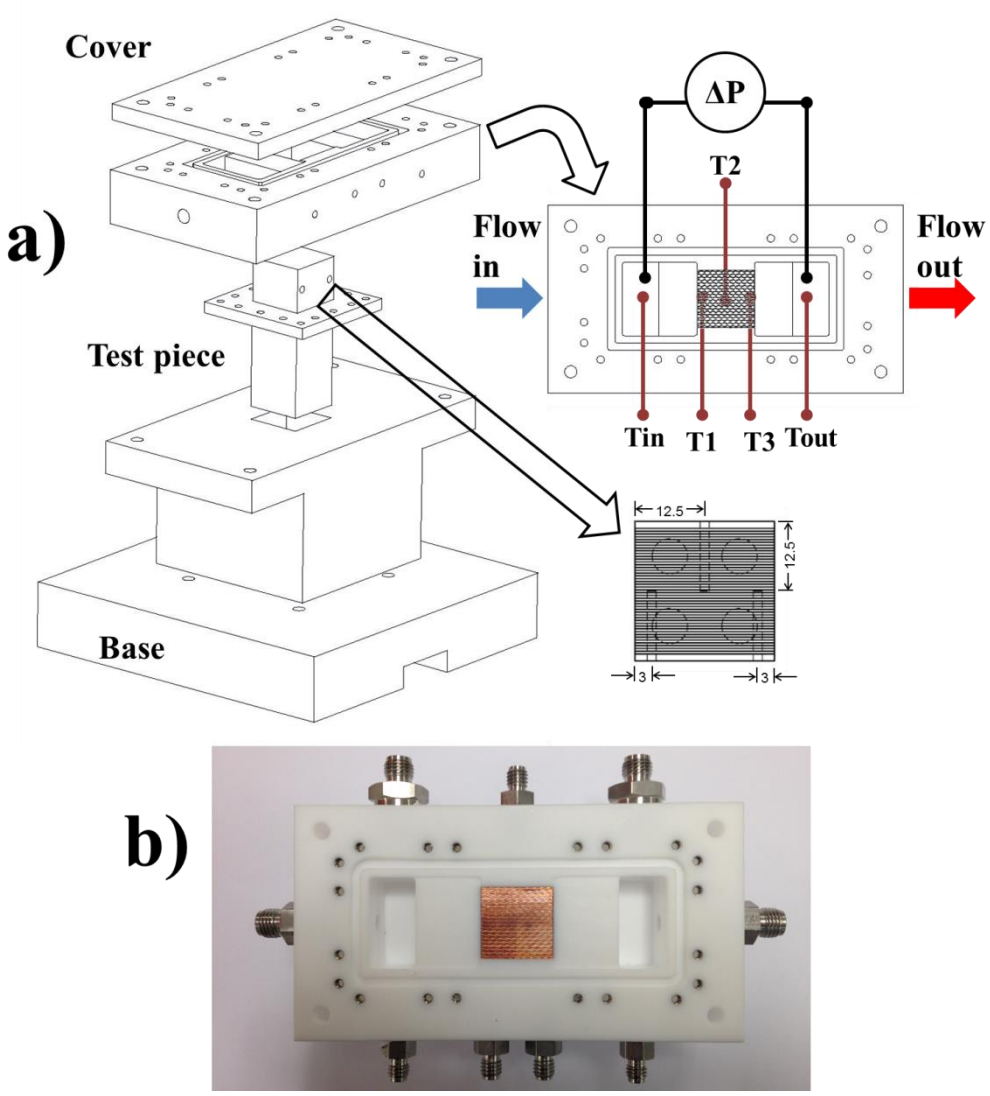

Figure 6-2. a) Test piece schematic diagram. Location of the thermocouples and pressure transducer are presented. b) Actual manifold and the test piece.

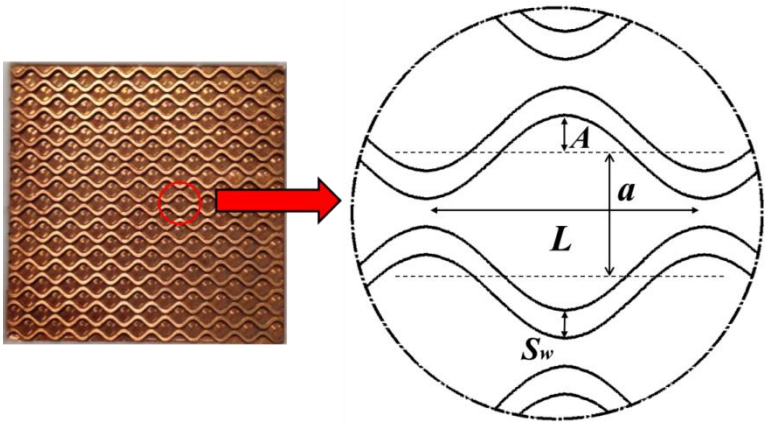

Figure 6-3. Converging-diverging architecture with the main geometrical parameters being presented.

For this experimental investigation, four configurations are manufactured which have equal aspect ratio S = 1.67 but with different levels of wall waviness λ. The dimensions of the test pieces are presented in Table 6-1. Each microchannel consists of 10 furrows (N = 10) and a total number of 20 microchannels are fabricated on the top of the copper block. Since the average width of the channels is kept constant, the total number of microchannels fabricated on the top of the copper is the same for all the cases. As mentioned previously, these test pieces have different levels of wall modulation: The straight test piece which has a waviness λ equal to 0, slightly modulated test piece with waviness λ = 0.05, moderately modulated test piece with waviness λ = 0.1 and highly modulated test piece with waviness λ = 0.15, Table 6-1.

At the bottom of the copper block, there are four holes where four cartridge heaters (Watlow E1J35-E12 250W) are placed. The heaters provide combined power of 1000 W, Figure 6-4. The voltage input to the cartridge heaters is controlled by a DC power supply unit. In order to measure the temperature of the copper block, three type T thermocouples are inserted inside the copper block as shown in Figure 6-4. The horizontal distances of the thermocouples from the inlet are 3 mm, 12.5 mm and 22 mm respectively. The

vertical distance of the thermocouples to the base of the microchannels S_v is 9.4 mm. The temperature reading of these thermocouples is then used to determine the average base temperature for the fins (microchannel walls).

Table 6-1. Dimension of the test pieces experimented.

Case	L (mm)	a (mm) $\pm 14\mu m$	A (mm) $\pm 10\mu m$	b (mm) $\pm 10\mu m$	S_w (mm) $\pm 14\mu m$	N
λ = 0	2.5	1	0	0.6	0.25	10
λ = 0.05	2.5	1	0.125	0.6	0.25	10
λ = 0.10	2.5	1	0.250	0.6	0.25	10
λ = 0.15	2.5	1	0.375	0.6	0.25	10

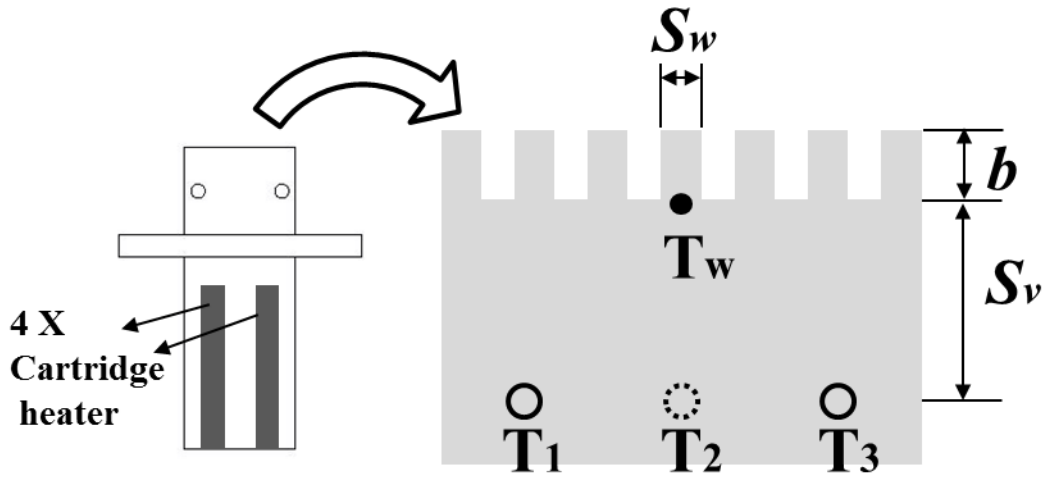

Figure 6-4. Position of thermocouples and the cartridge heaters in the copper block.

In order to measure the coolant temperature at inlet and outlet, two type T thermocouples are placed in the housing to measure the average values of fluid temperature as shown in Figure 6-2. In order to increase the accuracy of the pressure drop readings, two gauge

pressure transducers (Omega PX409-015G5V) are being positioned at inlet and outlet while a bidirectional differential pressure transducer (Setra Model 230) measures the pressure difference between inlet and outlet. These values are then averaged and the pressure drop at the channels is reported. A computer controlled DAQ system (NI-DAQ-9172) is used for data capturing.

6.2.3. Experimental procedure

All the experiments are performed following a standard procedure in a room with constant temperature. In order to eliminate the dissolved gases, coolant is boiled for 1.5 hour and cooled down before each experiment. After mounting the test piece into the test vehicle, the gear pump is turned on and its speed is gradually increased until the desired flow rate is reached. Meanwhile, all the temperatures and pressure drop readings are monitored and after reaching a steady state which is usually attained after 30-45 minutes, values of thermocouples and pressure transducers are stored for 60 seconds and subsequently time averaged to give an experimental data. Due to the restrictions regarding the differential pressure transducer range (-60 mbar to 60 mbar), for highly modulated test piece (λ = 0.15), Reynolds numbers only up to 600 were tested.

6.2.4. Data reduction

As with previous chapters, Reynolds number is determined by:

$$Re = \frac{\rho U_m D_h}{\mu} \tag{6-1}$$

for which the fluid properties are determined based on the mean temperature of the fluid and D_h is the hydraulic diameter of the equivalent straight microchannel, Equation 6-2), and U_m is the average velocity determined by the volume flow rate $\dot{V}$ being read from the flow meter and considering the cross section of the equivalent straight microchannel:

$$D_h = \frac{4 \times ab}{2(a+b)} \tag{6-2}$$

$$U_m = \frac{\dot{V}}{ab} \tag{6-3}$$

Following the procedure taken by Lee et al. [110], the amount of heat transferred to coolant for steady state liquid cooling is calculated by:

$$q = \rho c_p \dot{V} (T_{m,out} - T_{m,in}) \tag{6-4}$$

where $\dot{V}$ is the volumetric flow rate and is determined experimentally by the flow meter. $T_{m,in}$ and $T_{m,out}$ are the fluid temperatures at inlet and outlet which are measured by the thermocouples placed upstream and downstream of the microchannel test piece. Properties of the coolant, density and specific heat capacity are determined based on the mean flow temperature T_m from inlet to outlet.

In order to define the heat transfer coefficient, wall temperature is needed. Although it is difficult to directly measure the wall temperature, it can be calculated using extrapolation of the temperature readings from the thermocouples embedded in the copper block. By assuming a 1D conduction which is valid due to the high conductivity of copper and also insulated walls around the block [110], it can be written as:

$$T_w = (0.25T_1 + 0.5T_2 + 0.25T_3) - \frac{S_v q''}{k_{Cu}} \tag{6-5}$$

T_1, T_2 and T_3 are the temperature readings in the copper block whose positions are shown in Figure 6-4. The distance S_v is the vertical distance of the thermocouples to the base of the fins and is equal to 9.6 mm. k_{Cu} is the conductivity of copper and q'' is the average heat flux based on the foot print area A_{FP} = 6.25 cm^2:

$$q'' = \frac{q}{A_{FP}} \tag{6-6}$$

Based on the calculated wall temperature, the average heat transfer coefficient can be determined using

$$h = \frac{q}{M(A_{cb} + 2A_{cs}\eta)(T_w - T_m)} \tag{6-7}$$

where M = 20 is the number of channels. A_{cb} is the convective bottom area of the channel and A_{cs} is the side wall area of the channel. Since the temperature calculated for the wall is the base temperature of the fins, fin efficiency is considered for the side walls assuming an adiabatic tip condition for the fin and hence:

$$\eta = \frac{\tanh(mb)}{mb} \tag{6-8}$$

$$m = \frac{2h}{k_f S_w} \tag{6-9}$$

where b is the channel depth or fin height and S_w is the fin thickness which is equal to 0.25 mm. An iterative method is used to calculate the fin efficiency starting from the assumption of the fins being 100% efficient, h is determined first and then the new fin efficiency is calculated with the new value of h. This procedure is repeated until the change in the value of calculated h was less than 0.1%. The range for the fin efficiency in this investigation was between 96 to 98 %.

The average Nu can then be calculated using:

$$Nu = \frac{hD_h}{k_f} \tag{6-10}$$

where D_h is the hydraulic diameter with the definition presented in Equation 6-2 and k_f is the thermal conductivity of the water which is determined based on the mean temperature T_m of the fluid.

Friction factor for current study is defined as

$$f = \frac{(dp/dx)D}{0.5\rho U^2} \tag{6-11}$$

where the differential pressure are obtained from the differential pressure transducer.

6.3. Numerical simulations

Two sets of numerical simulations with different thermal boundary condition are performed, i.e. constant temperature boundary condition and conjugated simulation which considers both convection in the microchannels and conduction in the copper substrate. In the following sections, these numerical simulations will be explained.

6.3.1. Computational domain

Microchannel heat sinks being studied consist of 20 channels with varying degree of waviness. However, due to the complexity of a full domain simulation and the fact that the computational costs of such an study is extremely high, a single channel domain with two thermal boundary conditions were considered as the computational domains. Figure 6-5 shows the domains which are considered for these simulations. For constant temperature boundary condition, fluid domain of a single channel is considered while for the conjugated simulations, a construct which consists of the wavy fin with symmetric boundary conditions in the fluid domain and solid domain is considered, Figure 6-5b. These computational domains were introduced in Chapter 3 and the constant temperature boundary condition was used in Chapter 4. For the conjugated cases, in order to prevent any back flow, the fluid domain was further extended, Figure 6-5b. Furthermore, it makes

it very similar to the experimental configuration. Symmetry boundary condition is considered for the sides of the domain in the conjugated simulations.

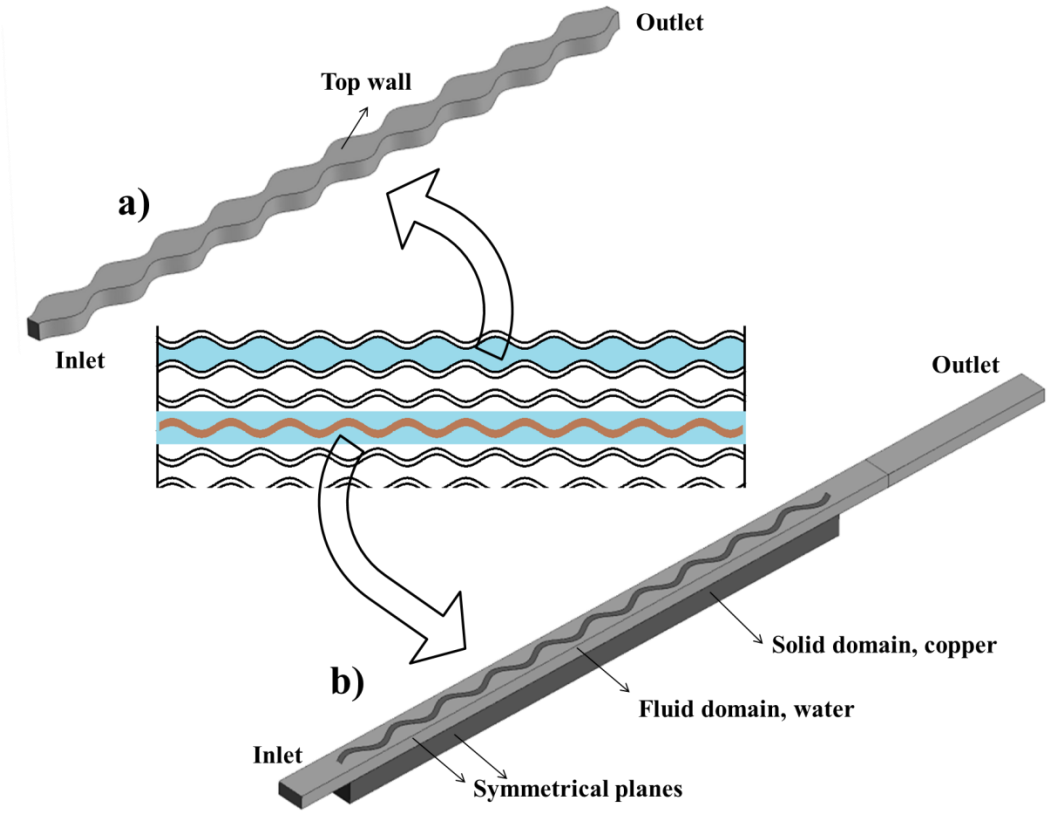

Figure 6-5. Computational domains for the simulations. a) Computational domain for a single channel with constant temperature boundary condition. b) Computational domain for a single construct with symmetric boundary conditions.

6.3.2. Mathematical model

Water as the coolant is considered for the fluid domain while solid substrate is considered to be made of copper. For conjugated simulations, properties of water are considered to be a function of temperature. On the other hand, for constant temperature simulations, all properties were considered to be constant. For both cases, fluid flow is assumed to be laminar with negligible viscous dissipation and since the minimum dimension is larger

than 10μm [96], conservation of mass and momentum as well as energy are the ones already being presented in Section 3.3:

6.3.3. Boundary conditions

6.3.3.1. Conjugated simulations

Considering the computational domains presented in previous sections, for conjugated simulations, conservation of energy at the solid-liquid interface requires that:

$$-k_s \frac{\partial T_s}{\partial n} = -k_f \frac{\partial T_f}{\partial n} \tag{6-12}$$

and

$$T_s = T_f \tag{6-13}$$

where n is the normal vector and k_f and k_s are the thermal conductivities of the fluid and solid respectively.

In order to have the maximum similarity with actual condition for the conjugated simulations, the fluid domain is extended to represent the inlet and outlet manifolds and also to prevent the back flow, Figure 6-5b. Heat is applied at the bottom while symmetry boundary condition is applied at the sides. The top wall is considered to be adiabatic for both fluid and solid domains and constant flow velocity is applied at the inlet with constant temperature of 300 K. The utlet pressure is set to be 1 atm, atmospheric pressure.

6.3.3.2. Constant temperature condition

For constant temperature boundary condition, the bottom wall as well as side walls were set at constant temperature, T = 350, while constant velocity boundary condition was

applied at inlet with constant fluid temperature of 300 K. The inlet velocity was determined in a way to satisfy the desired *Re*. The Top wall was set to be adiabatic.

6.3.4. Domain discretization and solver control

Gambit and ANSYS MESH were used to generate the structured grid for single channel fluid and conjugated domains respectively. A mesh independence study is done similar to the previous chapters. Total number of elements for the single channel domain was around 3.5 million while for conjugated simulations it was around 5 million depending on the case.

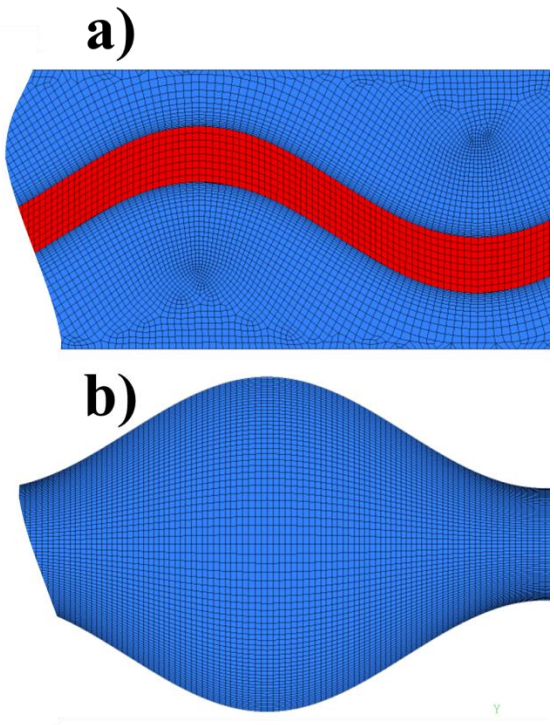

Figure 6-6. Grids being used for a) the conjugated simulation and b) constant temperature boundary condition.

Finite volume software, CFX 14.5, was used to solve the system of partial differential equations presented in Section 3.3 along with the boundary conditions discussed in previous section. The second order upwind scheme was used to model the combined

convection-diffusion phenomenon in transport equations. The solid-fluid interface was modeled by a one to one condition which is used when the mesh at solid and fluid side of the interface are identical. Convergence was considered when the residuals for mass and momentum as well as energy equations were less than 1e-6.

The definitions for *Nu* and friction factor are previously presented in Chapter 5.

6.4. Results and discussion

6.4.1. Thermal performance

Figures 6-7 to 6-10 depict the numerical and experimental Nusselt number as function of *Re* for different levels of wall waviness. The trends predicted by the numerical results are similar to the experimental ones which reveal that the numerical code can predict the actual system to within 25% difference. However, at smaller wall waviness the numerical results are under-predicting the thermal performance while for configurations with higher wall modulation, λ = 0.1 and λ = 0.15, there is a very good agreements between the results with less than 12% difference. The under-prediction for the straight design and slightly modulated design may be due to several reasons like the numerical domain selection which considers one channel and not the whole physical domain thus not considering flow maldistribution, and also the experimental uncertainty.

Another finding here is the validity of constant temperature boundary condition. From our results it is observed that constant temperature boundary condition can very well predict the trend and for wavy walled cases, it has results closer to experimental values compared to the conjugated simulations with symmetry boundary condition. One reason for good agreement of constant temperature boundary condition is due to the high value of fin efficiency which is greater than 95%. This indicated that constant temperature

boundary condition is indeed a good representation for such designs of microchannel heat sinks.

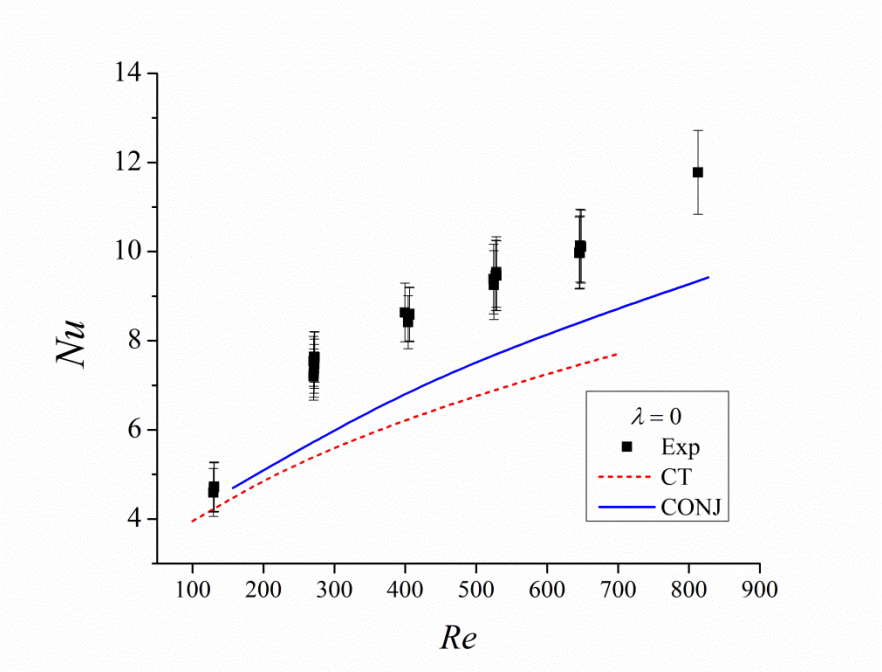

Figure 6-7. *Nu* as a function of *Re* for the straight configuration case, $\lambda = 0$.

From Figures 6-7 to 6-10 it can be observed that the Nusselt number uncertainty for higher *Re* decreases with wall waviness. From the data reduction equations presented in Section 6.2.4 and also Appendix A, it is obvious that the heat transfer coefficient reported is sensitive to the fluid temperature difference; hence it is important to have sufficiently large fluid temperature difference for better accuracy. This can be achieved by maximizing the heat flux. However, there was a limitation regarding the heat flux due to subcooled boiling. After a certain level of heat flux imposed, small bubbles are formed in the channels which make the pressure drop measurements inaccurate. This shows itself with sharp fluctuations in pressure drop readings as bubbles form and detach from the walls. Hence, the limitation regarding the heat flux dictates the accuracy of heat transfer coefficient. At the same time, for the cases with highly modulated walls due to better

mixing, subcooled boiling occurred at relatively higher values of heat flux and this made the measured values for heat transfer coefficients more accurate. Maximum uncertainty for *Nu* is around 16%, as seen in Appendix A.

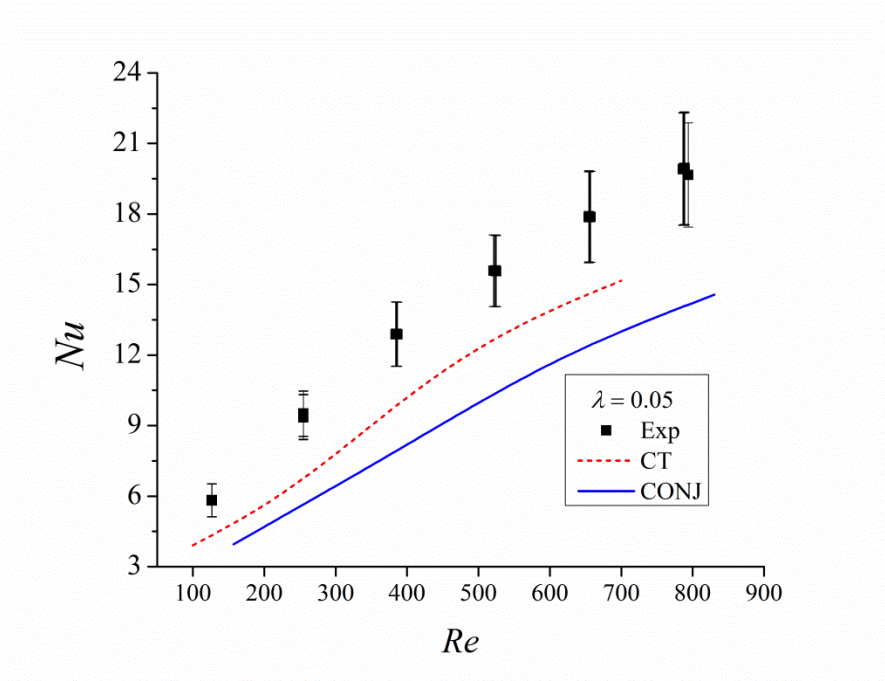

Figure 6-8. *Nu* as a function of *Re* for the slightly modulated case, λ = 0.05.

In order to explain the thermal performance of the case with λ = 0.05, it is needed to recall the three flow mechanisms that affect the heat transfer in converging-diverging microchannels addressed in previous chapters. From Section 4.4.2 it was observed that chaotic advection is present for all the cases while it will be stronger at higher *Re* or larger wall waviness. From Figure 6-11 it is obvious that at *Re* = 200 there is a strong chaotic advection regime for the case with λ = 0.10 while the case with λ = 0.05 is showing a weaker chaotic advection. However, at *Re* = 700 the slightly modulated configuration is also showing strong mixing. Considering this and the fact that counter rotating vortices in the trough region is much weaker for the slightly modulated case, it can be stated that the slightly modulated channels are optimum designs at higher *Re* as

they show superior thermal performance and as it will be shown later, they even have lower pressure drop tradeoff.

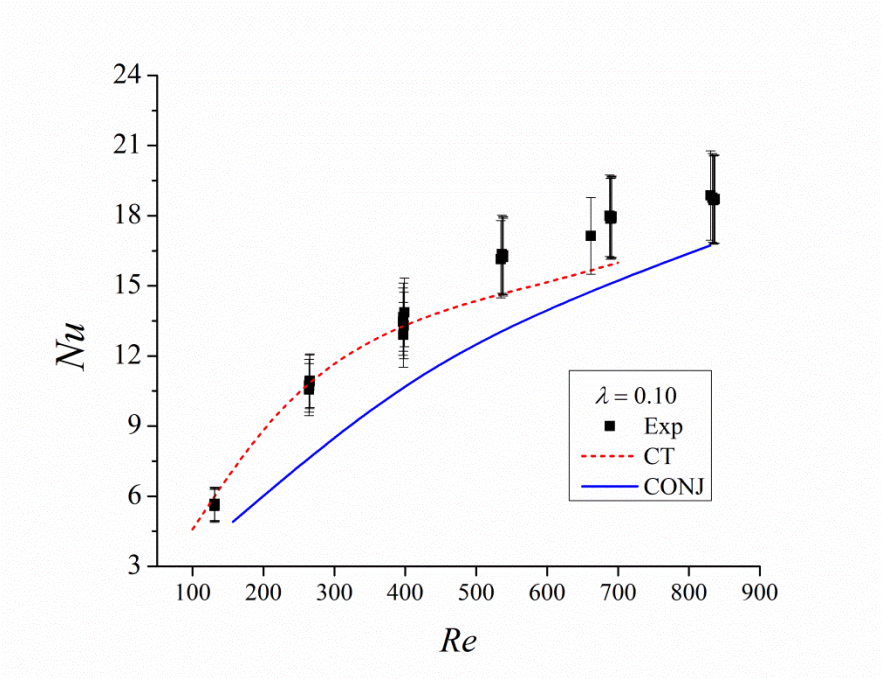

Figure 6-9. *Nu* as a function of *Re* for the moderately modulated case, λ = 0.10.

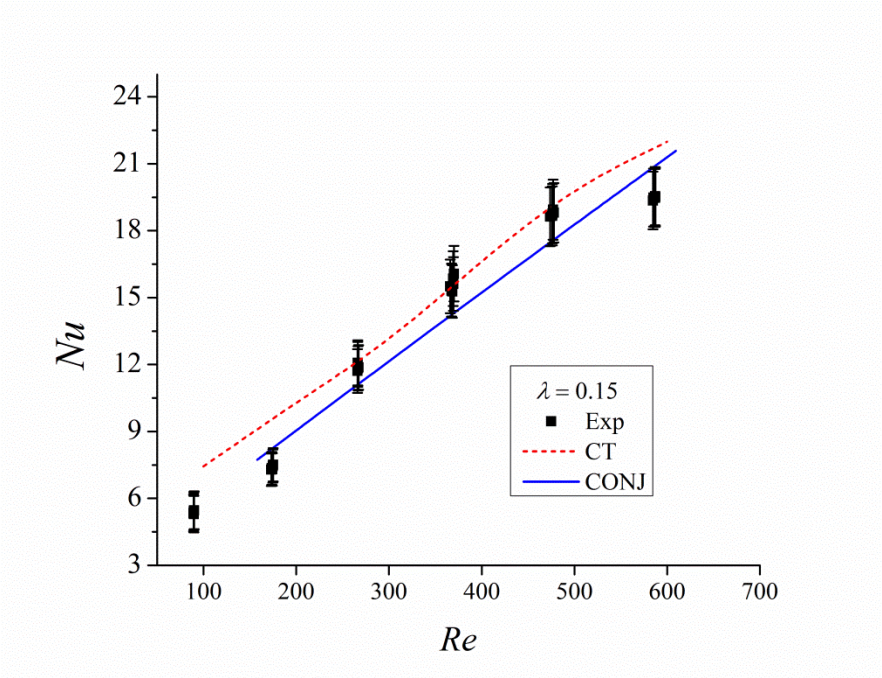

Figure 6-10. *Nu* as a function of *Re* for the highly modulated case, λ = 0.15.

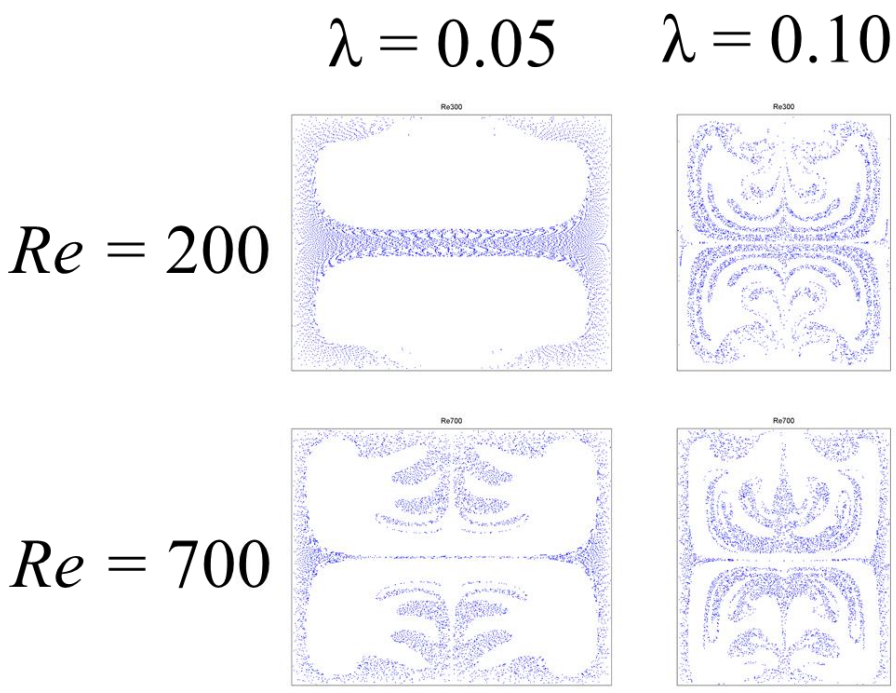

Figure 6-11. Poincaré sections for the cases with λ = 0.05 and λ = 0.10 at *Re* =200 and 700.

6.4.2. Hydraulic performance

Figure 6-12 to 6-15 depict the values for friction factor as the function of wall waviness and *Re*. From the results presented, it is observed that a computational domain consisting of a single channel with constant temperature boundary condition can predict the friction factor very well. However, for highly modulated case, Figure 6-15, experimented pressure drops show large deviation from the numerical results. Based on the results presented for *Nu* and *f*, it can be suggested that a single domain with constant temperature boundary condition is relatively a good representative of the system and it can be used to optimize micro structure shapes for single phase liquid cooling heat sinks.

Pressure reading uncertainty reduces with *Re* which is anticipated considering the fact that pressure drop value increases with *Re*. Maximum uncertainty in pressure reading occurs at smaller *Re* and it is around 20%, Appendix A represents the standard error analysis of the data presented.

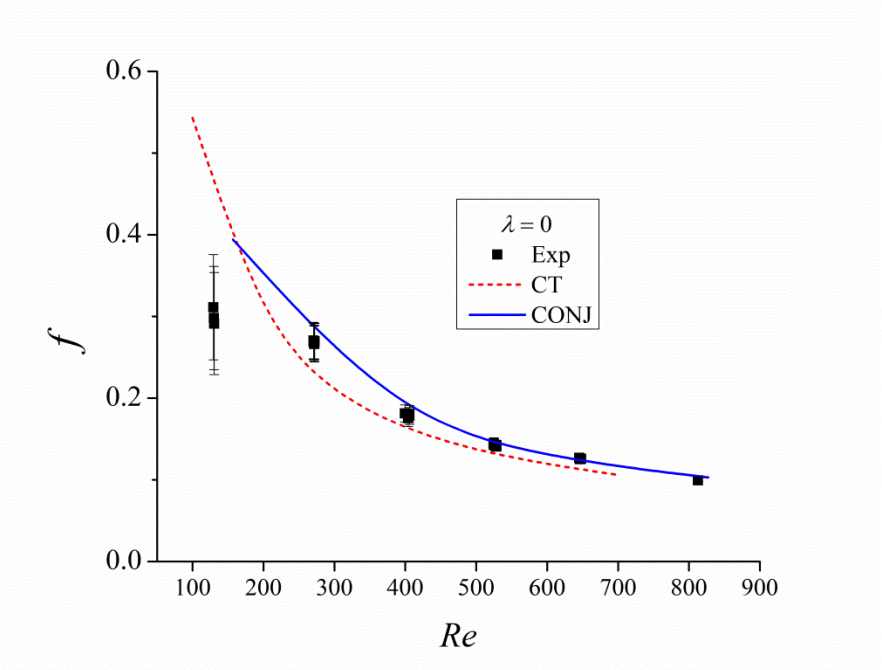

Figure 6-12. *f* as a function of *Re* for straight microchannel, $\lambda = 0$.

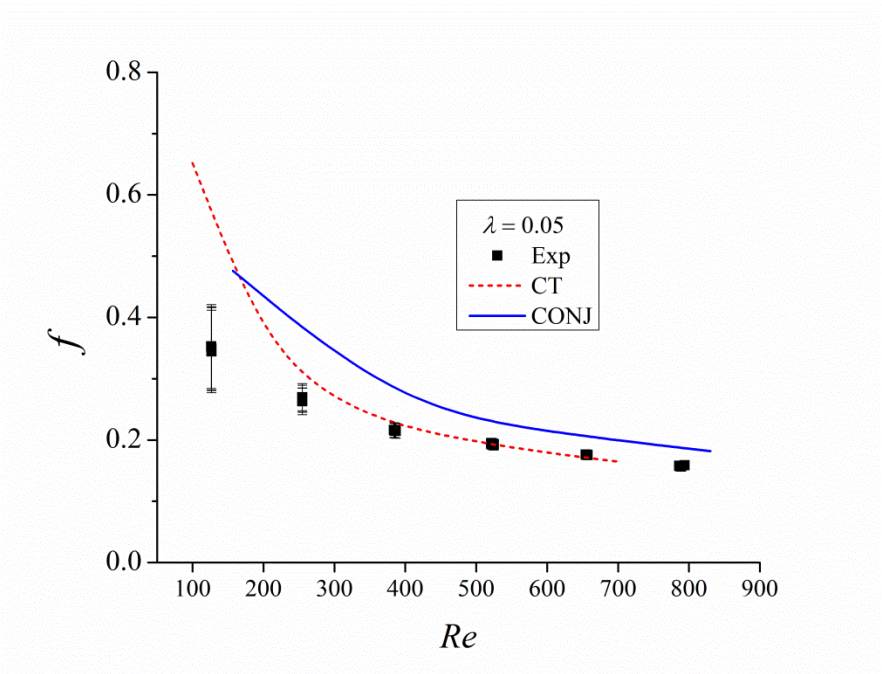

Figure 6-13. *f* as a function of *Re* for the slightly modulated case, λ = 0.05.

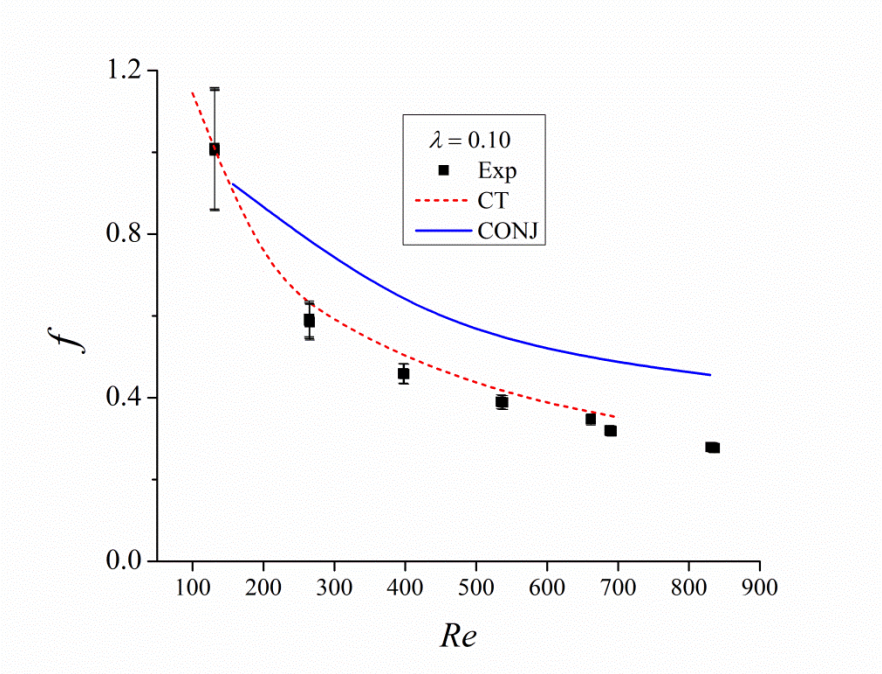

Figure 6-14. *f* as a function of *Re* for the moderately modulated case, λ = 0.10.

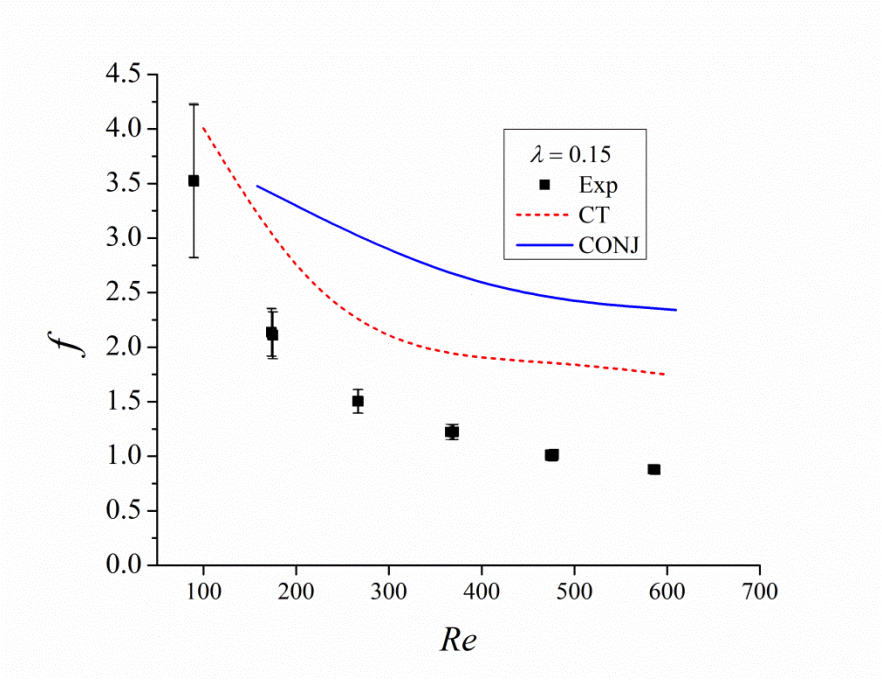

Figure 6-15. *f* as a function of *Re* for the highly modulated case, λ = 0.15.

6.4.3. Heat fluxes range

By considering the definition provided for heat flux by Equation 6-6, and also the pumping power formula:

$$PP = \dot{V}\Delta P \tag{6-14}$$

It is of interest to gain some idea of the heat fluxes being dissipated by each configuration.

In order to show the potential of such a design to be used for electronics cooling application, Figure 6-16 provides the range of heat fluxes being dissipated with these microchannel heat sinks as a function of pumping power. It should be noted that this figure does not provide any comparable performance data considering the fact that the imposed heat flux can be dissipated by any volumetric flow rate and as the result any pumping power. Indeed, for the results to be comparable, it is needed to keep two of the

variables, like mass flow rate and inlet temperature, constant. It should be noted that the data provided in Figure 6-16 are captured by making sure that sub-cooled boiling has not yet happened in the microchannels.

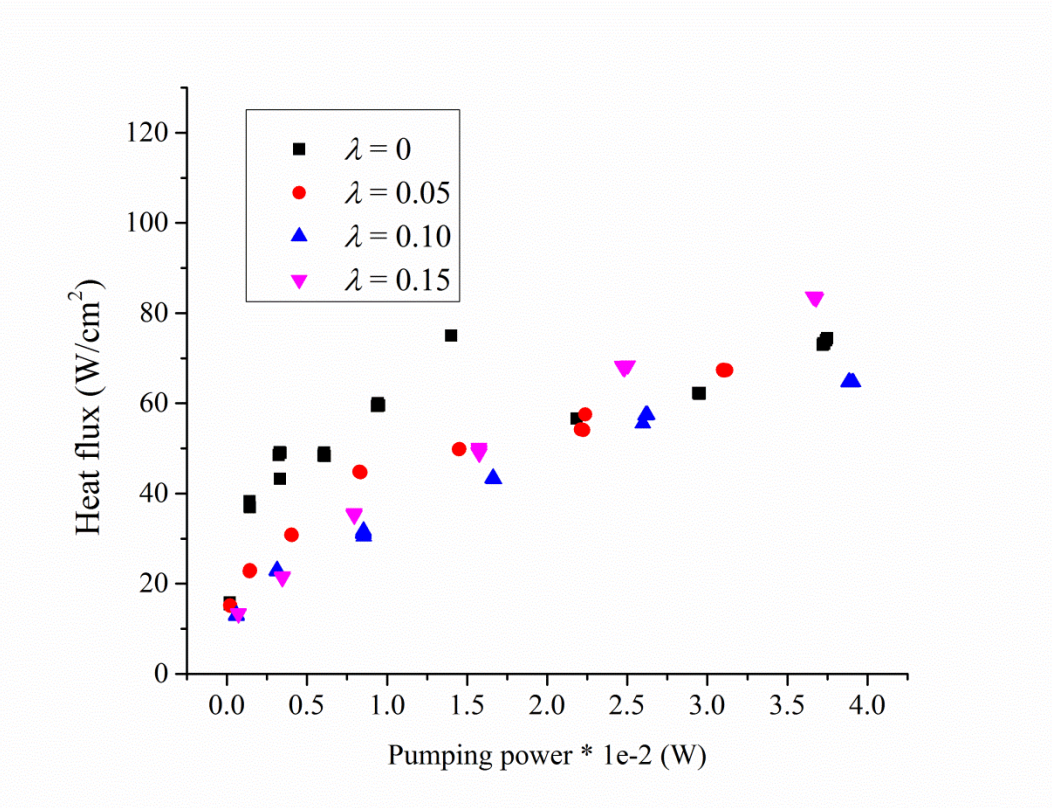

Figure 6-16. Dissipated Heat flux as a function of pumping power. T_{in} = 20°C.

6.5. Conclusion

In this chapter experimental investigation on hydro-thermal performance of wavy walled microchannels is presented. Results of numerical investigation with two different computational domains, i.e. single channel fluid domain with constant temperature boundary condition and conjugated domain with symmetrical boundary condition, are also provided and the experimental results are compared with them. The results obtained for heat transfer coefficient *Nu* and the friction factor *f* shows that the computational domain consisting of a single channel fluid domain with constant temperature can predict

the hydro-thermal performance to a good extend however there was an under-prediction regarding the *Nu* for slightly modulated cases. The results show that slightly modulated cases can be introduced as the superior designs especially at higher *Re* as they show both strong chaotic advection regime and lower pressure drop penalty compared to highly modulated cases.

Related publications

- **H. Ghaedamini, P. S. Lee, and C. J. Teo. "Experimental investigation of single phase forced convection in wavy walled microchannels". In preparation**

Chapter 7. Enhanced transport phenomenon in small scales using chaotic advection near resonance

7.1. Introduction

In previous chapters, single phase flow in wavy walled microchannels under steady flow condition was studied numerically and experimentally. It was found that there is a direct relation between the strength of the chaotic advection in the system and the thermal performance of the channel. On the other hand, it was observed that strong chaotic advection can be attained for higher *Re* and also highly modulated channels. This indeed causes the pressure drop to be highly significant and hence finding ways to elicit chaotic advection with less pressure drop penalty is of interest.

Achieving high levels of chaotic advection or even chaotic flow at smaller *Re* and also for slightly modulated channels is possible with methods like viscoelastic chaos or electromagnetic manipulation of the flow in the channel. The concept of using viscoelastic fluids in wavy walled microchannels is introduced by Burghelea et al. [111]. With this method, chaotic flow and not just chaotic advection could be achieved at relatively smaller *Re*. However, particle aggregation makes this method less attractive.

Studies by Aref [57] showed that in order to have chaotic advection, it is not necessary to have a chaotic velocity field, i.e. Eulerian chaos or turbulence, and even well-defined velocity fields which are time variant may create chaotic trajectories. In this chapter, the effect of pulsatile flow in modulated channels is investigated. We believe that using this method, at smaller mean Reynolds numbers at which chaotic advection is not present for an otherwise steady flow, it is possible to attain chaotic advection and large heat transfer enhancements may be realized. Hence, heat transfer augmentation in slightly modulated converging-diverging microchannels under pulsating flow condition is numerically investigated in this chapter. Effects of flow pulsation, mean Reynolds number and

pulsation frequency are studied and results are presented by comparing the pulsating flow condition with the otherwise steady state case. For the cases tested, it was observed that flow pulsation can greatly enhance heat transfer in slightly modulated channels while pressure drop was maintained at a reasonable level. It is also observed that there exists a characteristic frequency at which resonance takes place making heat transfer to be maximum. From a dynamical systems point of view, the presence of chaos near resonance can be a reason for the enhancement observed. It is also observed that the characteristic frequency value increases by increasing the mean flow *Re*. Proposed enhancement technique showed its superiority at higher Reynolds numbers with enhancements up to 70% for *Re* = 300 and 120% for *Re* = 700.

7.2. Geometry and cases simulated

In Chapter 3 the geometry and the geometrical parameters of a converging-diverging microchannel are presented. Since the parametric space of this study can be very vast considering the geometry and flow variations, the data for one set of geometry with slightly modulated walls are obtained. Moreover, due to the fact that simulating a full 3D model under pulsatile flow and for the whole parametric space is enormously time consuming and considering the available computational facilities, a 2D model is used for this investigation. Furthermore, as studied by Guzman and Amon [67], during the early stages of transition to chaos, 2D and 3D models exhibit similar behavior. Since the Reynolds numbers *Re* for the cases tested in the pulsatile flow regime are smaller than the first critical *Re* at which transition to periodic flow takes place, we are relatively confident that the 2D model represents the 3D physical system to a good extent.

Figure 3-6 represents the computational domains being used in this investigation. For the first part of the study, a single channel fluid domain model under pulsatile flow regime is considered while in the second part of the study, a 2D conjugated model is considered for

pulsatile regime. Water with constant properties, as tabulated in Table 7-1, enters the microchannel at 300 K and gains heat from the side walls. The walls of the microchannel are modulated slightly with the following dimensions:

- *A*, amplitude of the wavy wall, 125 μm
- *a*, averaged channel width, 1000 μm
- *L*, wavelength of the wavy wall, 2500 μm
- *N*, number of furrows, 12

As it was mentioned, the geometry is fixed for the current study while flow parameters are changing. The geometry studied has a waviness of λ = 0.05 with an expansion factor of γ = 2.33 while the channel consists of 12 furrows. It should be noted that the equivalent straight microchannel of the present design has a width of *a*.

Table 7-1. Thermo physical properties of water.

Density (Kg/m^3) ρ	997
Thermal conductivity (W/m K) k	0.6069
Specific heat capacity (J/Kg K) C_p	4181.7
Dynamic viscosity (Pa s) μ	8.899e-4

7.3. Mathematical formulation and numerical procedure

For 2D, incompressible, transient flow with constant fluid properties, the three conservation equations are the ones presented in Section 3.3. Inlet boundary condition is set to be a fluctuating uniform velocity profile with a constant temperature of 300 K. The temporal evolution of the velocity at the inlet is:

$$U = U_0 + U_P \sin(2\pi f_p t) \tag{7-1}$$

where f_p is the pulsation frequency and U_0 is the mean velocity at the inlet and it is chosen in such a way that it satisfies the required Reynolds number as:

$$Re = \frac{\rho U_m D_h}{\mu} \tag{7-2}$$

where U_m is the mean velocity of the equivalent straight microchannel and D_h is the hydraulic diameter for the equivalent straight microchannel which in our case is the hydraulic diameter for parallel plates, $D_h = 2a$. For a given *Re*, U_m and U_0 are related via $U_0 = aU_m/(a-2A)$ so as to achieve the same volume flow rate between the wavy and equivalent straight microchannel.

U_p corresponds to the amplitude of the inlet velocity fluctuation and it is defined based on the pulsation amplitude parameter, Re_P/Re_0.

Atmospheric pressure is set at the outlet and the side walls are set at constant temperature of 350 K with no slip condition while for the conjugated cases, constant heat flux is applied at the outer walls of the copper solid domain.

For each *Re*, one steady state case is computed using constant velocity boundary condition at the inlet, U_0, which was subsequently employed as the initial condition for the transient simulations. Moreover, the results of these steady state cases were also used for comparison against the pulsatile flow regime.

The governing equations are solved numerically using a commercial package, CFX 14.5, which uses the finite volume method. Double-precision numerical simulations are performed while the discretization accuracy is of second order both spatially and temporally. GAMBIT is used to generate the mesh which was made by invoking the mapped scheme, as shown in Figure 7-1. Grid independence study was performed for the

steady state case to define the best spatial discretization size. The results of the grid study for Nusselt number are presented in Table 7-2 where the second mesh was chosen. Afterwards, temporal grid independence study was performed to define the best time step. In this regard, time step Δt was chosen to be a fraction of the forced oscillation period τ, $\Delta t = \tau / N_t$. Two cases with frequencies of 30 Hz and 70 Hz were tested and it was observed that a time step size of $\tau/40$ was capable of predicting the Nusselt number temporal evolution independent of the time step size, Figure 7-2.

Validity of the numerical procedure is proven by performing a comparison between the numerical results and analytical results for the simple case of the straight microchannels. Moreover, the numerical procedure invoked has successfully been used previously in published studies [23, 64, 65, 102].

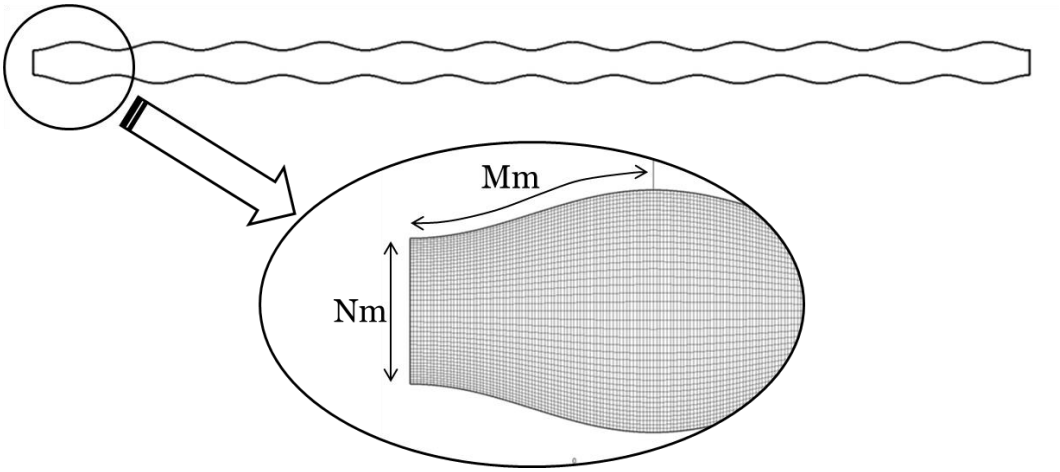

Figure 7-1. Grids being used for the pulsatile flow in wavy walled microchannel study.

Table 7-2. Grid independence study results.

Mm*Nm	Nu	Difference (%)
70*40		
70*70	9.104	0.08
70*100	9.116	0.21
70*140	9.122	0.27

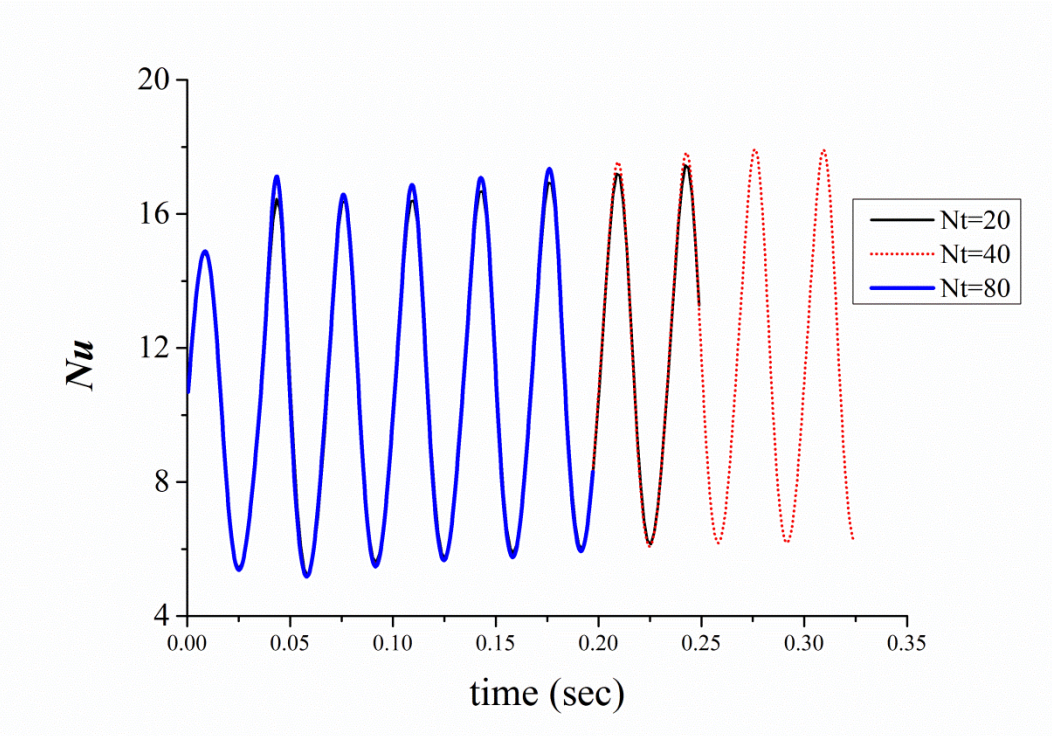

Figure 7-2. Temporal grid independence study.

The first part of the current study tends to examine the flow parameters' effect on heat transfer and flow characteristics of modulated microchannels. Thus, attempts are made to elucidate the effects of *Re*, flow pulsation amplitude, Re_P/Re_0, and pulsation frequency, f_P. For this study, the three Reynolds numbers that are tested are 100, 300 and 700, where *Re* has been previously defined in Equation 7-2. Flow pulsation is carried out for three different amplitudes, i.e. Re_P/Re_0 = 10%, 40% and 70%. The three frequencies which are tested for each case are 5 Hz, 40 Hz and 100 Hz. Table 7-3 provides a summary of the cases simulated, amounting to a total of 27 cases.

Based on the results of the first study, the second part of the study is performed by considering a conjugated domain and keeping the *Re* constant. Three pulsation amplitudes are studied, Re_P/Re_0 = 0.13, 0.4, 0.7, while for each amplitude the range of

pulsation frequencies varies from 10 Hz to 65 Hz. In this way, 36 cases are simulated and the results are time averaged after temporally periodic solution is attained which was after 15,000 to 20,000 time-steps depending on the individual simulation. With a single CPU (2 GHz) allocated, it took about 2 weeks to solve one case. Table 7-4 shows the cases simulated.

Table 7-3. Fluid flow parameters for the cases studied in the first part.

Re	100/300/700		
Re_P/Re_0	10%	40%	70%
frequency (*Hz*)	5/40/100		

Table 7-4. Fluid flow parameters for the cases studied in the second part.

Re	300		
Re_P/Re_0	13%	40%	70%
frequency (*Hz*)	10/15/20/25/30/35/40/45/50/55/60/65		

The heat transfer is quantified by the Nusselt number whose instantaneous value is given as:

$$Nu = \frac{hD_h}{k} \tag{7-3}$$

where D_h is the hydraulic diameter of the equivalent straight microchannel and h is the convective heat transfer coefficient:

$$h = \frac{Q}{A_{HT} \times \Delta T_{lm}} \tag{7-4}$$

where ΔT_{lm} is the log mean temperature difference which is the appropriate average of the temperature difference over the microchannel length [112].

$$\Delta T_{lm} = \frac{\Delta T_{in} - \Delta T_{out}}{\ln\left(\frac{\Delta T_{in}}{\Delta T_{out}}\right)} \tag{7-4}$$

$$\Delta T_{in} = T_w - T_{in} \; ; \; \Delta T_{out} = T_w - T_{out} \tag{7-5}$$

where T_{in} and T_{out} are mass flow averaged mean temperatures at inlet and outlet with the definitions previously presented in Equation 4-5.

Q is the heat transferred to the working fluid. There are two ways of determining Q:

- The first approach involves considering the heat transfer surface:

$$Q_1 = \int_{A_{HT}} q'' dA \tag{7-6}$$

where q'' is the local heat flux.

- The second approach considers the enthalpy change of the coolant passing through the channel:

$$Q_2 = \dot{m} C_p \left(T_{out} - T_{in}\right) \tag{7-7}$$

It should be noted that for a transient system, at any given instant $Q_1 \neq Q_2$, but since Q_2 is more easily quantified during experiments, coupled with the fact that time averaging will cancel out the differences (less than 0.2% difference was observed), the latter definition for Q is used to calculate the convective heat transfer coefficient.

Time-averaged Nusselt number $\overline{Nu}$ is evaluated based on the results after the temporally periodic solution has been obtained.

The difference between the time-averaged Nusselt number $\overline{Nu}$ corresponding to the transient simulations and the steady state Nusselt number Nu_{ss} corresponding to the steady-state simulations are quantified as:

$$\Delta Nu = \frac{\overline{Nu} - Nu_{ss}}{Nu_{ss}} \tag{7-8}$$

Instantaneous friction factor is calculated based on the area-averaged wall shear stress τ_w:

$$f = \frac{\tau_w}{0.5\rho U_m^2} \tag{7-9}$$

where U_m is the average velocity of the equivalent straight microchannel. Similar to Nusselt number, time averaged friction factor $\overline{f}$ is obtained after the temporally periodic solution has been obtained and then the friction factor variation is defined as:

$$\Delta f = \frac{\overline{f} - f_{ss}}{f_{ss}} \tag{7-10}$$

For the conjugated test, Nu is calculated by using the heat transfer coefficient h defined by:

$$h = \frac{Q}{A_{HT} \times (T_w - T_b)} \tag{7-11}$$

where Q is the input heat at the solid domain walls and T_w is the area averaged temperature of the microchannel wall and T_b is the volume averaged temperature of the fluid domain.

Friction factor however is calculated by considering the Equation 7-9.

7.4. Results and discussion

7.4.1. Overall Thermal-Hydraulic Performance

Figure 7-3 shows the Nusselt number variation as a function of frequency and different fluctuation amplitudes. Data are provided by dash lines since the interval points regarding the frequency are not sufficient to present the actual trend. It is seen that there is a large increment in heat transfer at certain frequencies and for the mean Reynolds number of 300, a peak occurs at approximately 40 Hz for the heat transfer. This indicates the presence of an optimum point for which Nusselt number is a maximum and this point should be in the vicinity of 40 Hz. The trend in the graph shows that increasing the frequency further has resulted in a decrement in *Nu*. In the following sections, the observed behavior is explained.

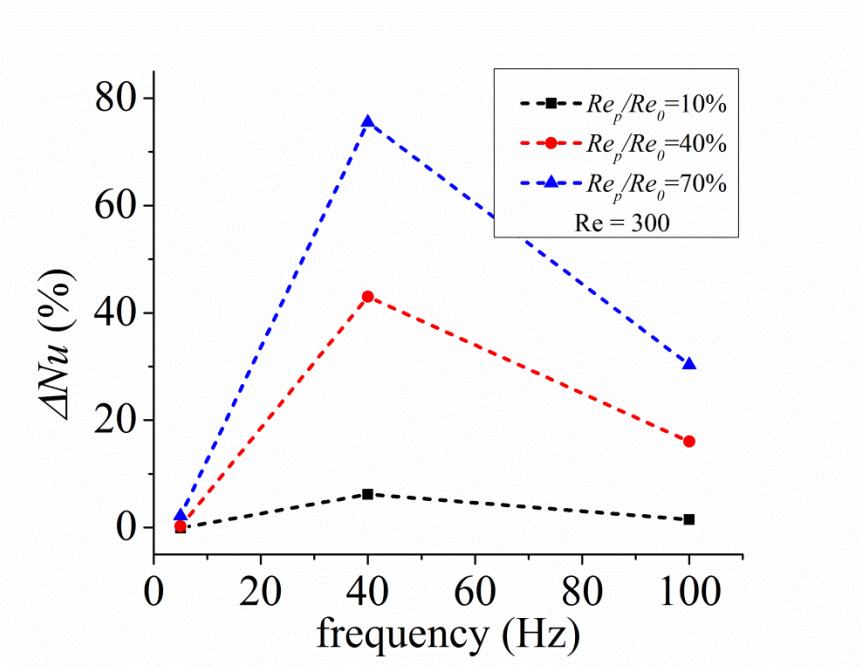

Figure 7-3. Nusselt number variation as a function of pulsation frequency and pulsation amplitude for *Re* = 300.

It is of interest to examine the penalty for this superior thermal performance. Figure 7-4 shows the friction factor increment as a function of pulsation frequency and amplitude. It is seen that increasing both the frequency and amplitude has resulted in an increment in frictional losses. Comparing Figures 7-3 and 4 reveals that for some cases, the increment in heat transfer exceeds the frictional penalty and thus rendering this technique attractive. The data presented in Figures 7-3 and 4 are tabulated in Table 7-5. It can be seen that for amplitudes of 10% and 40% and a frequency of 40 Hz, *Nu* increment is higher than the frictional loss penalty.

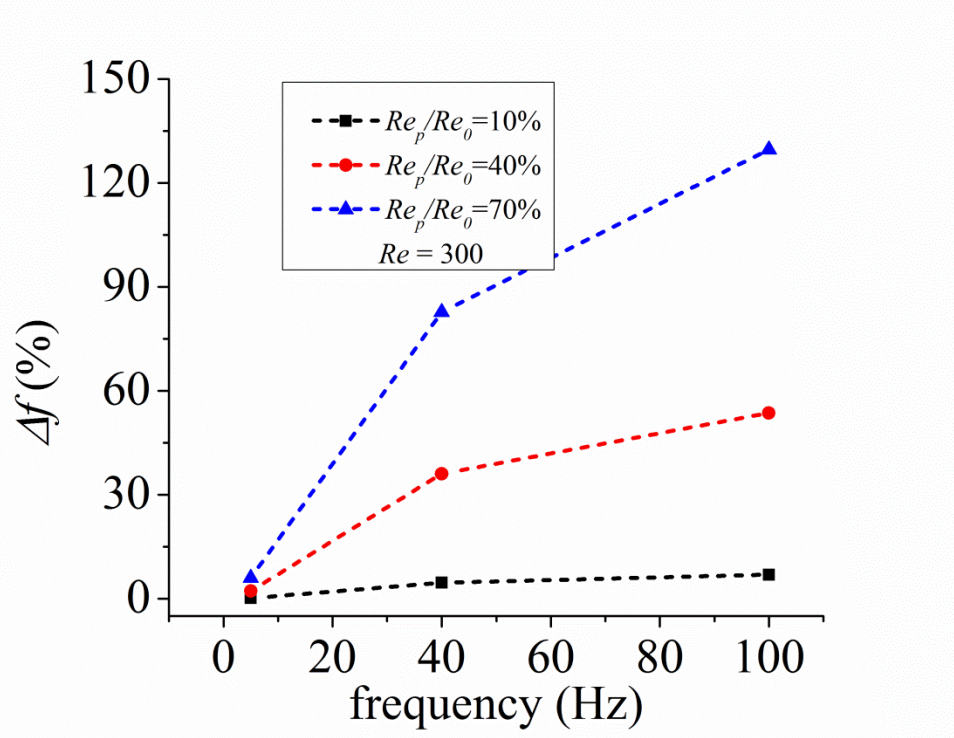

Figure 7-4. Friction factor variation as a function of pulsation frequency and pulsation amplitude for *Re* = 300.

Table 7-5. Nusselt number and friction factor for the cases with *Re* = 300.

	Re_p/Re_0=10%		Re_p/Re_0=40%		Re_p/Re_0=70%	
Frequency (*Hz*)	ΔNu	Δf	ΔNu	Δf	ΔNu	Δf
5	-0.1%	0.2%	0.2%	2.2%	2.2%	6.0%
40	6.2%	4.6%	43.0%	36.0%	75.5%	82.8%
100	1.5%	6.9%	16.0%	53.6%	30.3%	129.6%

7.4.2. Local performance

In order to understand the underlying heat transfer enhancement mechanisms, it is necessary to look into the microchannel flow locally. For the sake of explaining the behavior of the flow in the channel and without loss of generality, results of Rep/Re_0 = 40% for *Re* = 300 will be closely examined here. Figure 7-5 represents the temporal variation of instantaneous spatial averaged Nusselt number and friction factor for three different frequencies. The corresponding steady state value is also shown as a dash-dot line in this graph. For smaller frequencies, i.e. 5 Hz, the flow shows a quasi-steady behavior with spatial averaged *Nu* fluctuating around a mean value close to the steady state value. At frequency of 40 Hz, the temporal variation in *Nu* is increased in mean value and relative amplitude however for frequency of 100 Hz both mean value and amplitude of instantaneous *Nu* are less than 40 Hz. For friction factor on the other hand, increasing the frequency has resulted in increment of mean value and amplitude of the resulting instantaneous frictional loss.

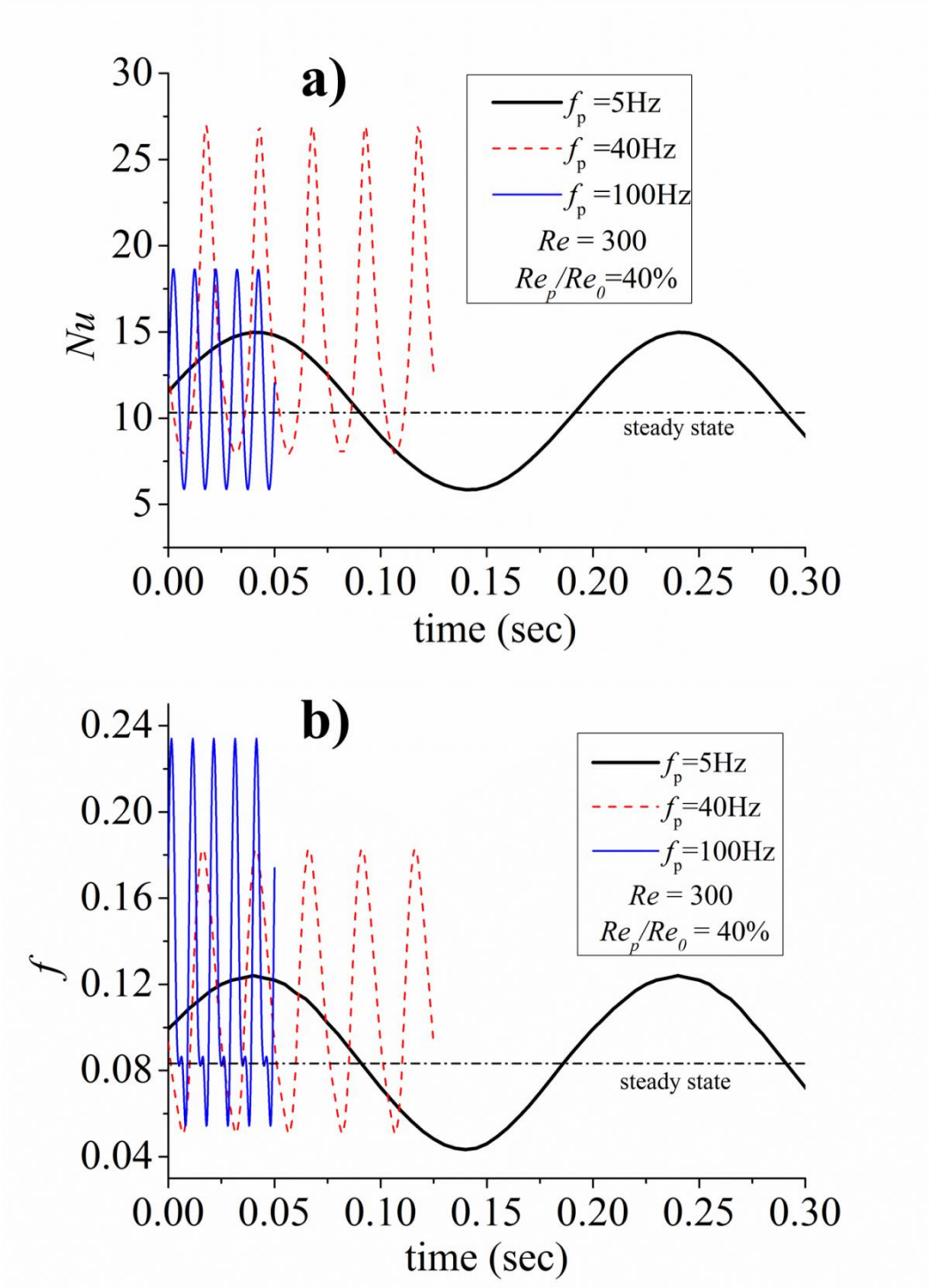

Figure 7-5. Temporal value of (a) Nusselt number and (b) friction factor for the cases with *Re* = 300 and 40% pulsation amplitude.

Based on the inlet condition, there are two phases for the mean flow velocity, namely deceleration phase ($0 < t < \tau / 2$) and acceleration phase ($\tau / 2 < t < \tau$), Figure 7-6. It is obvious that presenting the results for every furrow will culminate in an extremely lengthy discussion hence, local temperature distribution which is depicted in Figure 7-6 shows the evolution of temperature contour for furrow #6 of the channel (just one out of 12 furrows). The two cases shown are representative of the 40Hz and 100Hz pulsation frequencies. From Figure 7-6, in the acceleration phase, hot recirculating areas will be created in the trough region and in the deceleration phase, this vortex detaches from the expanding area and travels with the bulk flow. Comparing this situation with the steady flow, we can understand the reason for superior performance of such designs under pulsatile flow regime. For the steady state case as it was discussed in previous chapters, the recirculating area remains intact, reducing the effective heat transfer area, thus having an adverse effect on the heat transfer [102]. For larger frequencies (i.e. 100 Hz) we see less interactions between the core fluid and the eddies formed in the trough region and that can be a reason for less pronounced heat transfer enhancement.

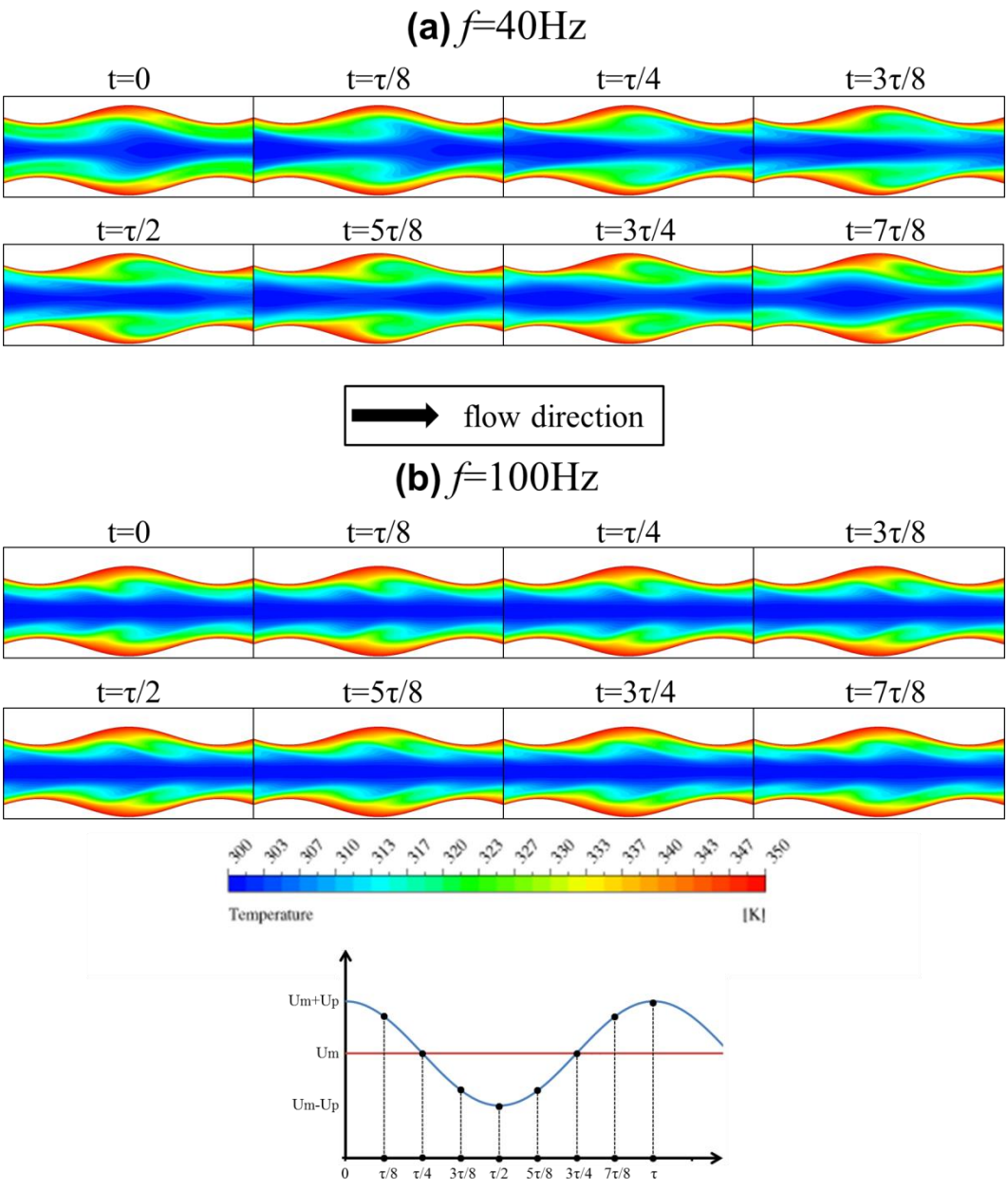

Figure 7-6. Temperature contours of furrow #6 of the channel at different time intervals for *Re* = 300 and 40% pulsation amplitude for two frequencies of (a) 40Hz and (b) 100Hz.

Due to hot spot issues, there is a concern that there may be a situation for which local performance of the pulsatile flow is inferior to that for the steady state case, although the overall performance may be higher. For this reason, locally temporal and spatial averaged *Nu* is computed for each furrow along the channel. Nusselt number for steady state case

is also calculated and presented in Figure 7-7. It is observed that for all the cases the performance under transient condition is locally superior compared to that for the steady state case. Referring to Figure 7-7, one interesting observation is that the individual plots corresponding to the pulsatile flow exhibit similar trends and local behavior to the steady state case. This indicates at each pulsatile frequency, similar transient flow structures responsible for the heat transfer augmentation occur in each furrow, thus corroborating with our previous statement that the flow structure in furrow #6 may be a representative of the flow structure through the other furrows and hence the whole channel.

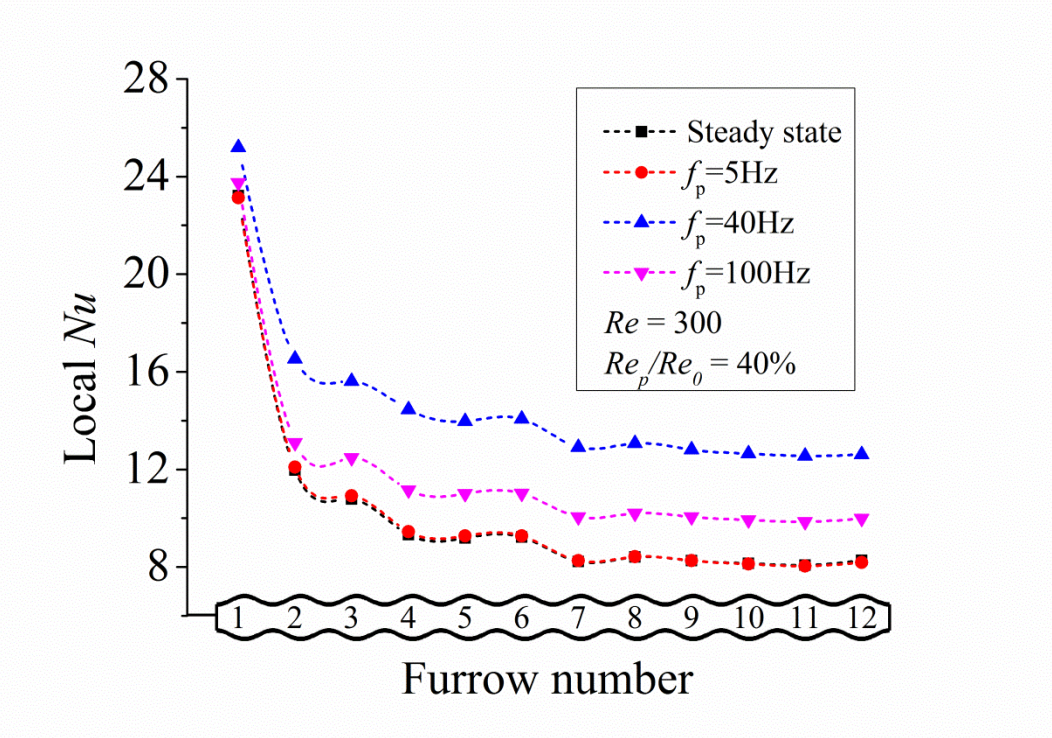

Figure 7-7. Local value of spatially and temporally averaged Nusselt number for the case with *Re* = 300 and pulsation amplitude of 40%.

7.4.3. Chaotic advection in converging-diverging microchannels

Based on the detailed discussion in Section 3.4, Aref [57] established that advection problem from Lagrangian point of view can be reduced to a finite dimension dynamical system and thus there is an analogy between them. Previous investigations on

converging-diverging passages [67, 68] and also the results presented at Section 4.4.4 showed that there is a transition to Eulerian chaos by increasing the *Re* as the control parameter. However, this transition for slightly modulated channels occurs at relatively higher Reynolds numbers. Moreover, Eulerian chaos is accompanied by high pressure drops due to small scales.

Lagrangian representation of advection problem of a steady, incompressible, 2D flow will result in an integrable system or in other words, a regular advection. On the other hand, making the flow field variant can potentially result in chaotic advection at lower mean Reynolds numbers with smaller pressure drop penalties. Thus, enhanced transport phenomena as manifested by enhanced *Nu* in Figure 7-3 may be an indicator of chaotic advection. This will be investigated in the next section.

7.4.4. Chaotic advection near resonance

In Section 3.4.5 the definition of Poincaré map and the methods to create it for pulsatile flow are discussed. Figure 7-8 shows the Poincaré map for three pulsation frequencies of 5, 40 and 100 Hz for the case with *Re* = 300 and pulsation amplitude of 40%, corresponding to the data of red line in Figure 7-3. Poincaré maps are created by releasing 4000 massless particles at the start of deceleration phase for mass flow rate in the area of a rectangle placed at furrow #5 and then implementing a fourth-order Runge-Kutta method and utilizing a time varying integration step, calculating the position of those particles as time passes. At certain time intervals, position of those particles is shown in Figure 7-8. Chaotic advection shows itself by a Poincaré map at which particles have a tendency to occupy maximum area of domain. As it can be seen, for the case with 5 Hz, particles tend to travel along a manifold showing itself as a line. However, 40 Hz case shows a behavior best explained by chaotic advection. Particles are traveling with the core flow as well as a nice near wall interaction which shows itself in high Nusselt

number of 40 Hz at Figure 7-3. For the case 100 Hz, particles have minimum near wall interaction but, it can be said that advection is locally chaotic but it does not include the near wall region and hence an inferior heat transfer performance compared to 40 Hz case is achieved.

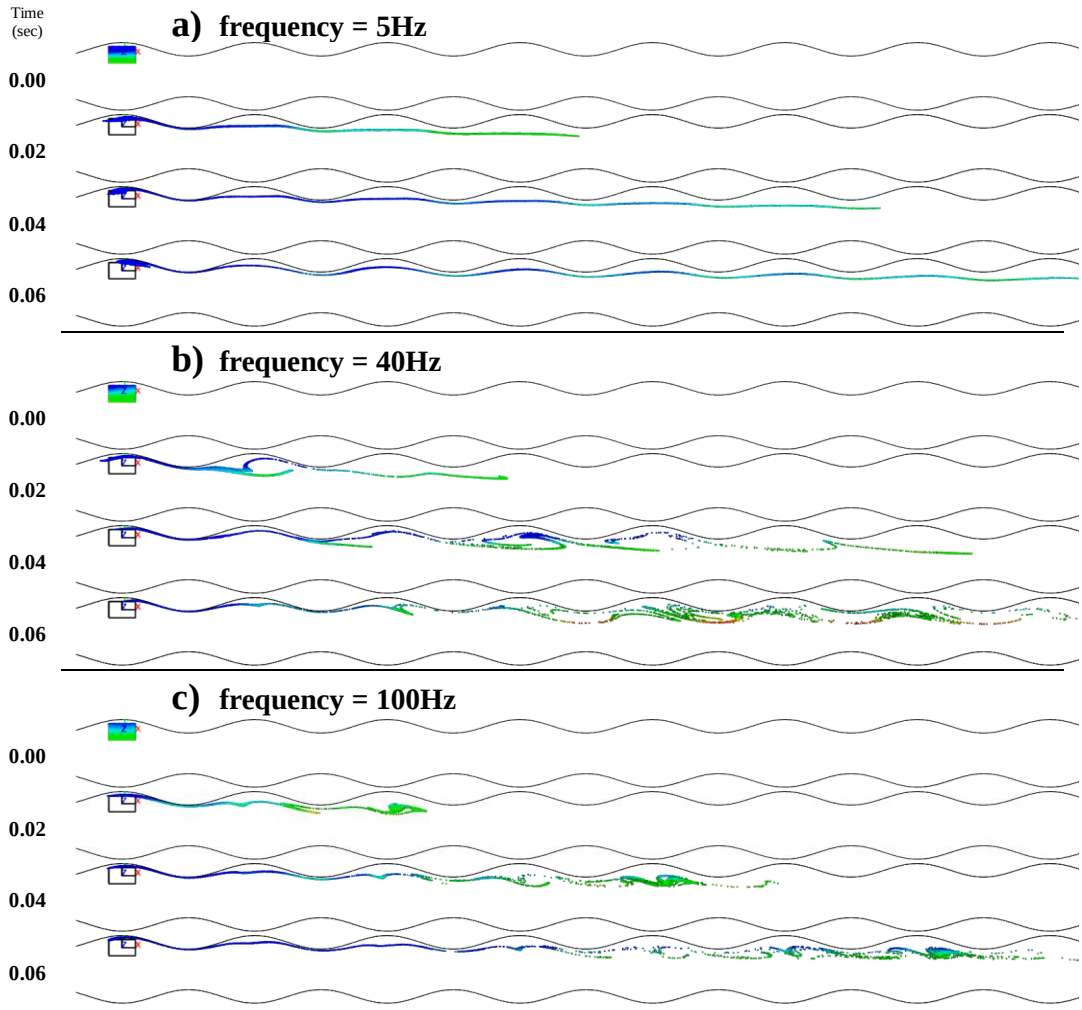

Figure 7-8. Poincaré map at four time intervals for the cases with *Re* = 300, pulsation amplitude of 40% and pulsation frequency of (a) 5 Hz, (b) 40 Hz and (c) 100 Hz.

Superior thermal performance around the characteristic frequency and not at frequencies greater can be due to the phenomenon, *chaotic advection near resonance*. Resonances are regions in the phase space of any dynamical system for which the forcing frequency results in highly complex motions with a profound effect on the dynamics of the system.

It has been relatively well studied that resonance can result in chaotic motions [94], and that may be the main reason for highly enhanced Nusselt number that we are observing near the characteristic frequency.

7.4.5. Effect of Re

Figure 7-9 discloses the Nusselt number variation as a function of frequency and amplitude of inlet velocity. Since the scope of this study is to address the thermal performance of micro/mini channels, Reynolds numbers are chosen in a way that the flow is maintained in the laminar flow regime. It is seen that enhancement is more pronounced for higher Reynolds numbers as we can achieve enhancements up to 120% for Re = 700. As a rule, it is observed that larger amplitudes always result in higher enhancements in Nu for all the cases. However, for frequency, it seems that there is an optimum frequency at which heat transfer performance is maximum. This characteristic frequency is seen to be higher for higher Reynolds numbers. Another remarkable result is that for higher Reynolds numbers, i.e. Re = 700, even a small amplitude pulsation can result in enhancements of up to 30% if it is excited at an appropriate frequency.

Figure 7-9 also shows the effect of flow pulsation on friction factor for the three different Reynolds numbers. It is observed that increase in Re, pulsation amplitude and pulsation frequency result in increment in friction factor. Doing a one to one comparison between the ΔNu and Δf in Figure 7-9 reveals that for Re= 300 and Re = 700, there are cases with heat transfer augmentations being higher than the pressure drop penalty which makes this active method of enhancement appealing.

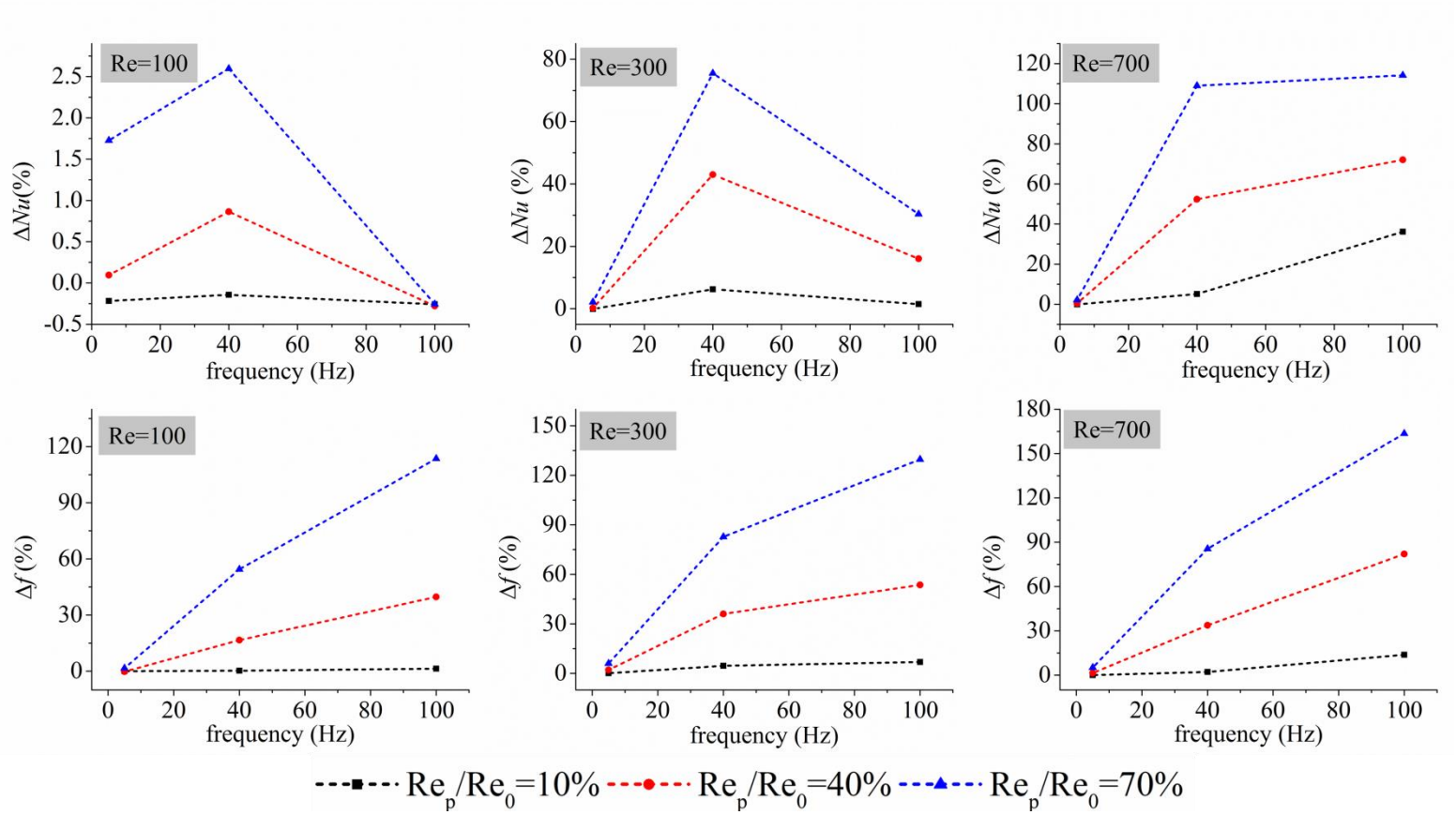

Figure 7-9. Nusselt number and friction factor variation as a function of pulsation frequency and pulsation amplitude for *Re* = 100, 300 and 700.

7.4.6. Effect of conjugated condition

Figure 7-10 depicts Nusselt number, friction factor and maximum temperature in the solid as the function of frequency for the pulsation amplitude of 13%. *Nu* is calculated by using the heat transfer coefficient *h* defined by Equation 7-11. Friction factor is calculated by considering the area averaged shear stress on the microchannel wall and the velocity associated with an equivalent straight microchannel presented in Equation 7-9. The above values are calculated for each time-step and after the periodic results are attained, the results are averaged for the final 12 pulsation periods τ which is equal to 480 time-steps as each pulsation period is 40 time-steps.

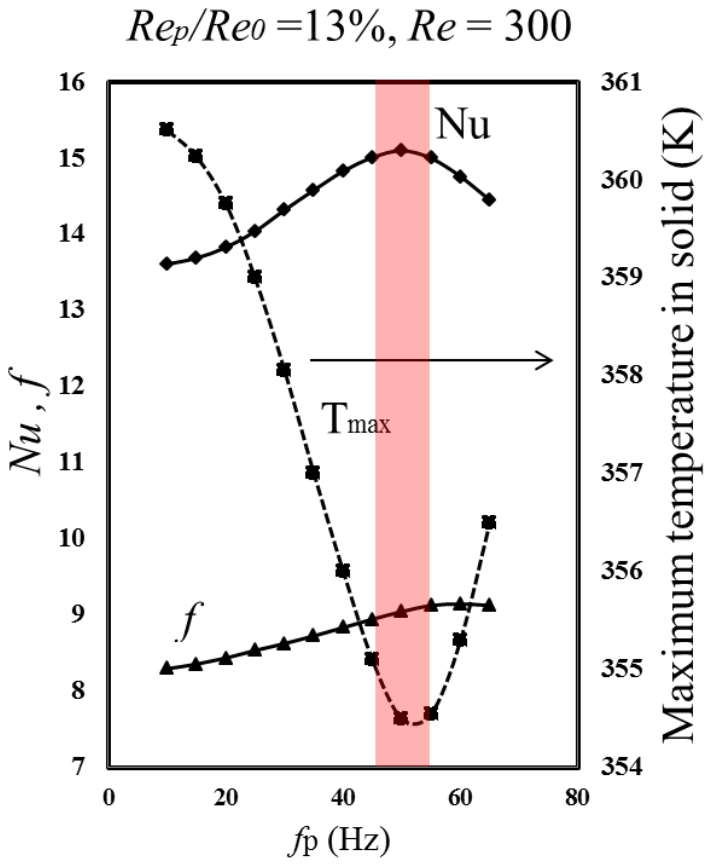

Figure 7-10. Time averaged Nusselt number, friction factor and maximum temperature in the solid as the function of pulsation frequency for the case with 13% pulsation amplitude and *Re* = 300.

Based on Figure 7-10, there is a pulsation frequency at which Nusselt number is maximum while the minimum value of T_{max} is also obtained around that value. Friction factor increases with the frequency of the pulsation up to a certain level and further increase in pulsation frequency causes the friction factor to decline. This observation is reasonable considering the fact that any inertia system has a cut off frequency above which it is not sensitive to oscillation excitation [76].

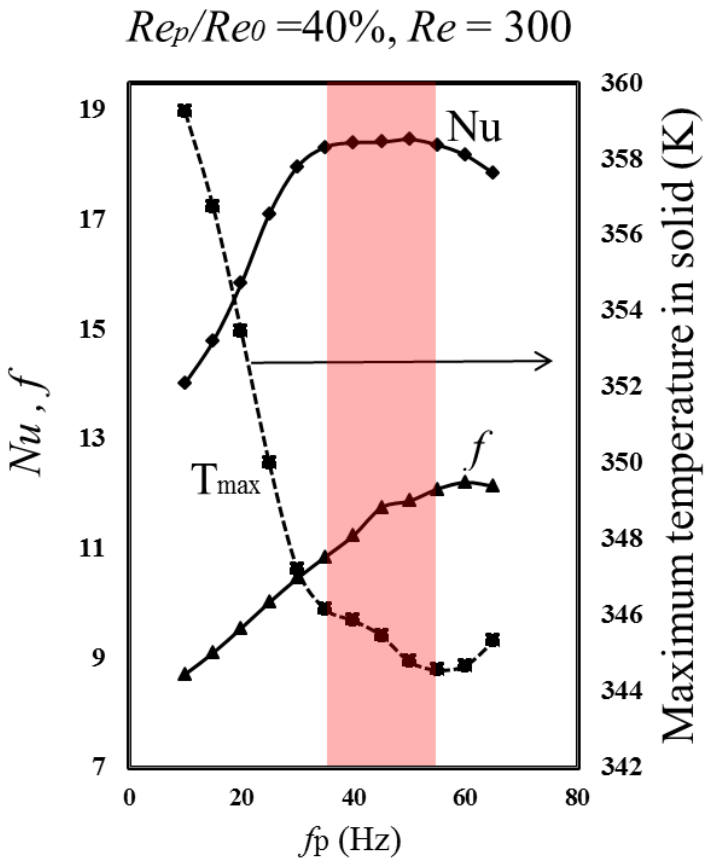

Figure 7-11. Time averaged Nusselt number, friction factor and maximum temperature in the solid as the function of pulsation frequency for the case with 40% pulsation amplitude and *Re* = 300.

Figures 7-11 and 7-12 show the Nusselt number and friction factor for pulsation amplitudes of 40% and 70% respectively. In Figure 7-11, it is seen that the Nusselt number is constant for a larger range of frequencies which shows the robustness of design

for certain amplitudes. However, considering the three figures together, it is clear that the thermally optimum frequency range is at smaller frequencies for larger pulsation amplitudes.

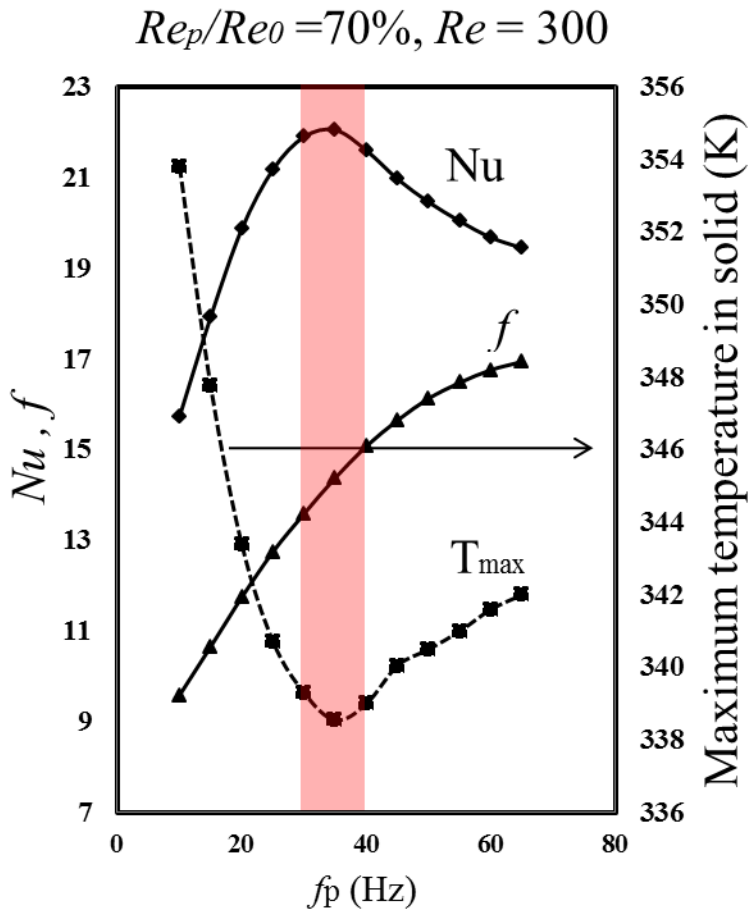

Figure 7-12. Time averaged Nusselt number, friction factor and maximum temperature in the solid as the function of pulsation frequency for the case with 70% pulsation amplitude and *Re* = 300.

As it was discussed in previous sections, considering the peak observed for *Nu* as the function of pulsation frequency, we believe that the enhancement is due to the presence of chaotic advection near resonance. That means that the maximum heat transfer occurring around a certain frequency and that characteristic frequency belongs to the

resonance region of the system. Presence of chaos as the result of resonance is well studied by G. Haller in dissipative as well as Hamiltonian systems [94].

Another observation is the out-of-phase variation of T_{max} and Nu. This is especially noticeable for the case with pulsation amplitude of 40%, i.e. Re_P/Re_0 = 40%. Over-simplification may be the cause of out phase behavior since the definition used for Nu considers the bulk temperature of the fluid and also area averaged temperature of the wall and this may render the definition of Nu not to be conclusive.

Based on the maximum temperature in the solid, a thermal resistance parameter can be suggested as:

$$R = \frac{T_{\max} - T_{in}}{Q} \tag{7-12}$$

Figure 7-13 shows the thermal resistance as a function of pulsation frequency and pulsation amplitude. It is seen that larger pulsation amplitude results in a smaller thermal resistance. Considering the definitions of thermal resistance and friction factor, it is proposed that the following definition for the Figure of merit, *FOM*, be used:

$$FOM = \frac{1}{R \times \overline{f}} \tag{7-13}$$

The proposed *FOM* parameter gives an indication of whether the increment in heat transfer is worth the pressure drop penalty and since the mean value for mass flow rate is kept constant for all the cases, this provides a fair comparison.

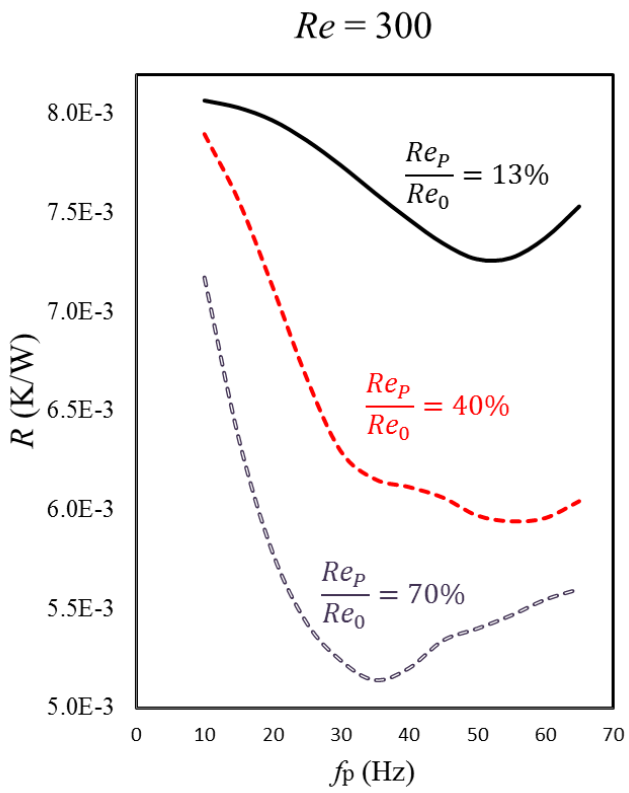

Figure 7-13. Thermal resistance as a function of pulsation frequency and pulsation amplitude.

Figure 7-14 shows the *FOM* as a function of pulsation frequency and pulsation amplitude. As it can be seen, the maximum value for *FOM* migrates to the left for larger pulsation amplitudes. When pulsation amplitude is very large, Re_P/Re_0 = 70%, *FOM* declines drastically with increment in frequency. From designing point of view, one should first determine the amount of enhancement in heat transfer which is needed (Figure 7-13) and then based on the *FOM* (Figure 7-14), operating frequency can be determined.

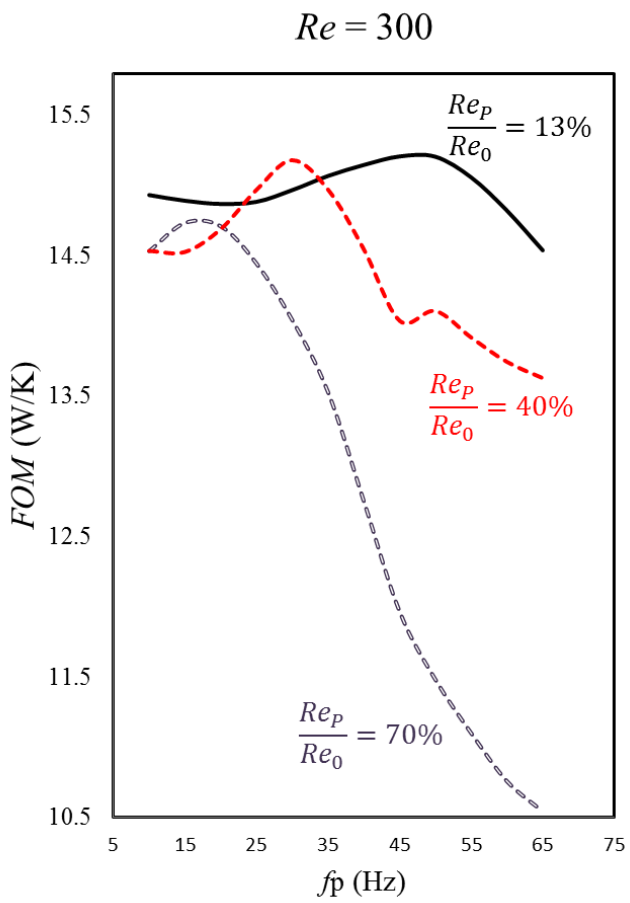

Figure 7-14. Figure of merit as a function of pulsation frequency and pulsation amplitude

7.5. Conclusion

In this chapter, the effect of flow pulsation on heat transfer performance of slightly modulated channels is investigated. Modulated channels are one of the shapes which are proposed by researchers for passive enhancement techniques [113]. At lower *Re*, *Re* = 100, enhancements observed were marginal while the pressure drop penalty was tangibly higher, making the method unattractive. However, for higher *Re*, i.e. *Re* = 300, heat transfer augmentations up to 70% were observed with pressure drop penalties of the same range. Enhancements were even more pronounced for *Re* = 700 with number of cases for

which heat transfer enhancement exceeded pressure drop penalty increased and augmentations up to 120% were observed.

Seeing the effect of pulsation frequency and amplitude while keeping *Re* constant, increasing pulsation amplitude resulted in an increase in both *Nu* and friction factor. However, frequency showed a different behavior. There seems to be a characteristic frequency for each *Re* and pulsation amplitude at which heat transfer is augmented the most. We believe that enhancements observed are the result of chaotic advection in the system and that the characteristic frequency is located in the resonance region of the system.

With a conjugated model, the effect of pulsation frequency and pulsation amplitude at constant mean *Re* was studied in the second part of this chapter for a single configuration with slightly modulated channel. It was observed that for each pulsation amplitude, there is an optimum frequency at which heat transfer is maximum or thermal resistance is minimum. Within the range studied, up to 35% reduction in thermal resistance was observed and it is believed that the enhancement observed is, to some extent, the result of the presence of chaotic advection near resonance.

A figure of merit, *FOM*, is defined in order to assess the effects of heat transfer and pressure drop at the same time. Based on the proposed figure of merit and for the range studied, it was shown that optimum frequency for larger amplitudes happens at smaller frequencies. Moreover, due to the large increment in pressure loss at larger amplitudes and higher frequencies, performance of the channel decreases drastically when the frequency increases.

Related publications

- **H. Ghaedamini, P. S. Lee, and C. J. Teo. "Forced pulsatile flow to provoke chaotic advection in wavy walled microchannel heat sinks." Thermal and Thermomechanical Phenomena in Electronic Systems (ITherm), 2014 IEEE Intersociety Conference on. IEEE, 2014.**
- **H. Ghaedamini, P. S. Lee, and C. J. Teo. "Enhanced transport phenomenon in small scales using chaotic advection near resonance." International Journal of Heat and Mass Transfer 77 (2014): 802-808.**
- **H. Ghaedamini, P. S. Lee, and C. J. Teo. "Pulsatile flow in slightly modulated microchannels." In preparation.**

Chapter 8. Conclusion and recommendations for future works

8.1. Conclusion

Hydro-thermal performance of converging-diverging microchannels to be used in the single phase liquid cooling heat sinks is being studied numerically and experimentally in this thesis. Effect of geometrical parameters and flow parameters are studied and the results are presented in the format of dimensionless parameters as *Nu* and *f*. The terminology of chaotic advection near resonance is introduced for the first time in this thesis although the concept itself is not new. The possibility of using this technique to enhance the transport phenomenon at small scales is investigated and the results showed a good potential for single phase cooling enhancement.

Our numerical results show that the vortical structures at converging-diverging configuration are four streamwise vortices at the corner of the contracting part of the furrow and if the waviness is large enough and *Re* is high enough, there may appear two counter rotating vortices in the trough region. Based on these vortical structures and the concept of chaotic advection, the key mechanisms that affect the heat transfer performance in converging-diverging microchannels are introduced as: heat transfer augmentation due to increment in heat transfer area, heat transfer enhancement due to presence of chaotic advection, and heat transfer decrease due to presence of dead areas as the result of counter rotating vortices in the trough region.

Depending on the level of wall waviness and the value of *Re*, each of above mechanisms can be dominant and an increase or decrease in heat transfer may be observed as the resultant. Pressure drop however is a direct function of wall waviness or channel expansion factor. Based on the results presented in Chapter 4, pressure drop is an

exponential function of channel expansion factor γ and it increases with the wall waviness.

Based on the pressure drop and the heat transfer coefficient, performance factor is being defined which considers the enhancement in both dimensionless parameters *Nu* and *f*. The results for performance factor showed that the cases with slightly modulated walls had better performance. Considering the heat transfer, cases with narrower channels are superior. Hence, for a constant wall waviness condition, cases with larger expansion factor show higher heat transfer rates.

Our experimental results indicate good agreement with the numerical results of a single channel under constant temperature boundary condition. This is due to the fact that the fin efficiency is very high in our study, above 95%. Pressure drop was predicted very well with our code however, for the case with highly modulated walls differences between the numerical and experimental results were observed. Again the experimental results showed that the cases with slightly modulated walls are the best candidates for heat transfer enhancement and especially for higher *Re* where chaotic advection is strong and counter rotating vortices in the trough region are not that strong due to the small waviness.

The study done on pulsatile flow in slightly modulated wavy walled microchannels showed that there is a significant cooling enhancement opportunity regarding this technique. While heat transfer augmentation up to 70% is observed, pressure drop penalty was less than 60% which renders this method attractive. The superiority of this technique showed itself at higher *Re* with heat transfer enhancements up to 120% for some cases.

8.2. Recommendations for future work

Single phase liquid cooling due to its simplicity has the potential to be the De facto of cooling strategy for electronics systems. Our results showed great enhancements which can be achieved with converging-diverging designs and especially at lower wall waviness and higher *Re*. The following can be recommended for future work:

- Experimental investigation of pulsatile flow in wavy walled microchannels. We believe that experiments are needed to further verify the results provided in the last chapter. The main problem for such a study would be the measurement of the mass flow rate. With frequencies as high as 30 Hz, the flow meter should operate with frequencies around 300 Hz, which is extremely fast for a flow meter. An alternative method would be to use the pressure drop parameter as pressure transducers can work with such frequencies.
- A wavy walled microchannel design which not only has wavy side walls but also has wavy structure at the bottom. The effect of these walls on the fluid flow and mixing may lead to interesting results.
- The concept of pulsatile flow in converging-diverging configuration can also be extended to wavy microchannels.
- The transition scenario discussed by Guzman and Amon [66] is for a design with moderately modulated walls. However, the recent paper of Guzman [69], which has considered a 2D model, shows that the transition scenario is highly dependent on the expansion factor. A similar study can be performed to examine this idea for 3D models also.
- Although the depth of the channel is highly restricted by the manufacturability of the channels, but some of our rudimentary results which are not provided in this

thesis show that the Poincaré structure may not show the asymmetry behavior at higher *Re* for some cases with smaller depth. This can be a subject of future studies.

- Based on our numerical results and the comparison with the experiments, it is observed that the single channel with constant temperature boundary condition can predict the hydro-thermal performance to a good extent. This result can be used in optimization algorithms which uses the single channel instead of the conjugated domain.

References

[1] D.B. Tuckerman, R.F.W. Pease, High-Performance Heat Sinking for Vlsi, Electron Devic Lett, 2(5) (1981) 126-129.
[2] V. Venkatadri, B. Sammakia, K. Srihari, D. Santos, A review of recent advances in thermal management in three dimensional chip stacks in electronic systems, J Electron Packaging, 133(4) (2011) 041011.
[3] S. Liu, J. Yang, Z. Gan, X. Luo, Structural optimization of a microjet based cooling system for high power LEDs, Int J Therm Sci, 47(8) (2008) 1086-1095.
[4] H. Cao, G. Chen, Optimization design of microchannel heat sink geometry for high power laser mirror, Applied Thermal Engineering, 30(13) (2010) 1644-1651.
[5] A.G. Fedorov, R. Viskanta, Three-dimensional conjugate heat transfer in the microchannel heat sink for electronic packaging, Int J Heat Mass Tran, 43(3) (2000) 399-415.
[6] G.E. Moore, Cramming more components onto integrated circuits, in, McGraw-Hill New York, NY, USA, 1965.
[7] S.I. Association, International technology roadmap for semiconductors (ITRS), 2003 edition, (2003).
[8] J. RATH, China's Milky Way-2 Is World's Top Supercomputer, in, data center knowledge 2013.
[9] C. Moore, Data Processing in Exascale-Class System, in: The Salishan Conference on High Speed Computing, 2011.
[10] S.G. Kandlikar, Review and Projections of Integrated Cooling Systems for Three-Dimensional Integrated Circuits, J Electron Packaging, 136(2) (2014) 024001.
[11] A. Bar-Cohen, M. Arik, M. Ohadi, Direct liquid cooling of high flux micro and nano electronic components, P Ieee, 94(8) (2006) 1549-1570.
[12] B.K. Bose, Modern power electronics and AC drives, Prentice Hall USA, 2002.
[13] Z. Xu, M. Li, F. Wang, Z. Liang, Investigation of Si IGBT operation at 200 C for traction applications, Power Electronics, IEEE Transactions on, 28(5) (2013) 2604-2615.
[14] S.G. Kandlikar, S. Colin, Y. Peles, S. Garimella, R.F. Pease, J.J. Brandner, D.B. Tuckerman, Heat Transfer in Microchannels-2012 Status and Research Needs, J Heat Trans-T Asme, 135(9) (2013).
[15] J. Kim, Spray cooling heat transfer: the state of the art, Int J Heat Fluid Fl, 28(4) (2007) 753-767.
[16] S.G. Kandlikar, A.V. Bapat, Evaluation of jet impingement, spray and microchannel chip cooling options for high heat flux removal, Heat Transfer Eng, 28(11) (2007) 911-923.
[17] A. Pavlova, M. Amitay, Electronic cooling using synthetic jet impingement, Journal of heat transfer, 128(9) (2006) 897-907.
[18] R. Chein, Y. Chen, Performances of thermoelectric cooler integrated with microchannel heat sinks, International Journal of Refrigeration, 28(6) (2005) 828-839.
[19] S.G. Kandlikar, W.J. Grande, Evaluation of single phase flow in microchannels for high heat flux chip cooling - Thermohydraulic performance enhancement and fabrication technology, Heat Transfer Eng, 25(8) (2004) 5-16.
[20] Z. Mo, J. Anderson, J. Liu, Integrating nano carbontubes with microchannel cooler, in: High Density Microsystem Design and Packaging and Component Failure Analysis, 2004. HDP'04. Proceeding of the Sixth IEEE CPMT Conference on, IEEE, 2004, pp. 373-376.

[21] S.G. Kandlikar, S. Joshi, S. Tian, Effect of surface roughness on heat transfer and fluid flow characteristics at low Reynolds numbers in small diameter tubes, Heat Transfer Eng, 24(3) (2003) 4-16.
[22] Y.-J. Lee, P.-S. Lee, S.-K. Chou, Enhanced microchannel heat sinks using oblique fins, in: ASME 2009 InterPACK Conference collocated with the ASME 2009 Summer Heat Transfer Conference and the ASME 2009 3rd International Conference on Energy Sustainability, American Society of Mechanical Engineers, 2009, pp. 253-260.
[23] Y. Sui, C.J. Teo, P.S. Lee, Y.T. Chew, C. Shu, Fluid flow and heat transfer in wavy microchannels, Int J Heat Mass Tran, 53(13-14) (2010) 2760-2772.
[24] R.C. Chu, A review of IBM sponsored research and development projects for computer cooling, P Ieee Semicond Ther, (1999) 151-165.
[25] R.C. Chu, R.E. Simons, M.J. Ellsworth, R.R. Schmidt, V. Cozzolino, Review of cooling technologies for computer products, Ieee T Device Mat Re, 4(4) (2004) 568-585.
[26] R.C. Chu, The challenges of electronic cooling: Past, current and future, J Electron Packaging, 126(4) (2004) 491-500.
[27] B. Agostini, M. Fabbri, J.E. Park, L. Wojtan, J.R. Thome, B. Michel, State of the art of high heat flux cooling technologies, Heat Transfer Eng, 28(4) (2007) 258-281.
[28] S.G. Kandlikar, History, advances, and challenges in liquid flow and flow boiling heat transfer in microchannels: A critical review, Transactions of the ASME-C-Journal of HeatTransfer, 134(3) (2012) 034001.
[29] M.G. Khan, A. Fartaj, A review on microchannel heat exchangers and potential applications, Int J Energ Res, 35(7) (2011) 553-582.
[30] Bellhous.Bj, Bellhous.Fh, C.M. Curl, Macmilla.Ti, A.J. Gunning, E.H. Spratt, Macmurra.Sb, J.M. Nelems, High-Efficiency Membrane Oxygenator and Pulsatile Pumping System, and Its Application to Animal Trials, T Am Soc Art Int Org, 19 (1973) 72-79.
[31] I.J. Sobey, Flow through Furrowed Channels .1. Calculated Flow Patterns, J Fluid Mech, 96(Jan) (1980) 1-26.
[32] I.J. Sobey, K.D. Stephanoff, B.J. Bellhouse, Flow through Furrowed Channels .2. Observed Flow Patterns, J Fluid Mech, 96(Jan) (1980) 27-32.
[33] T. Nishimura, Y. Ohori, Y. Kawamura, Flow Characteristics in a Channel with Symmetric Wavy Wall for Steady Flow, J Chem Eng Jpn, 17(5) (1984) 466-471.
[34] T. Nishimura, Y. Ohori, Y. Kajimoto, Y. Kawamura, Mass-Transfer Characteristics in a Channel with Symmetrical Wavy Wall for Steady Flow, J Chem Eng Jpn, 18(6) (1985) 550-555.
[35] T. Nishimura, S. Murakami, S. Arakawa, Y. Kawamura, Flow Observations and Mass-Transfer Characteristics in Symmetrical Wavy-Walled Channels at Moderate Reynolds-Numbers for Steady Flow, Int J Heat Mass Tran, 33(5) (1990) 835-845.
[36] S. Blancher, R. Creff, P. Le Quere, Effect of Tollmien Schlichting wave on convective heat transfer in a wavy channel. Part 1: Linear analysis, Int J Heat Fluid Fl, 19(1) (1998) 39-48.
[37] M. Greiner, P.F. Fischer, H.M. Tufo, Two-dimensional simulations of enhanced heat transfer in an intermittently grooved channel, J Heat Trans-T Asme, 124(3) (2002) 538-545.
[38] M. Greiner, P.F. Fischer, H.M. Tufo, R.A. Wirtz, Three-dimensional simulations of enhanced heat transfer in a flat passage downstream from a grooved channel, J Heat Trans-T Asme, 124(1) (2002) 169-176.
[39] M. Greiner, R.J. Faulkner, V.T. Van, H.M. Tufo, P.F. Fischer, Simulations of three-dimensional flow and augmented heat transfer in a symmetrically grooved channel, J Heat Trans-T Asme, 122(4) (2000) 653-660.

[40] R.A. Wirtz, F. Huang, M. Greiner, Correlation of fully developed heat transfer and pressure drop in a symmetrically grooved channel, J Heat Trans-T Asme, 121(1) (1999) 236-239.
[41] M. Greiner, G.J. Spencer, P.F. Fischer, Direct numerical simulation of three-dimensional flow and augmented heat transfer in a grooved channel, J Heat Trans-T Asme, 120(3) (1998) 717-723.
[42] M. Greiner, R.F. Chen, R.A. Wirtz, Enhanced Heat-Transfer Pressure-Drop Measured from a Flat Surface in a Grooved Channel, J Heat Trans-T Asme, 113(2) (1991) 498-501.
[43] P.E. Geyer, N.R. Rosaguti, D.F. Fletcher, B.S. Haynes, Laminar flow and heat transfer in periodic serpentine mini-channels, J Enhanc Heat Transf, 13(4) (2006) 309-320.
[44] N.R. Rosaguti, D.F. Fletcher, B.S. Haynes, Laminar flow and heat transfer in a periodic serpentine channel with semi-circular cross-section, Int J Heat Mass Tran, 49(17-18) (2006) 2912-2923.
[45] P.E. Geyer, D.F. Fletcher, B.S. Haynes, Laminar flow and heat transfer in a periodic trapezoidal channel with semi-circular cross-section, Int J Heat Mass Tran, 50(17) (2007) 3471-3480.
[46] N.R. Rosaguti, D.F. Fletcher, B.S. Haynes, Low-Reynolds number heat transfer enhancement in sinusoidal channels, Chem Eng Sci, 62(3) (2007) 694-702.
[47] Z. Zheng, D.F. Fletcher, B.S. Haynes, Laminar heat transfer simulations for periodic zigzag semicircular channels: Chaotic advection and geometric effects, Int J Heat Mass Tran, 62 (2013) 391-401.
[48] Z. Zheng, D.F. Fletcher, B.S. Haynes, Transient laminar heat transfer simulations in periodic zigzag channels, Int J Heat Mass Tran, 71 (2014) 758-768.
[49] H. Heidary, M. Kermani, Effect of nano-particles on forced convection in sinusoidal-wall channel, Int Commun Heat Mass, 37(10) (2010) 1520-1527.
[50] M. Ahmed, N. Shuaib, M. Yusoff, Numerical investigations on the heat transfer enhancement in a wavy channel using nanofluid, Int J Heat Mass Tran, 55(21) (2012) 5891-5898.
[51] Y. Joshi, L. Gong, K. Kota, W.Q. Tao, Parametric Numerical Study of Flow and Heat Transfer in Microchannels With Wavy Walls, J Heat Trans-T Asme, 133(5) (2011).
[52] P. Gunnasegaran, H. Mohammed, N. Shuaib, R. Saidur, The effect of geometrical parameters on heat transfer characteristics of microchannels heat sink with different shapes, Int Commun Heat Mass, 37(8) (2010) 1078-1086.
[53] H. Mohammed, P. Gunnasegaran, N. Shuaib, Influence of channel shape on the thermal and hydraulic performance of microchannel heat sink, Int Commun Heat Mass, 38(4) (2011) 474-480.
[54] H.A. Mohammed, P. Gunnasegaran, N.H. Shuaib, Numerical simulation of heat transfer enhancement in wavy microchannel heat sink, Int Commun Heat Mass, 38(1) (2011) 63-68.
[55] G. Xia, L. Chai, H. Wang, M. Zhou, Z. Cui, Optimum thermal design of microchannel heat sink with triangular reentrant cavities, Applied Thermal Engineering, 31(6) (2011) 1208-1219.
[56] G. Xia, L. Chai, M. Zhou, H. Wang, Effects of structural parameters on fluid flow and heat transfer in a microchannel with aligned fan-shaped reentrant cavities, Int J Therm Sci, 50(3) (2011) 411-419.
[57] H. Aref, Stirring by Chaotic Advection, J Fluid Mech, 143(Jun) (1984) 1-21.
[58] N.-T. Nguyen, Z. Wu, Micromixers—a review, Journal of Micromechanics and Microengineering, 15(2) (2005) R1.

[59] C.-P. Jen, C.-Y. Wu, Y.-C. Lin, C.-Y. Wu, Design and simulation of the micromixer with chaotic advection in twisted microchannels, Lab Chip, 3(2) (2003) 77-81.
[60] H. Xia, S. Wan, C. Shu, Y. Chew, Chaotic micromixers using two-layer crossing channels to exhibit fast mixing at low Reynolds numbers, Lab on a Chip, 5(7) (2005) 748-755.
[61] C.Y. Lee, C.L. Chang, Y.N. Wang, L.M. Fu, Microfluidic Mixing: A Review, International Journal of Molecular Sciences, 12(5) (2011) 3263-3287.
[62] M. Shaker, H. Ghaedamini, A.P. Sasmito, J.C. Kurnia, S.V. Jangam, A.S. Mujumdar, Numerical investigation of laminar mass transport enhancement in heterogeneous gaseous microreactors, Chem Eng Process, 54 (2012) 1-11.
[63] M.A. Stremler, F. Haselton, H. Aref, Designing for chaos: applications of chaotic advection at the microscale, Philosophical Transactions of the Royal Society of London. Series A: Mathematical, Physical and Engineering Sciences, 362(1818) (2004) 1019-1036.
[64] Y. Sui, P.S. Lee, C.J. Teo, An experimental study of flow friction and heat transfer in wavy microchannels with rectangular cross section, Int J Therm Sci, 50(12) (2011) 2473-2482.
[65] Y. Sui, C.J. Teo, P.S. Lee, Direct numerical simulation of fluid flow and heat transfer in periodic wavy channels with rectangular cross-sections, Int J Heat Mass Tran, 55(1-3) (2012) 73-88.
[66] A.M. Guzman, C.H. Amon, Transition to Chaos in Converging Diverging Channel Flows - Ruelle-Takens-Newhouse Scenario, Phys Fluids, 6(6) (1994) 1994-2002.
[67] A.M. Guzman, C.H. Amon, Dynamical flow characterization of transitional and chaotic regimes in converging-diverging channels, J Fluid Mech, 321 (1996) 25-57.
[68] C.H. Amon, A.M. Guzman, B. Morel, Lagrangian chaos, Eulerian chaos, and mixing enhancement in converging-diverging channel flows, Phys Fluids, 8(5) (1996) 1192-1206.
[69] A.M. Guzman, R.A. Hormazabal, T.A. Aracena, Heat Transfer Enhancement Due to Frequency Doubling and Ruelle-Takens-Newhouse Transition Scenarios in Symmetric Wavy Channels, J Heat Trans-T Asme, 131(9) (2009).
[70] A.M. Guzmán, M.J. Cárdenas, F.A. Urzúa, P.E. Araya, Heat transfer enhancement by flow bifurcations in asymmetric wavy wall channels, Int J Heat Mass Tran, 52(15) (2009) 3778-3789.
[71] G. Wang, S.P. Vanka, Convective Heat-Transfer in Periodic Wavy Passages, Int J Heat Mass Tran, 38(17) (1995) 3219-3230.
[72] E. Stalio, M. Piller, Direct numerical simulation of heat transfer in converging-diverging wavy channels, J Heat Trans-T Asme, 129(7) (2007) 769-777.
[73] M. Faghri, K. Javdani, A. Faghri, Heat-Transfer with Laminar Pulsating Flow in a Pipe, Lett Heat Mass Trans, 6(4) (1979) 259-270.
[74] A. Yakhot, M. Arad, G. Ben-Dor, Numerical investigation of a laminar pulsating flow in a rectangular duct, Int J Numer Meth Fl, 29(8) (1999) 935-950.
[75] M.A. Habib, A.M. Attya, A.I. Eid, A.Z. Aly, Convective heat transfer characteristics of laminar pulsating pipe air flow, Heat Mass Transfer, 38(3) (2002) 221-232.
[76] H.N. Hemida, M.N. Sabry, A. Abdel-Rahim, H. Mansour, Theoretical analysis of heat transfer in laminar pulsating flow, Int J Heat Mass Tran, 45(8) (2002) 1767-1780.
[77] D.L. Zeng, H. Gao, X.C. Zeng, C. Liu, J. Zheng, Heat transfer enhancement by using self-oscillation, Proceedings of the 3rd International Symposium on Heat Transfer Enhancement and Energy Conservation, Vols 1 and 2, (2004) 677-681.
[78] J.W. Moon, S.Y. Kim, H.H. Cho, Frequency-dependent heat transfer enhancement from rectangular heated block array in a pulsating channel flow, Int J Heat Mass Tran, 48(23-24) (2005) 4904-4913.

[79] H. Chattopadhyay, F. Durst, S. Ray, Analysis of heat transfer in simultaneously developing pulsating laminar flow in a pipe with constant wall temperature, Int Commun Heat Mass, 33(4) (2006) 475-481.
[80] M. Sumida, Pulsatile entrance flow in curved pipes: effect of various parameters, Exp Fluids, 43(6) (2007) 949-958.
[81] B. Olayiwola, P. Walzel, Cross-flow transport and heat transfer enhancement in laminar pulsed flow, Chem Eng Process, 47(5) (2008) 929-937.
[82] T. Persoons, T. Saenen, T. Van Oevelen, T. Baelmans, Effect of flow pulsation on the heat transfer performance of a microchannel heat sink, Journal of Heat Transfer, (2012).
[83] I.J. Sobey, The Occurrence of Separation in Oscillatory Flow, J Fluid Mech, 134(Sep) (1983) 247-257.
[84] I.J. Sobey, Oscillatory Flows at Intermediate Strouhal Number in Asymmetric Channels, J Fluid Mech, 125(Dec) (1982) 359-373.
[85] T. Nishimura, N. Oka, Y. Yoshinaka, K. Kunitsugu, Influence of imposed oscillatory frequency on mass transfer enhancement of grooved channels for pulsatile flow, Int J Heat Mass Tran, 43(13) (2000) 2365-2374.
[86] T. Nishimura, K. Kunitsugu, Self-sustained oscillatory flow and fluid mixing in grooved channels, Kagaku Kogaku Ronbun, 23(6) (1997) 764-771.
[87] T. Nishimura, Y. Kawamura, Transition of Oscillatory Flow in a Symmetric Sinusoidal Wavy-Walled Channel, Els Ser Therm Fluid, (1993) 928-935.
[88] T. Nishimura, H. Miyashita, S. Murakami, Y. Kawamura, Oscillatory Flow in a Symmetrical Sinusoidal Wavy-Walled Channel at Intermediate Strouhal Numbers, Chem Eng Sci, 46(3) (1991) 757-771.
[89] T. Nishimura, H. Miyashita, S. Murakami, Y. Kawamura, Effect of Strouhal Number on Flow Characteristics in a Symmetric Sinusoidal Wavy-Walled Channel for Oscillatory Flow, J Chem Eng Jpn, 22(5) (1989) 505-511.
[90] T. Nishimura, S. Arakawa, S. Murakami, Y. Kawamura, Oscillatory Viscous-Flow in Symmetric Wavy-Walled Channels, Chem Eng Sci, 44(10) (1989) 2137-2148.
[91] T. Nishimura, A. Tarumoto, Y. Kawamura, Flow and Mass-Transfer Characteristics in Wavy Channels for Oscillatory Flow, Int J Heat Mass Tran, 30(5) (1987) 1007-1015.
[92] T. Nishimura, S. Matsune, Mass transfer enhancement in a sinusoidal wavy channel for pulsatile flow, Heat Mass Transfer, 32(1-2) (1996) 65-72.
[93] T. Nishimura, N. Kojima, Mass-Transfer Enhancement in a Symmetrical Sinusoidal Wavy-Walled Channel for Pulsatile Flow, Int J Heat Mass Tran, 38(9) (1995) 1719-1731.
[94] G. Haller, Chaos near resonance, Springer Verlag, 1999.
[95] B.D. Iverson, S.V. Garimella, Recent advances in microscale pumping technologies: a review and evaluation, Microfluidics and Nanofluidics, 5(2) (2008) 145-174.
[96] N.T. Obot, Toward a better understanding of friction and heat/mass transfer in microchannels - A literature review, Microscale Therm Eng, 6(3) (2002) 155-173.
[97] E. Ott, Chaos in dynamical systems, Cambridge university press, 2002.
[98] M.W. Hirsch, S. Smale, R.L. Devaney, Differential equations, dynamical systems, and an introduction to chaos, Academic press, 2004.
[99] E.N. Lorenz, Deterministic Nonperiodic Flow, Journal of the Atmospheric Sciences, 20(2) (1963) 130-141.
[100] J. Ottino, Mixing, chaotic advection, and turbulence, Annual Review of Fluid Mechanics, 22(1) (1990) 207-254.
[101] G. Fountain, D. Khakhar, I. Mezic, J. Ottino, Chaotic mixing in a bounded three-dimensional flow, J Fluid Mech, 417 (2000) 265-301.
[102] H. Ghaedamini, P. Lee, C. Teo, Developing forced convection in converging–diverging microchannels, Int J Heat Mass Tran, 65 (2013) 491-499.

[103] D. Khakhar, J. Franjione, J. Ottino, A case study of chaotic mixing in deterministic flows: the partitioned-pipe mixer, Chem Eng Sci, 42(12) (1987) 2909-2926.
[104] G. Alfonsi, Coherent structures of turbulence: Methods of education and results, Appl Mech Rev, 59(1-6) (2006) 307-323.
[105] R.M. Manglik, J. Zhang, A. Muley, Low Reynolds number forced convection in three-dimensional wavy-plate-fin compact channels: fin density effects, Int J Heat Mass Tran, 48(8) (2005) 1439-1449.
[106] R. Shah, A. London, Laminar flow forced convection in ducts: a source book for compact heat exchanger analytical data, Supl. 1, in, Academic Press, New York, 1978.
[107] J.M. Ottino, The kinematics of mixing: stretching, chaos, and transport, Cambridge University Press, 1989.
[108] J. Jeong, F. Hussain, On the Identification of a Vortex, J Fluid Mech, 285 (1995) 69-94.
[109] K. Balasubramanian, P. Lee, C. Teo, S. Chou, Flow boiling heat transfer and pressure drop in stepped fin microchannels, Int J Heat Mass Tran, 67 (2013) 234-252.
[110] P.-S. Lee, S.V. Garimella, D. Liu, Investigation of heat transfer in rectangular microchannels, Int J Heat Mass Tran, 48(9) (2005) 1688-1704.
[111] T. Burghelea, E. Segre, I. Bar-Joseph, A. Groisman, V. Steinberg, Chaotic flow and efficient mixing in a microchannel with a polymer solution, Phys Rev E, 69(6) (2004).
[112] F.P. Incropera, D.P. De Witt, Fundamentals of heat and mass transfer, (1985).
[113] V. Zimparov, Energy conservation through heat transfer enhancement techniques, Int J Energ Res, 26(7) (2002) 675-696.
[114] J. Taylor, Introduction to error analysis, the study of uncertainties in physical measurements, 1997.

Appendix A: Uncertainty Analysis for Experimental Data

In order to calculate the uncertainty of the experimental data, the principles proposed by J.R. Taylor [114] are used in this thesis. Table A1 below has summarized the standard error analysis for different functions:

Table A 1. Standard error analysis

Function	Standard error
$f = x + ... + z - (u + ... + w)$	$\delta f = (\delta x^2 + ... + \delta z^2 + \delta u^2 + ... + \delta w^2)^{0.5}$ $\delta f \le \delta x + ... + \delta z + \delta u + ... + \delta w$
$f = \frac{x \times ... \times z}{u \times ... \times w}$	$\frac{\delta f}{\lvert f \rvert} = \left(\left(\frac{\delta x}{\lvert x \rvert} \right)^2 + ... + \left(\frac{\delta z}{\lvert z \rvert} \right)^2 + \left(\frac{\delta u}{\lvert u \rvert} \right)^2 + ... + \left(\frac{\delta w}{\lvert w \rvert} \right)^2 \right)^{0.5}$ $\frac{\delta f}{\lvert f \rvert} \le \left(\frac{\delta x}{\lvert x \rvert} \right) + ... + \left(\frac{\delta z}{\lvert z \rvert} \right) + \left(\frac{\delta u}{\lvert u \rvert} \right) + ... + \left(\frac{\delta w}{\lvert w \rvert} \right)$
$f = x^n$	$\frac{\delta f}{\lvert f \rvert} = \lvert n \rvert \frac{\delta x}{\lvert x \rvert}$
$f = f(x)$	$\delta f = \left\lvert \frac{df}{dx} \right\rvert \delta x$
$f = f(x, y, .., z)$	$\delta f = \left(\left(\frac{\partial f}{\partial x} \delta x \right)^2 + ... + \left(\frac{\partial f}{\partial z} \delta z \right)^2 \right)^{0.5}$ $\delta f \le \left(\frac{\partial f}{\partial x} \delta x \right) + ... + \left(\frac{\partial f}{\partial z} \delta z \right)$

Table A2 shows the accuracies and the range for experimental uncertainties associated with the measurements. It should be noted that the greatest uncertainty for heat transfer

coefficient measurement was related to the inlet to outlet fluid temperature difference measurements.

Table A 2. The measurement accuracies and the range of experimental uncertainties associated with sensors and parameters.

Sensor/Parameter	Accuracy/uncertainty
T-type thermocouples	$\pm 0.5°C$
Flow meter	$\pm 10 ml/min$
Differential pressure transducer	$\pm 0.165 mbar$
Dimension measurement	$\pm 10 \mu m$
Heat flux	6%-14%
Pressure drop	0.7%-16%
Heat transfer coefficient	7%-16%
Friction factor coefficient	3%-21%

Table A3 summarizes the main equation being used for data reduction. It should be noted that for calculating the error related to heat transfer coefficient h, since η is a function of h, $\delta\eta$ would also be a function of δh. Hence, an iterative method is needed to calculate the accuracy of h. At the same time, a conservative approach can be taken which considers $\eta = 1$ and assumes simpler functions to calculate the error related to measuring the side area A_{cs} and bottom area A_{cb} of the microchannel. The error calculated in this way is larger than the actual error but is less tedious than an iterative method.

Table A 3. The main functions and the related formula used for uncertainty analysis.

Function	Standard error
$Re = \frac{\rho U D}{\mu}$	$\frac{\delta Re}{Re} = \left(\left(\frac{\delta U}{U} \right)^2 + \left(\frac{\delta D}{D} \right)^2 \right)^{0.5}$
$D = \frac{4 \times ab}{2(a+b)}$	$\frac{\delta D}{D} = \left(\left(\frac{\partial D}{\partial a} \delta a \right)^2 + \left(\frac{\partial D}{\partial b} \delta b \right)^2 \right)^{0.5} \approx 0.016$ $\frac{\partial D}{\partial a} = \frac{4b^2}{(a+b)^2}$ $\frac{\partial D}{\partial b} = \frac{4a^2}{(a+b)^2}$
$U = \frac{\dot{V}}{ab}$	$\frac{\delta U}{U} = \left(\left(\frac{\delta \dot{V}}{\dot{V}} \right)^2 + \left(\frac{\delta a}{a} \right)^2 + \left(\frac{\delta b}{b} \right)^2 \right)^{0.5}$
$q = \rho c_p \dot{V} (T_{m,out} - T_{m,in})$	$\frac{\delta q}{q} = \left(\left(\frac{\delta \dot{V}}{\dot{V}} \right)^2 + \left(\frac{\delta (T_{m,out} - T_{m,in})}{\lvert T_{m,out} - T_{m,in} \rvert} \right)^2 \right)^{0.5}$ $\delta (T_{m,out} - T_{m,in}) = \sqrt{2} \delta T \approx \pm 0.7°\text{C}$
$T_w = (0.25T_1 + 0.5T_2 + 0.25T_3) - \frac{Sq''}{k_{Cu}}$	$\delta T_w = \left(\left(\delta (0.25T_1 + 0.5T_2 + 0.25T_3) \right)^2 + \left(\delta \left(\frac{Sq''}{k_{Cu}} \right) \right)^2 \right)^{0.5}$ $\delta (0.25T_1 + 0.5T_2 + 0.25T_3) = \pm 0.3°\text{C}$ $\delta \left(\frac{Sq''}{k_{Cu}} \right) = \frac{Sq''}{k_{Cu}} \left(\left(\frac{\delta S}{S} \right)^2 + \left(\frac{\delta q''}{q''} \right)^2 \right)^{0.5}$ $\frac{\delta S}{S} \approx 1e-3$

$$q'' = \frac{q}{A_{FP}} \qquad \frac{\delta q''}{q''} = \left(\left(\frac{\delta q}{q} \right)^2 + \left(\frac{\delta A_{FP}}{A_{FP}} \right)^2 \right)^{0.5}$$

$$\frac{\delta A_{FP}}{A_{FP}} \approx 5.66e-4$$

$$h = \frac{q}{M(A_{cb} + 2A_{cs}\eta)(T_w - T_m)} \qquad \frac{\delta h}{h} = \left(\left(\frac{\delta q}{q} \right)^2 + \left(\frac{\delta (A_{cb} + 2A_{cs}\eta)}{|A_{cb} + 2A_{cs}\eta|} \right)^2 + \left(\frac{\delta (T_w - T_m)}{|T_w - T_m|} \right)^2 \right)^{0.5}$$

$$assuming \eta = 1 \Rightarrow$$

$$\eta = \frac{\tanh(mb)}{mb} \qquad \frac{\delta (A_{cb} + 2A_{cs}\eta)}{|A_{cb} + 2A_{cs}\eta|} = \left(\left(\frac{\delta A_{cb}}{A_{cb}} \right)^2 + 2\eta \left(\frac{\delta A_{cs}}{A_{cs}} \right)^2 \right)^{0.5}$$

$$m = \frac{2h}{k_f S_w}$$

$$\frac{\delta A_{cb}}{A_{cb}} \approx \left(\left(\frac{\delta l}{l} \right)^2 + \left(\frac{\delta a}{a} \right)^2 \right)^{0.5}$$

$$\frac{\delta A_{cs}}{A_{cs}} \approx \left(\left(\frac{\delta l}{l} \right)^2 + \left(\frac{\delta b}{b} \right)^2 \right)^{0.5}$$

$$Nu = \frac{hD}{k_f} \qquad \frac{\delta Nu}{Nu} = \left(\left(\frac{\delta h}{h} \right)^2 + \left(\frac{\delta D}{D} \right)^2 \right)^{0.5}$$

$$f = \frac{(dp/dx)D}{0.5\rho U^2} \qquad \frac{\delta f}{f} = \left(\left(\frac{\delta p}{p} \right)^2 + \left(\frac{\delta l}{l} \right)^2 + \left(\frac{\delta D}{D} \right)^2 + 2\left(\frac{\delta U}{U} \right)^2 \right)^{0.5}$$